# The mechanical properties of Y-Ba-Cu-O and Gd-Ba-Cu-O/Ag bulk superconductor magnets

Kai Yuan Huang

Department of Engineering

University of Cambridge

This dissertation is submitted for the degree of

Doctor of Philosophy

Churchill College   March 2021

Declaration

This thesis is the result of my own work and includes nothing which is the outcome of work done in collaboration except as declared in the Preface and specified in the text. I further state that no substantial part of my thesis has already been submitted, or, is being concurrently submitted for any such degree, diploma or other qualification at the University of Cambridge or any other University or similar institution except as declared in the Preface and specified in the text.

This dissertation is within the word limit of 65,000 words, including appendices, bibliography, footnotes, tables and equations, and has fewer than 150 figures.

<div style="text-align: right">

Kai Yuan Huang

March 2021

</div>

The mechanical properties of Y-Ba-Cu-O and Gd-Ba-Cu-O/Ag bulk superconductor magnets

Kai Yuan Huang

Single-grain RE-Ba-Cu-O bulk high temperature superconductors [or (RE)BCO, where RE = rare earth element or yttrium] have demonstrated significant potential for practical applications due to their ability to trap magnetic fields in excess of 17 T, which is an order of magnitude greater than what can be achieved with conventional iron-based permanent magnets. One of the major obstacles to the use of (RE)BCO trapped field magnets is their poor mechanical properties, as bulk samples typically contain a large number of defects, such as pores and micro-cracks. Furthermore, significant electromagnetic stresses develop in bulk superconductors during magnetisation as a result of the Lorentz force, leading frequently to sample failure above around 10 T. Therefore, it is clear that the mechanical properties of bulk (RE)BCO need to be studied comprehensively and improved upon to realise the full potential of this technologically important material.

This study first investigated the mechanical strength of YBCO single grains at room temperature by utilising three-point bend and Brazilian tests. This was followed by measurement of the mechanical deformation of GdBCO/Ag single grains in situ, i.e. during high-field magnetisation, to determine the strains and stresses experienced by the samples as a trapped field was established inside them at 64 K.

Two techniques for improving the mechanical reliability of (RE)BCO bulk superconductors were subsequently developed. Firstly, samples of YBCO were melt-processed with artificial holes to reduce the defect population and to improve the intrinsic strength of the resultant single grains. As a result, the YBCO sample with artificial holes was able to survive significantly higher magnetisation fields and achieved a surface trapped field of 8.8 T at 30 K without any external reinforcement, which was not possible with the standard YBCO sample. Secondly, a composite structure was proposed, which involved reinforcing GdBCO/Ag single grains with stainless-steel sheets and shrink-fit stainless-steel rings. This preparation technique is also expected to improve the thermal stability of the overall structure. The first composite stack achieved 16.8 T and 17.6 T at 26 K and 22.5 K, respectively, in sequential magnetisation cycles, demonstrating the effectiveness of this reinforcement approach.

Acknowledgements

My utmost gratitude goes first and foremost to my supervisor, Prof. David Cardwell, who has been a great mentor and guided me patiently over the past four plus years. He has been nothing but incredibly supportive throughout my growth as a researcher.

I am also extremely grateful to my advisor, Dr John Durrell, for his continued assistance and guidance throughout the PhD.

Words cannot express my gratitude to Dr Yunhua Shi, Dr Devendra Namburi, Dr Difan Zhou, Dr Mark Ainslie and Dr Martin Boll, who have offered invaluable help with the experimental and computational work I carried out. I have learnt so much from them.

I would also like to thank Mr Anthony Dennis and Mr Harry Druiff for providing assistance with the practical aspects of the PhD and for always motivating me whenever I was in the lab.

Additionally, this PhD would not have been enjoyable without all the amazing friends and colleagues I met whilst in the Bulk Superconductivity Group. Working in a research lab would have been tough without the friendly banter and I am truly appreciative to have been a part of such a friendly, supportive and collaborative team.

I would like to acknowledge financial support from the Engineering and Physical Sciences Research Council (EPSRC). In addition, I would like to thank Churchill College and the Engineering Department for providing financial assistance that made it possible for me to attend and present at various conferences throughout the years.

I would also like to thank Dr Christy Hung, who stuck by my side through all of the ups and downs of the PhD and always provided encouraging words.

Most importantly, I would like to thank my parents, who have supported me unconditionally every step of the way. I am truly thankful for their support.

List of publications

K. Y. Huang, T. Hlásek, D. K. Namburi, A. R. Dennis, Y. Shi, M. D. Ainslie, J. V. J. Congreve, V. Plecháček, J. Plecháček, D. A. Cardwell, and J. H. Durrell. "Improved trapped field performance of single grain Y-Ba-Cu-O bulk superconductors containing artificial holes." *Journal of the American Ceramic Society* 104, no. 12 (2021): 6309-6318.

K. Y. Huang, Y. Shi, J. Srpčič, M. D. Ainslie, D. K. Namburi, A. R. Dennis, D. Zhou, M. Boll, M. Filipenko, J. Jaroszynski, E. E. Hellstrom, D. A. Cardwell, and J. H. Durrell. "Composite stacks for reliable> 17 T trapped fields in bulk superconductor magnets." *Superconductor Science and Technology* 33, no. 2 (2019): 02LT01.

K. Y. Huang, D. Zhou, J. Srpčič, Y. Shi, D. K. Namburi, A. Dennis, M. D. Ainslie, M. Boll, R. Bause, M. Filipenko, J. H. Durrell, and D. A. Cardwell. "Spatial distribution of flexural strength in Y–Ba–Cu–O bulk superconductors." *IEEE Transactions on Applied Superconductivity* 28, no. 4 (2018): 1-5.

D. K. Namburi, **K. Huang**, W. Lau, Y. Shi, K. G. Palmer, A. R. Dennis, D. A. Cardwell, and J. H. Durrell. "A simple, reliable and robust reinforcement method for the fabrication of (RE)–Ba–Cu–O bulk superconductors." *Superconductor Science and Technology* 33, no. 5 (2020): 054005.

D. Barthlott, **K. Y. Huang**, J. H. Durrell, D. A. Cardwell, B. Holzapfel, and M. D. Ainslie. "Numerical optimisation of mechanical ring reinforcement for bulk high-temperature superconductors." *Journal of Physics: Conference Series*, vol. 1559, no. 1 (2020), p. 012031. IOP Publishing.

M. D. Ainslie, **K. Y. Huang**, H. Fujishiro, J. Chaddock, K. Takahashi, S. Namba, D. A. Cardwell, and J. H. Durrell. "Numerical modelling of mechanical stresses in bulk superconductor magnets with and without mechanical reinforcement." *Superconductor Science and Technology* 32, no. 3 (2019): 034002.

T. Hlásek, **K. Y. Huang**, J. Esnoz-Larraya, V. Plecháček, J. H. Durrell, I. Valiente-Blanco, and D. A. Cardwell. "Enhanced mechanical properties of single-domain YBCO bulk superconductors processed with artificial holes." *IEEE Transactions on Applied Superconductivity* 29, no. 5 (2019): 1-4.

D. Zhou, J. Srpcic, **K. Huang**, M. Ainslie, Y. Shi, A. Dennis, M. Boll, M. Filipenko, D. Cardwell, and J. Durrell. "Reliable 4.8 T trapped magnetic fields in Gd–Ba–Cu–O bulk superconductors using pulsed field magnetization." *Superconductor Science and Technology* 34, no. 3 (2021): 034002.

J. V. J. Congreve, Y. Shi, **K. Y. Huang**, A. R. Dennis, J. H. Durrell, and D. A. Cardwell. "Improving mechanical strength of YBCO bulk superconductors by addition of Ag." *IEEE Transactions on Applied Superconductivity* 29, no. 5 (2019): 1-5.

J. Srpčič, F. Perez, **K. Y. Huang**, Y. Shi, M. D. Ainslie, A. R. Dennis, M. Filipenko, M. Boll, D. A. Cardwell, and J. H. Durrell. "Penetration depth of shielding currents due to crossed magnetic fields in bulk (RE)-Ba-Cu-O superconductors." *Superconductor Science and Technology* 32, no. 3 (2019): 035010.

J. V. J. Congreve, Y. Shi, **K. Y. Huang**, A. R. Dennis, J. H. Durrell, and D. A. Cardwell. "Characterisation of the mechanical failure and fracture mechanisms of single grain Y–Ba–Cu–O bulk superconductors." *Superconductor Science and Technology* 33, no. 1 (2019): 015003.

Contents

List of figures

List of tables

List of abbreviations and symbols

AC	Alternating current
Ag	Silver
Ba	Barium
Ce	Cerium
Cu	Copper
DC	Direct current
DIC	Digital image correlation
Eu	Europium
FBG	Fibre Bragg grating
FC	Field-cooling
FCM	Field cooled magnetisation
Fe	Iron
FEM	Finite element method
Gd	Gadolinium
GdBCO	Gd-Ba-Cu-O gadolinium barium copper oxide Usually referring to the Gd-123/Gd-211 composite
GdBCO/Ag	Silver-containing gadolinium barium copper oxide
GPa	Gigapascal
GS	Growth sector
GSB	Growth sector boundary

h	Hour
HTS	High-temperature superconductor
La	Lanthanum
LHe	Liquid helium
LN_2	Liquid nitrogen
LTS	Low-temperature superconductor
Maglev	Magnetic levitation
Mg	Magnesium
MgB_2	Magnesium diboride
MPa	Megapascal
MRI	Magnetic resonance imaging
Nd	Neodymium
NMR	Nuclear magnetic resonance
O	Oxygen
PFM	Pulsed field magnetisation
Pt	Platinum
RE	Rare earth element or yttrium
(RE)BCO	RE-Ba-Cu-O rare earth barium copper oxide
	Usually referring to the RE-123/RE-211 composite
RE-123	$REBa_2Cu_3O_{7-\delta}$ superconducting phase
RE-211	RE_2BaCuO_5 non-superconducting phase

SEM	Scanning electron microscope
Sm	Samarium
SQUID	Superconducting quantum interference device
STM	Scanning tunnelling microscope
T	Tesla
TSIG	Top seeded infiltration and growth
TSMG	Top seeded melt growth
wt %	Percentage by weight
Y	Yttrium
Yb	Ytterbium
YBCO	Y-Ba-Cu-O yttrium barium copper oxide
	Usually referring to the Y-123/Y-211 composite
ZFC	Zero-field-cooling
2D	Two-dimensional
3D	Three-dimensional

a	Crystallographic a-direction
b	Crystallographic b-direction
B	Magnetic flux density
$B_{applied}$	Applied field
$B_{trapped}$	Trapped field
	Usually referring to field trapped at the centre of a superconductor
c	Crystallographic c-direction
D	Diameter of a cylindrical sample
e	Electron charge
E	Electric field (in the context of electromagnetism)
	Young's modulus (in the context of mechanical properties)
F_L	Lorentz force
F_p	Pinning force
(g)	Gaseous state
h	Planck's constant
H	Magnetic field strength
H_c	Critical field
H_{c1}	Lower critical field
H_{c2}	Upper critical field
H_{irr}	Irreversibility field
H_p	Penetration field

J	Current density
J_c	Critical current density
J_e	Engineering current density
K_{IC}	Fracture toughness
(l)	Liquid state
m	Magnetic moment
	Weibull coefficient (in the context of mechanical properties)
M	Magnetisation
n	n-value of a superconductor
n_s	Number density of superconducting electrons
p	Porosity
r	Radial coordinate or distance
r^*	Critical entrapment size
R	Radius of a cylindrical sample
	Growth rate (in the context of crystal growth)
(s)	Solid state
t	Time
T	Temperature
T_c	Critical temperature
T_p	Peritectic temperature
ΔT	Undercooling

z	Axial coordinate
α	Coefficient of thermal expansion
ε	Mechanical strain
ε_θ	Hoop strain
ε_r	Radial strain
η	Melt viscosity
κ	Thermal conductivity
	Ginzburg-Landau parameter (in the context of superconductivity)
λ	Penetration depth
μ_0	Permeability of free space
ρ	Density
σ	Mechanical stress or strength
σ_θ	Hoop stress
σ_r	Radial stress
σ^{COOL}	Thermal stress
σ^{FCM}	Electromagnetic stress
ν	Poisson's ratio
ξ	Coherence length
Φ_0	Magnetic flux quantum

Chapter 1

Introduction

1.1.   High temperature superconductors in single grain form

Superconductors are materials that exhibit zero resistance to electrical current when cooled below a particular cryogenic temperature. As a result, superconductors can sustain considerably higher current densities than conventional conductors, such as copper, enabling the transport of large currents with minimal power dissipation and the generation of extremely high magnetic fields. Consequently, the use of superconductors can improve significantly the performance and efficiency of many existing, predominantly sustainable, technologies.

Superconductivity was discovered in the cuprates in 1986, 75 years after the discovery of superconductivity by Kamerlingh-Onnes, when Bednorz and Müller observed superconductivity in the La-Ba-Cu-O system with an onset temperature above 30 K [1]. This exceeded the highest critical temperature achieved at the time, which was 23 K in Nb-Ge films [2], but more importantly, this was the first perovskite-structure cuprate superconductor (layered material consisting of superconducting copper oxide planes and chains) to be discovered, whereas most of the previously identified superconductors had been elements or metal alloys. This discovery provided opportunities for fine-tuning the chemical composition of this compound and ultimately ignited a quest for even higher critical temperature T_c amongst these materials. Superconductivity was subsequently observed in the Y-Ba-Cu-O system, which exhibited a significantly higher T_c of 93 K [3], by Wu and Chu in 1987. Since then, several cuprate superconductors have been fabricated with T_c well above 77 K, the boiling point of liquid nitrogen (LN$_2$). This includes the RE-Ba-Cu-O family [or (RE)BCO, where RE = rare earth element or yttrium] which demonstrate a T_c above 90 K [3], Bi-Sr-Ca-Cu-O with a T_c of 105 K [4], Tl-Ba-Ca-Cu-O with a T_c of 125 K [5] and Hg-Ba-Ca-Cu-O with a T_c of 164 K at a pressure of 30 GPa [6]. These signified major breakthroughs as the elevated temperature around and above 77 K could be reached readily in a cost-effective manner either

with LN_2 or commercial off-the-shelf cryocoolers, making them far more attractive to engineering applications than the superconductors that were discovered earlier.

Despite not completely understanding the nature of the electron pairing interaction in these so-called high temperature superconductors (HTS), scientists and engineers have continued to make steady progress in the materials science of these unique materials and have explored their potential for technical applications. For applications, superconductors are manufactured in one of three broad material forms: wires/tapes, thin films and bulks. Wires/tapes are used mostly to transport large electrical currents over long distances with minimal energy loss and can also be wound into solenoids to generate high magnetic fields within their bore. Thin films are explored primarily in the area of superconducting devices and electronics, such as superconducting transistors for ultrafast computing, due to a wide range of desirable properties. This dissertation will focus on the bulk category, in particular RE-Ba-Cu-O bulk superconductors, where samples are normally manufactured in the form of large cast and sintered products or crystallised single domains up to several centimetres in diameter for flux-trapping, levitation and shielding purposes.

RE-Ba-Cu-O bulk superconductors are usually fabricated in the form of large, single grains, i.e. the crystal lattice is predominantly continuous and unbroken across the entire bulk sample, to eliminate grain boundary weak links that severely limit the ability of the material to transport supercurrents on a macroscopic scale. Large, single-grain RE-Ba-Cu-O of several centimetres in diameter and thickness have shown great potential for practical applications due to their ability to trap magnetic fields in excess of 17 T [7], [8], which is an order of magnitude higher than the maximum field attainable by conventional permanent magnets (permanent magnets are limited fundamentally to around 2 T due to the number of Bohr magnetons per atomic site, and thus the magnetic moment achievable per atom). Furthermore, bulk superconductors also benefit from not requiring direct connection to a power supply, unlike electromagnets, and can be switched off safely by simply being warmed up.

The high magnetic field achievable with a small volume of material makes bulk superconductors attractive for a host of engineering applications [9], including electric motors/generators with unprecedented power densities, portable desktop magnetic resonance imaging/nuclear magnetic resonance (MRI/NMR) machines for imaging small specimens, magnetic separation, magnetic drug delivery and magnetically levitated transport, many of which have been or are now being studied in demonstration projects.

1.2.   Subject and aims of this thesis

Despite their tremendous potential, a number of issues still need to be addressed before RE-Ba-Cu-O bulk superconductors can be used reliably in various applications, one of which is the poor mechanical properties of these brittle, ceramic-like materials. It is widely acknowledged that RE-Ba-Cu-O bulk materials exhibit poor mechanical strength in comparison to conventional ceramics due to the relatively large number of defects, such as pores, inclusions and micro-cracks, that form during melt-processing [10]–[13], which is a necessary fabrication procedure to generate large single grains. The poor mechanical strength, in fact, limits the maximum field a typical unreinforced sample can effectively trap to around 8 T [14], since the sample is subject to a radially outward Lorentz force that scales quadratically with the trapped field as a result of the current–field interaction. Consequently, a high trapped field inadvertently drives the sample closer to mechanical failure. Furthermore, thermal stresses can develop within the bulk samples during thermal cycling, and, in certain applications, the samples may also be required to withstand additional mechanical loads, such as the centrifugal force associated with high-speed rotation in rotating machines. Therefore, a clear understanding of the mechanical behaviour of these materials and the practicable methods of preventing mechanical failure during their operation is vital to their successful technological development. A road-mapping workshop in 2016 involving 16 leading experts in the field of bulk superconductivity also highlighted better mechanical properties as one of the most pressing industrial needs [9].

This dissertation aims to address the challenges associated with characterising the mechanical properties of RE-Ba-Cu-O bulk superconductors (Chapters 3 and 4) and demonstrates means of improving the mechanical reliability of these trapped field magnets (Chapters 5 and 6).

1.3.   Thesis outline

Chapter 2 presents an overview of the fundamental principles of superconductivity relating to the work carried out during this study, including type I and type II superconductors, magnetisation curves and flux pinning. This is followed by an introduction to the different families of bulk high temperature superconductors and the reasoning behind the choice of single-grain RE-Ba-Cu-O in practical applications. The magnetisation techniques available and the potential applications of these materials, including past demonstration projects, are also

discussed. Finally, the importance of understanding and improving the mechanical properties of RE-Ba-Cu-O bulk superconductors is highlighted.

Chapters 3 to 6 cover the key experimental and numerical modelling work conducted for this dissertation, describing in detail the preparation of samples, the set-up of measurement instruments and the methods implemented. More importantly, the results of these studies and their implications are discussed.

In Chapter 3, small-scale mechanical tests performed on Y-Ba-Cu-O single grains at room temperature are presented following a literature review of studies that have measured the mechanical properties of these materials. The spatial distribution of flexural strength within 25 mm diameter Y-Ba-Cu-O bulk discs was determined using the three-point bend test and understood in terms of the spatially varying microstructure. Subsequently, the bulk-to-bulk variation in tensile strength, which was deemed highly relevant to applications, was quantified using the so-called Brazilian test, which is a technique commonly used on rock, concrete and ceramic specimens. The Brazilian test allows for the indirect determination of the tensile strength of brittle materials in cylindrical geometry, which fits well with the natural geometry of bulk RE-Ba-Cu-O samples.

In Chapter 4, measurement of the mechanical deformation of a stack of two 40 mm Ag-containing Gd-Ba-Cu-O single grains during operation as trapped field magnets below 100 K and in magnetising fields of up to 9.6 T is described. The hoop and radial strains at various points on one of the superconductor discs were measured using cryogenic strain gauges and acquired using a program written in LabVIEW. The experimentally obtained trapped fields and strains were then compared to predictions from three-dimensional numerical models implemented in COMSOL Multiphysics, where a homogeneous and an inhomogeneous case were considered. The inhomogeneous model included the spatial distribution of the critical current density and Young's modulus, both of which were determined empirically from representative samples.

In Chapter 5, the Brazilian test was used to confirm a significant enhancement in the tensile strength of the so-called thin-wall bulk superconductors, where the Y-Ba-Cu-O discs were melt-processed with a network of artificial columnar holes to decrease the effective wall thickness, sample porosity and increase the intrinsic mechanical strength of the remaining superconducting material. The improvement in strength was then confirmed directly by

comparing the magnetic fields up to which the thin-wall and standard samples could survive before failing due to the electromagnetic stresses or thermal instabilities.

In Chapter 6, post-melt-processing treatments on as-grown single grains involving stainless steel lamination and shrink-fit stainless-steel rings are proposed and assessed using COMSOL Multiphysics. The resultant composite structures, which were manufactured from 24 mm diameter Gd-Ba-Cu-O/Ag bulk superconductors, were measured in the 18 T SCM2 system at the National High Magnetic Field Laboratory (NHMFL), Florida State University. The results demonstrated the effectiveness of this inexpensive and straight-forward reinforcement approach, as the first composite stack achieved trapped fields ≥ 16.8 T in its first two runs without failing. Two subsequent composite stacks also successfully survived their initial runs and trapped fields of around 16 T.

Finally, Chapter 7 summarises the major contributions of this dissertation to the field and their potential implications. Possible future research directions, which build on the methods and results presented in this dissertation, are proposed.

Chapter 2

Theoretical overview

This chapter introduces the fundamental phenomenological theories relating to superconductivity and the candidate materials for high-field applications. The factors that make RE-Ba-Cu-O bulk superconductors one of the most promising candidates are subsequently presented, followed by a brief overview of the processing, characterisation and magnetisation of these technologically important materials. The significance of the mechanical properties of RE-Ba-Cu-O single grains pertaining to practical applications is then discussed.

2.1.   Fundamentals of superconductivity

2.1.1.   Zero resistance and the Meissner effect

Superconductivity was discovered in 1911 by Kamerlingh-Onnes when he first observed the disappearance of electrical resistance in a mercury wire at a temperature of 4.2 K [15]. This was enabled by the successful liquefaction of helium by Kamerlingh-Onnes a few years prior that meant temperatures as low as 1.5 K could be reached experimentally. Mercury was chosen for the initial measurements in part because it could be made extremely pure via repeated distillation. In 1912, tin and lead were also found to superconduct, at temperatures of 3.8 K and 7.2 K, respectively [16].

The transition of DC electrical resistance of a superconductor from a finite value to zero at a critical temperature T_c represents the first phenomenological characteristic of superconductivity. In the absence of resistance, a persistent DC electrical current will continue to circulate indefinitely in a closed loop as long as the material remains in the superconducting state.

The second hallmark of superconductivity was discovered in 1933 when Meissner and Ochsenfeld observed perfect diamagnetism in a superconductor. When a superconductor is cooled below T_c, magnetic flux is expelled completely from the interior of the sample, except for a thin layer within the surface characterised by the London penetration depth λ_L [17]. This magnetic behaviour became known as the Meissner effect, demonstrating once again that superconductivity was indeed an entirely novel thermodynamic phenomenon and not simply perfect conductivity. In a perfect conductor, field lines would instead be retained or "frozen-in" as the conductor is cooled in field to below T_c, as shown in Figure 2.1.
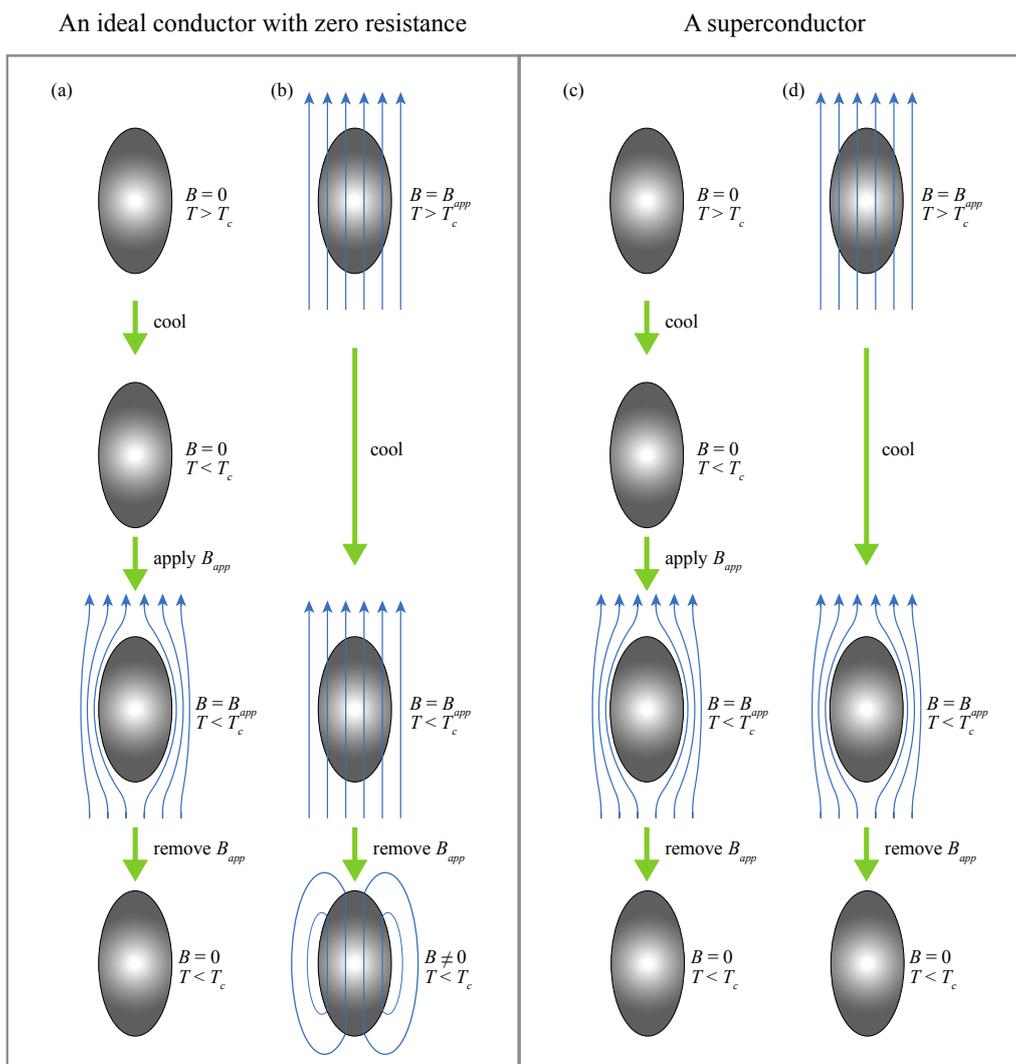
Figure 2.1. Comparison of the response of a perfect conductor, in (a) and (b), and a superconductor, in (c) and (d), to a small applied magnetic field B_{app} when cooled below the critical temperature T_c.

In addition, superconductivity is suppressed in the presence of an applied magnetic field H exceeding the critical magnetic field H_c of the superconductor. H_c can be related to the difference between the Gibbs free energy densities of the superconducting and normal states by Equation (2.1), which applies to a thin superconductor in a parallel field.

$$\frac{\mu_0 H_c{}^2(T)}{2} = G_n(T) - G_s(T) \tag{2.1}$$

Where μ_0 is the permeability of free space, H_c is the critical field, and $G_n(T)$ and $G_s(T)$ are the free energy densities of the normal and superconducting states, respectively. The superconducting state is the lower energy state, so is favoured over the normal state.

The upper limits in temperature, field and current density define the critical surface shown in Figure 2.2, indicating whether a superconductor is in the superconducting state or the normal state for a given set of conditions.

Phase diagram showing the boundaries that limit superconductivity in *J-H-T* space removed for copyright reasons.

Figure 2.2. The phase diagram of a superconducting material, showing the parameter space typically occupied by the superconducting states of low temperature superconductors (LTS) and high temperature superconductors (HTS) [18].

2.1.2. Type I and Type II superconductors

There are several ways of classifying superconductors, including distinct categorisations such as by their response to an external magnetic field (type I or type II) and their material constituents (elements, alloys or ceramics) as well as more ambiguous categorisations such as their critical temperature (low temperature or high temperature) and whether they can be explained by the BCS theory (conventional or unconventional).

As more superconductors were discovered, it became clear they exhibited two types of magnetic behaviour. Type I superconductors (comprised mainly of metals including aluminium, indium and tin), which were the first superconductors to be discovered, exhibit the Meissner effect below the critical field H_c and transition directly from the superconducting state into the normal state at H_c, where the field fully penetrates the interior of the sample.

On the other hand, type II superconductors (comprised mainly of alloys and compounds like niobium-titanium NbTi, niobium-tin Nb_3Sn, magnesium diboride MgB_2 and the rare earth cuprates) have a lower and upper critical field, H_{c1} and H_{c2} respectively, as shown in Figure 2.3. Below H_{c1}, a type II superconductor behaves like type I, expelling all magnetic flux. Above H_{c2}, field penetrates fully and uniformly, and the superconductor is driven normal.

However, between H_{c1} and H_{c2}, magnetic field partially penetrates the material in the form of individual/quantised vortices of flux in multiples of $\Phi_0 = h/2e = 2.1 \times 10^{-15}$ Wb, where h is the Planck constant and e is the electron charge. In this case, the superconductor enters a so-called "mixed state" that is energetically more favourable than having all of the flux expelled from its interior.

H-T phase diagrams for both type I and type II superconductors, showing the Meissner State in type I and the Meissner and Mixed States in type II, removed for copyright reasons.

Figure 2.3. *H–T* phase diagrams of type I and type II superconductors [19]. The insets illustrate the behaviour of flux lines in the different states.

2.1.3. Characteristic length scales: penetration depth and coherence length

The difference between type I and type II superconductors can be understood in terms of characteristic length scales and surface energy. The important length scales here are the penetration depth λ and the coherence length ξ.

First proposed by F. and H. London in their phenomenological theory [20], the penetration depth λ_L governs the penetration of magnetic flux into a superconductor and determines the finite surface layer over which screening currents flow to reduce the flux density to zero within the interior of the superconductor. The field decay with distance from the surface is given by:

$$B(x) = B_{app}e^{-x/\lambda_L} \tag{2.2}$$

Where $B(x)$ is the magnetic field at distance x from the surface, $B_{app} = \mu_0 H$ is the magnitude of the external applied field and λ_L is the characteristic London penetration depth.

The London penetration depth depends on the superconducting electron number density:

$$\lambda_L = \sqrt{\frac{mc^2}{4\pi n_s e^2}} \tag{2.3}$$

Where m is the mass of the superconducting electrons, c is the speed of light in vacuum, n_s is the superconducting electron number density and e is the electronic charge.

As a result of the temperature dependence of n_s, the penetration depth has a temperature dependence, which is described approximately by:

$$\lambda(T) = \lambda(0)[1 - (T/T_c)^4]^{-1/2} \tag{2.4}$$

Where $\lambda(T)$ is the penetration depth at temperature T, $\lambda(0)$ is the penetration depth at $T = 0$ K and T_c is the critical temperature of the superconductor.

The superconducting wavefunction also has a characteristic length scale over which the superconducting order parameter ψ and the superconducting state transitions into the normal state, since this cannot be arbitrarily small. The characteristic length scale is known as the coherence length ξ, which can be estimated from the uncertainty principle [21]:

$$\xi_0 = \frac{\hbar v_f}{2E_g} \tag{2.5}$$

Where $\hbar$ is the reduced Planck's constant, v_F is the Fermi velocity for the material and E_g is the superconducting energy gap.

The Ginzburg-Landau theory of superconductivity introduced subsequently [22], in addition to a complex pseudo-wavefunction ψ to describe the spatial extent of superconducting electrons, the Ginzburg-Landau penetration depth $\lambda(T)$ and coherence length $\xi(T)$, which incorporated temperature dependence as shown in Equation (2.6).

$$\xi(T) = \sqrt{\frac{\hbar}{2m^*|\alpha(T)|}} \tag{2.6}$$

Where $\alpha(T)$ is an expansion coefficient dependent on temperature. In a pure superconductor far below its T_c, one gets $\xi \approx \xi_0$; but they diverge near T_c.

The difference between type I and type II superconductors arises from the sign of the surface energy at the superconducting–normal interface, as shown in Table 2.1, and can be understood in terms of minimising the net energy of the system in response to a magnetic field $H > H_c$ (or $H > H_{c1}$). Magnetic flux penetrating the superconductor, as governed by the penetration depth λ, results in an increase in the magnetic energy of the system. On the other hand, the formation of superconducting electron pairs, as governed by the coherence length ξ, results in a decrease in energy.

As a result of the negative surface energy and surface tension when ξ becomes considerably shorter than λ, it is energetically favourable for type II superconductors to enter the mixed state between H_{c1} and H_{c2} as they remain superconducting. To minimise the free energy, field would naturally penetrate the superconductor as a regular triangular array of flux vortices, as shown in Figure 2.5. Inside these filament-like vortices, each containing a flux quantum $\Phi_0 = h/2e = 2.1 \times 10^{-15}$ T m^2 over a length scale on the order of ξ, the flux density is high, and the superconductor reverts back to the normal state. Each vortex is surrounded by a circulating shielding current that allows the rest of the material to remain in the superconducting state.

In this context, a useful ratio is the Ginzburg-Landau parameter, given by $\kappa = \lambda/\xi$, which divides superconductors into type I and type II according to Table 2.1 and as illustrated in Figure 2.4.

Table 2.1. Ginzburg-Landau ratio and surface energy associated with a superconducting–normal interface.

	$\kappa = \lambda/\xi$	Surface energy	Note	Examples
Type I	$< 1/\sqrt{2}$	> 0	Energetically favourable to have a single normal domain with minimum surface to volume ratio	Al, Sn, Hg, Pb
Type II	$> 1/\sqrt{2}$	< 0	Energetically favourable to maximise interface area between superconducting and normal regions and form a mixed state	Nb, NbTi, Nb$_3$Sn, YBCO

Diagrams showing the relative magnitudes of the penetration depth and coherence length in type I and type II superconductors, removed for copyright reasons.

Figure 2.4. Relative magnitudes of the penetration depth λ and coherence length ξ in (a) type I and (b) type II superconductors [23], illustrating the degree of electromagnetic screening and quantum correlation which are governed by λ and ξ, respectively. The magnetic field and Cooper pair wavefunction are shown by the solid and dashed lines, respectively, as a function of depth r below the surface of the superconductor.

For reference, values of $\lambda(0)$ for some typical superconductors are as follows [23], [24]: Al = 16 nm, Nb = 39 nm, YBCO = 140 nm [25]. In comparison, values of ξ_0 for these materials are: Al = 1600 nm, Nb = 38 nm, YBCO = 1.7 nm.

The flux vortices entering a type II superconductor can be pinned by disorder in the superconducting matrix. In the absence of any resistance to their motion, the flux vortices arrange themselves periodically due to mutual repulsion, similar to the repulsion between otherwise unconstrained parallel bar magnets, forming the so-called Abrikosov vortex lattice (named after Abrikosov, who published a theoretical paper regarding the then new class of superconductors in 1957 [26]). The vortex lattice can be observed visually in experiments, as shown in Figure 2.5(d) for a $NbSe_2$ superconductor at 0.4 K.

Diagrams showing flux vortices in the mixed state of a type II superconductor and STM image of the vortex lattice in a NbSe2 superconductor, removed for copyright reasons.

Figure 2.5. (a) Mixed state in a type II superconductor, showing the lattice of flux vortices and normal cores surrounded by circulating supercurrent loops [27]. (b) Variation of superconducting electron density n_s with position. (c) Variation of flux density B with position. (d) Scanning tunnelling microscopy (STM) topographic image of the vortex lattice in a $NbSe_2$ superconductor at 0.5 T and 0.4 K [28].

The upper critical field H_{c2} is ultimately set by when the flux vortices overlap. Since H_{c2} is usually orders of magnitude larger than H_c, type II superconductors can sustain significantly

higher currents in comparison to type I superconductors, making them the obvious choice for practical applications. For instance, H_c of lead (one of the strongest type I superconductors in terms of electron pairing energy) has been measured to be less than 0.1 T towards 0 K, whereas the H_{c2} of YBCO can be up to 100 T near 0 K. All known high temperature superconductors are type II superconductors.

2.2.   Type II superconductors

2.2.1.   Magnetisation curves

Reversible and irreversible magnetisation curves of a type II superconductor are shown in Figure 2.6. The magnetisation M is reversible if the superconductor is ideal and free of defects, meaning no field will remain within the sample once the external field is removed. However, if the superconductor contains defects of size comparable to or larger than the coherence length, flux lines can become pinned at these locations, resulting in irreversibility and remanent magnetisation, i.e. a trapped field.

When a field $H < H_{c1}$ is applied, shielding currents flow on the surface of the superconductor over a thickness governed by λ such that $B = 0$ inside the superconductor, resulting in perfect diamagnetism. This culminates in the initial linear region on the M–H curve, which has a slope of -1 if demagnetisation effects are negligible, i.e. $M = -\mu_0 H$.

For a field $H_{c1} < H < H_{c2}$, irreversible magnetisation starts to deviate from the reversible case due to flux vortices interacting with the pinning sites. On the irreversible M_{irr} curve, the penetration field H_p represents the applied field at which the field reaches the centre of the superconductor and coincides with the point of inflexion on the M–H curve. For $H > H_p$, magnetisation starts to decrease as a result of a reduction in the critical current density with increasing field.

Instead of H_{c2}, the irreversible loop actually closes at the irreversibility field $H_{irr} \leq H_{c2}$, above which the thermal fluctuations dominate such that flux pinning becomes ineffective and flux lines start to move freely. Therefore, the irreversible region between H_{irr} and $-H_{irr}$ can be considered as the M–H space usable by practical applications.
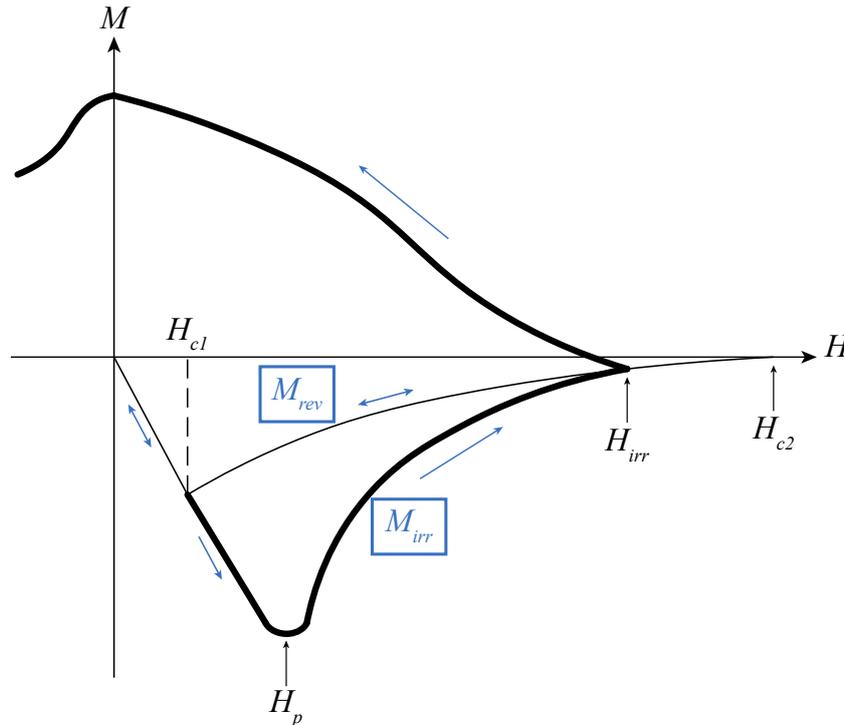
Figure 2.6. Schematic of the reversible (thin line) and irreversible magnetisation (thick line), denoted by M_{rev} and M_{irr} respectively, of a type II superconductor.

2.2.2. Flux pinning and critical current density

The critical current density J_c describes the maximum DC current that can be transported by a unit area of the superconductor with zero resistance and without depinning the flux lines. It is, therefore, one of the most important properties of any superconductor for an engineer. In the absence of defects or imperfections, also known as pinning centres, flux density will be uniform across the superconductor with evenly distributed vortices in the mixed state forming the triangular lattice shown in Figure 2.5. However, a flux density gradient will be established if pinning is present, as the material can sustain magnetisation currents.

Equation (2.7) shows the pinning potential U_p, which is the energy saving in having a pinned flux vortex instead of a free vortex line, as a product of the condensation energy E of the superconducting state and the volume V over which the pinning interaction takes place. The dependence of U_p on the thermodynamic critical field H_c, coherence length ξ and average diameter of the non-superconducting particle d is shown in Equation (2.7).

$$U_p = \Delta E \times V = \frac{1}{2}\mu_0 H_c{}^2 \times \pi\xi^2 d \tag{2.7}$$

The flux pinning force f_p can subsequently be derived by considering the force required to eject a flux line segment, i.e. by moving it over a distance of ξ:

$$f_p = \frac{U_p}{\xi} = \frac{1}{2}\mu_0 H_c{}^2 \pi\xi d \tag{2.8}$$

For a superconductor with N number of pinning centres per unit volume, the net pinning force F_p of the bulk material is given by:

$$F_p = N \times f_p \tag{2.9}$$

The pinning force F_p must be greater than or equal to the Lorentz force F_L to resist electromagnetic driving forces and prevent flux motion. Otherwise, the movement of flux lines would generate a voltage according to Faraday's law and result in a non-zero resistance in the superconductor. Balancing F_L and F_p, namely Equations (2.9) and (2.10), yields J_c in Equation (2.11) [29].

$$F_L = J \times B \tag{2.10}$$

$$J_c = \frac{N\mu_0 H_c{}^2 \pi\xi d}{2B} \tag{2.11}$$

It is clear from Equation (2.11) that the dimension of the pinning centres, represented by d, is key in determining J_c. While it is generally considered a pinning centre is most effective when its size $d \approx \xi$, structures much larger than ξ are also useful, an example of this being the $REBa_2Cu_3O_{7-\delta}/RE_2BaCuO_5$ (RE-123/RE-211) interface in the rare earth cuprates. In reality, the interfacial defects generated by the presence of relatively large, non-superconducting RE-211 precipitates in the RE-123 superconducting phase matrix have been shown to aid flux pinning in (RE)BCO materials. The microstructure and phases present in typical (RE)BCO bulk materials will be presented in detail in Sections 2.3.2 and 2.5.4.

It is important to note that the type, size and density of defects in type II superconductors, and hence the flux pinning strength of the material, can be varied by fine tuning the fabrication process. This ultimately means that J_c can be considered an extrinsic property, unlike T_c or H_c.

Melt-processed (RE)BCO samples typically contain several microstructural defects that assist in flux pinning, including twin planes, stacking faults, cracks, oxygen-deficient regions, dislocations and non-superconducting inclusions [29]. Flux pinning as a result of the non-superconducting RE-211 particles is arguably discussed the most extensively in the literature, as excess RE-211 can be added in a controlled manner and dispersed throughout the RE-123 matrix in the form of discrete particles of controlled size. The influence of Y-211 particles has been confirmed empirically in YBCO, as shown in Figure 2.7, where J_c was improved by increasing the overall Y-211 content (where V_f = volume fraction) and by increasing the effective Y-123/Y-211 interfacial area with finer Y-211 particles [30].

Plots showing the measured dependence of J_c-B on Y-211 content and the measured dependence of J_c on effective interface area, removed for copyright reasons.

Figure 2.7. (a) Dependence of J_c on Y-211 content and (b) dependence of J_c on effective interface area V_f/d of Y-211 inclusions, measured from YBCO bulk superconductors with different Y-211 contents and particle sizes [30].

2.2.3. The Bean model

The Bean critical state model [31] was the first model to successfully describe the irreversible magnetisation of practical type II superconductors and has successfully depicted the positional variation of flux density B in relation to J_c. The underlying concept of this model is that a superconductor can carry a macroscopic supercurrent density J, which is equal to either $\pm J_c$ or 0 depending on how field H is applied ($J = \pm J_c$ in regions that have experienced an electric field E and $J = 0$ in regions where E has remained zero). In the Bean model, J_c is considered to be constant with a magnitude that is independent of B.

Figure 2.8 illustrates the field and current distributions in an infinite slab of superconductor, with a width of $2a$ in the x-direction, according to the Bean model. H is applied along the z-direction.

As field penetrates the superconductor when H exceeds H_{c1}, pinning sites confine the flux to the exterior region of the superconductor, resulting in a flux density gradient $dB/dx = \mu_0 J_c$, as shown in Figure 2.8(a). As H is increased further, field penetrates further inwards, but the same gradient applies due to the constant J_c. The full penetration field $B^* = \mu_0 J_c a$ is shown in the figure. It can be seen in Figure 2.8(e) that a field becomes trapped in the superconductor once the external field has been completely removed.

In practice, if the pinning force is independent of B, J_c will instead exhibit a $1/B$ dependence, as indicated by Equation (2.11). To account for this behaviour, Kim and Anderson [32], [33] later modified the Bean model to include a more realistic $J_c(B)$ dependence, given by:

$$J_c(B,T) = \frac{J_0(T)}{1 + B/B_0} \tag{2.12}$$

Where $J_0(T)$ is the critical current density at zero field, B is the local field and B_0 is a model parameter dependent on the material and determined by experiment.

Despite its simplifications, the Bean model is, remarkably, still an excellent tool for making approximations and for analysing the behaviour of a superconductor in response to an applied field.
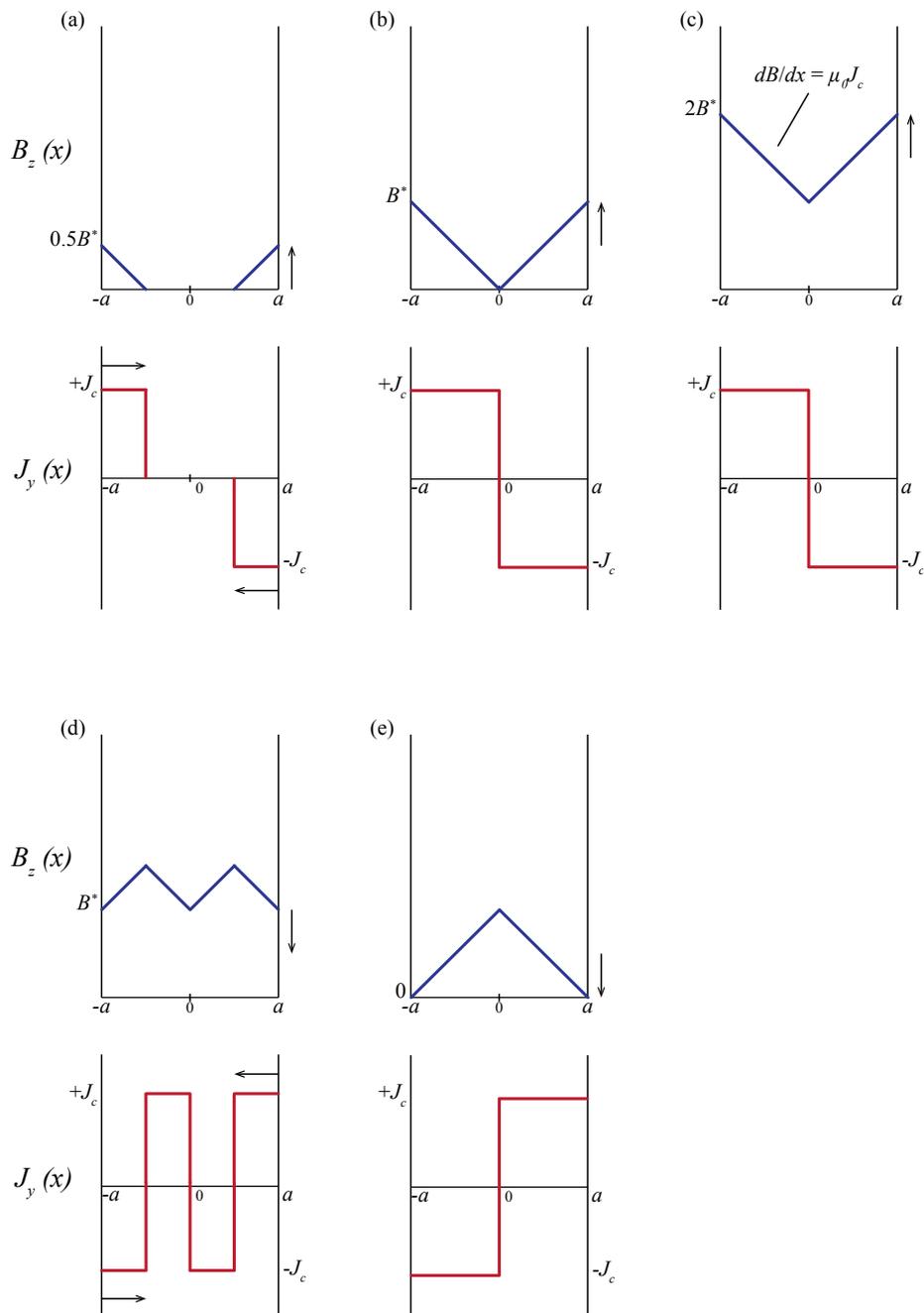
Figure 2.8. Distributions of B_z and J_y in an infinitely long slab of superconductor (width $2a$ along the x-axis) with increasing and decreasing external field applied parallel to the z-axis. The plots in (e) show a remanent field trapped in the superconductor as the external field is removed completely.

2.2.4.   Determining J_c using the extended Bean model

T_c and J_c of bulk superconductors are frequently determined using a superconducting quantum interference device (SQUID), which measures the magnetic moment of a small specimen of the superconductor as a function of temperature T and applied field $\mu_0 H$.

T_c is obtained from the onset of the Meissner effect during temperature sweeps and is often quoted with a transition width ΔT_c. J_c for an infinitely long specimen with a cross sectional area of $a \times b$ is calculated from the field sweeps using the extended Bean model [34]:

$$J_c(H) = \frac{2\Delta M(H)}{a\left(1 - {}^{a}\!/_{3b}\right)} \tag{2.13}$$

Where $\Delta M = M(H)^+ - M(H)^-$ is the width of the M–H hysteresis loop. The equation can be adapted to the form below to calculate J_c (in A/cm^2) directly from experimental data acquired using the SQUID:

$$J_c = \frac{20 \times 10^{-5}\Delta m}{a\left(1 - {}^{a}\!/_{3b}\right)abc} \tag{2.14}$$

Where $\Delta m = m(H)^+ - m(H)^-$ is the difference between the magnetic moments (in emu), and a, b and c are the dimensions of the SQUID specimen (in cm) in the respective crystallographic directions. a is defined as the shorter side of the specimen in the ab direction such that $a \leq b$.

2.3.   High temperature superconductors in bulk form

The discovery of high temperature superconductivity in 1986 by Bednorz and Müller [1], when they observed superconductivity at 35 K in polycrystalline $La_{5-x}Ba_xCu_5O_{5(3-y)}$, was followed by the synthesis of $YBa_2CuO_{7-\delta}$ superconductors in 1987 by Wu and Chu [3], which exhibited a T_c of 93 K. X-ray powder diffraction on the Y-Ba-Cu-O compound showed that the superconducting phase had an orthorhombic, distorted, oxygen-deficient perovskite structure of stoichiometry $YBa_2Cu_3O_{7-\delta}$ ($\delta = 0.1 \pm 0.05$), similar to some compositions of the La-Ba-Cu-O system [35]. These achievements paved the way for a much broader range of practical applications than what traditional low-temperature superconductors could offer given the T_c of

these new systems exceeded 77 K, which meant these materials could be cooled easily and economically with liquid nitrogen (LN$_2$) or commercial cryocoolers. The superconductors that were discovered previously had to be cooled primarily with liquid helium (LHe), which is far less economical.

Since then, researchers have observed superconductivity in other cuprates such as BiSrCaCu$_y$O$_x$ (T_c = 105 K) [4], TlCaBaCu$_2$O$_x$ (T_c = 125 K) [5] and HgBa$_2$Ca$_2$Cu$_3$O$_{8+\delta}$ (T_c = 164 K at 31 GPa) [6]. The more recent discoveries of superconductivity in intermetallic magnesium diboride MgB$_2$ with a T_c of 39 K [36] and iron-based superconductors with a T_c of 55 K [37] add to the family of high temperature superconductors (HTS).

Diagram showing the year of discovery and critical temperature of each superconductor material, removed for copyright reasons.

Figure 2.9. Evolution of the various families of superconducting materials, showing the year of discovery and the critical temperature recorded [38]. Superconductors that conform to the BCS theory are represented by green circles. The cuprates are represented by blue diamonds.

HTS, when manufactured in large, bulk form, are highly attractive for quasi-permanent magnet applications. A large, trapped field of several tesla can be achieved with bulk superconducting magnets of only a few centimetres in diameter as a result of the flow of macroscopic

supercurrent. As shown in Figure 2.10, the combination of high field, compactness and safety is simply not possible in conventional permanent magnets or electromagnets (conventional or superconducting).

According to the Bean model, the maximum trapped field $B_{trapped}$ that can be achieved at the centre of a fully magnetised cylindrical bulk superconductor as a result of the induced persistent currents is given by:

$$B_{trapped} = A\mu_0 J_c R \tag{2.15}$$

Where A is a geometrical factor (which is equal to 1 for an infinitely long cylinder), μ_0 is the permeability of free space, J_c is the critical current density and R is the radius of the superconductor.

Equation (2.15) shows that $B_{trapped}$ can in fact be increased by enhancing J_c (either by improving the flux pinning at a certain temperature or by lowering the sample temperature) and enlarging the size of the single grain, which is why a great amount of research effort has been focussed on these areas of materials processing.

For a bulk superconductor of finite thickness, the surface trapped field $B_{surface}$ is given by Equation (2.16).

$$B_{surface} = \frac{\mu_0 J_c R}{2} \frac{t}{R} \ln\left(\frac{R + \sqrt{R^2 + t^2}}{t}\right) \tag{2.16}$$

Where R and t are the radius and thickness, respectively, of the superconductor disc.
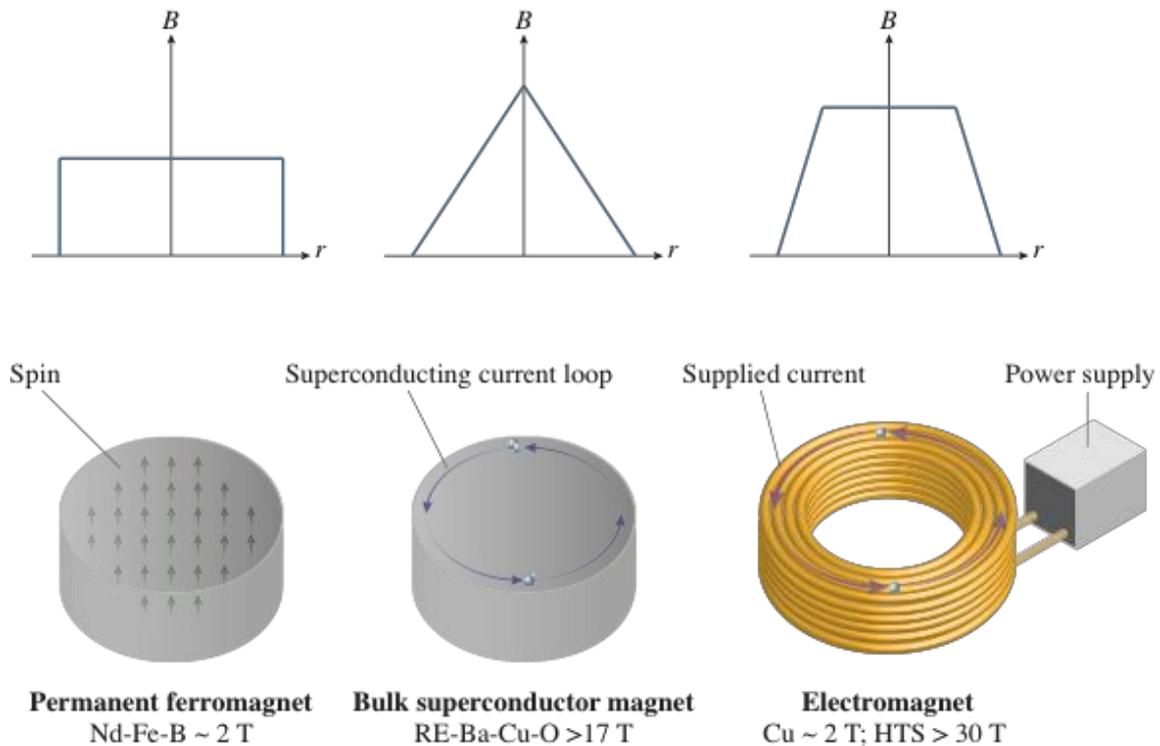
Figure 2.10. Comparison of the field profile and peak field from each type of strong magnet, as well as the underlying mechanism responsible for generating/sustaining the magnetic field.

2.3.1. Candidate materials

It is clear, from Table 2.2, that YBCO, and the (RE)BCO family in general, are the most promising cuprates for high-field permanent magnet applications due to the significant processing challenges and limited properties associated with Bi-based and Tl-based materials. However, a major challenge lies in that it is highly undesirable to fabricate these materials as polycrystalline samples, for instance, through conventional solid-state reaction, but that they must be fabricated as single domains to minimise the number of large-angle grain boundaries and to maximise the $J_c \times R$ product.

Table 2.3 compares MgB_2 and Fe-based superconductors, the other highly promising HTS materials, with (RE)BCO single grains. Despite possessing some disadvantages, it can be seen that single-grain (RE)BCO also has obvious advantages making it a strong candidate for a variety of niche applications in the near future.

Table 2.2. Critical temperature T_c and irreversibility field H_{irr} of various cuprates with potential for high-field applications [39].

Material	T_c (K)	$\mu_0 H_{irr}$ (T) at 77 K	Main drawbacks
$YBa_2Cu_3O_{7-\delta}$ (YBCO or Y-123)	92	5	Small critical grain boundary angle of $3 - 5$ º
$Bi_2Sr_2CaCu_2O_x$ (Bi-2212)	90	< 0.1	Low H_{irr} limits applications to lower fields
$Bi_2Sr_2Ca_2Cu_3O_y$ (Bi-2223)	105	0.3	Low H_{irr} limits applications to lower fields
$TlCa_2Ba_2Cu_3O_z$ (Tl-1223)	120	4	Tl is toxic and oxides are volatile J_c is usually low

2.3.2. Processing of (RE)BCO single grains

It is well established that the number of practical applications of polycrystalline (RE)BCO bulk superconductors prepared through simple sintering is limited by the weak link nature of their grain boundaries [40]–[42], as J_c across a grain boundary deteriorates rapidly with increasing misorientation angle between the individual high-J_c grains.

Other properties of grain boundaries, such as relatively low apparent density and presence of a secondary phase [43], also reduce the flow of supercurrent. For reference, the bulk J_c measured in polycrystalline samples is typically on the order of 10^6 A/m^2 at 77 K and in zero field, which is around two orders of magnitude less than that of single grains.

Table 2.3. Comparison of MgB_2 and Fe-based superconductors with (RE)BCO [44].

	(RE)BCO	MgB_2	Fe-based superconductors
T_c	93 K	39 K	55 K
Advantages	High T_c and H_{irr}	Easy fabrication	Easy fabrication
	Very high trapped fields have been demonstrated (> 17 T at ~ 30 K)	High trapped fields have been demonstrated (5.4 T at ~ 12 K [45])	Weak field dependence of J_c suggests very high trapped fields can be achieved in large samples
	Reliable and large batches of samples already available from commercial suppliers	J_c not hindered by weak-link grain boundaries	Robust to impurities
		Small anisotropy	
		Low density and therefore light weight	
Disadvantages	Time-consuming production	Relatively low H_{irr} (~ 10 T at 20 K) and H_{c2} (0)	Toxicity
	Single grain growth is very sensitive		Low measured trapped fields so far (~ 1 T at 5 K [46])
		Sensitive to impurities	
	Limit on maximum grain size		

Grain boundaries are intrinsically weak links in (RE)BCO superconductors due to the two-dimensional nature of their crystal structure and their small coherence length. Cuprate superconductors are made of superconducting copper oxide (CuO_2) planes separated by insulating layers containing metallic ions such as Y^{3+} and Ba^{2+}. As supercurrents propagate easily within the CuO_2 planes, yet adjacent CuO_2 planes are weakly coupled, conductivity is much higher parallel to the CuO_2 planes (usually referred to as the *ab* planes) than perpendicular to the planes (usually referred to as the *c* direction), resulting in significant anisotropy in the superconducting properties, particularly J_c. The degree of anisotropy is evident in the strong angular dependence of J_c on the direction of applied field in YBCO coated conductors [47], [48]. Consequently, a (RE)BCO bulk superconductor needs to be fabricated

in the form of a well-connected, large, single grain with a well-defined orientation for the generation of high and uniform J_c.

The most commonly used and well-established melt processing technique to produce well-oriented (RE)BCO single grains is top seeded melt growth (TSMG). All melt processing techniques are based on the peritectic reaction shown in Equation (2.17), which occurs at a temperature T_p dependent on the RE element. T_p ranges from approximately 960 ºC in Yb to 1068 ºC in La, with Y and Gd, two of the most commonly used RE systems, at 1005 ºC and 1030 ºC, respectively [49].

$$2(RE)Ba_2Cu_3O_{7-\delta}(s) \leftrightarrow (RE)_2BaCuO_5(s) + Ba_3Cu_5O_8(l) + yO_2(g) \quad (2.17)$$
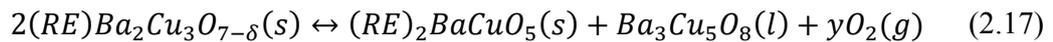
Where s denotes a solid phase, l denotes a liquid phase and g denotes a gaseous phase.

TSMG, which exploits this peritectic reaction/solidification, can be summarised in a few steps: mixing and pressing, seeding, melt-processing and oxygenation [50]. Each step is described in detail below.

Firstly, precursor powders of the required composition, of which examples are given in Table 2.4, are mixed together using a mixing device, such as a pestle and mortar. The powders may also be milled if the precursor particles are too large. The excess RE-211 phase added to the starting composition provides additional non-superconducting particles in the resultant bulk superconductors as that would form effective flux pinning centres in the single grains. Additional dopants may also be added, for instance, incorporating Pt or CeO_2 to refine the size of the RE-211 particles or incorporating Ag_2O to improve the fracture toughness of the grown bulk samples. The evenly mixed powder is then pressed into pellets of the desired size using a die or a mould, taking into account shrinkage during melt-processing.

Secondly, a small seed crystal (typically 2 mm × 2 mm × 1 mm in dimensions) with a similar crystal structure and lattice constants but a higher melting temperature is placed on the top surface of the pressed pellet as shown in Figure 2.11. The seed crystal forms an epitaxial nucleation site to initiate large, single-grain growth. The sample/seed assembly is then placed into a furnace for melt-processing.

Thirdly, the precursor assembly is heat treated by following a particular temperature profile. In general, the pellet is heated to a few degrees celsius above T_p, allowing the RE-123 to

decompose into a melt, and then cooled slowly back down through T_p (typically at rates between 0.2 and 0.8 ºC/h) to enable c-axis oriented growth of a RE-123 matrix from the seed during the peritectic growth window.

Lastly, the as-grown single domains are oxygenated, i.e. annealed in an oxygen atmosphere, for several days (typically 7 – 10 days) to facilitate the tetragonal (non-superconducting) to orthorhombic (superconducting) transformation. A well-oxygenated sample would undergo an increase in weight of around 1 %.

The resultant bulk superconductor is a c-axis-oriented RE-123 matrix containing distributed RE-211 inclusions as well as microstructural defects from the growth and oxygenation processes, such as pores and cracks. These will be discussed in more detail in Section 2.5.4.
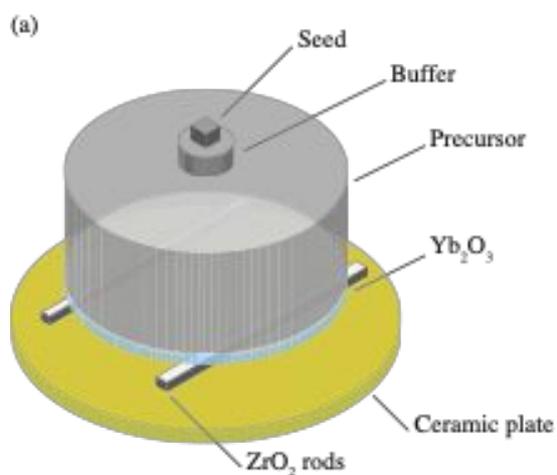
Figure 2.11. (a) Typical assembly (pre-melt-processing) used for TSMG. The buffer (optional) reduces the lattice mismatch between the seed and the precursor pellet. The ytterbium oxide (Yb$_2$O$_3$) layer prevents growth of sub-grains by lowering the T_p of the powder in its vicinity. (b) An example of the resultant fully-grown (RE)BCO single grain (post-melt-processing), which is 25 mm in diameter [51].

Table 2.4. Seeds and powder compositions that could be used for fabricating YBCO and GdBCO/Ag single grains.

	Seed	Powder composition (by weight)
YBCO	NdBCO crystal	$(75\% \ YBa_2Cu_3O_7 + 25\% \ Y_2BaCuO_5) +$ $0.5\% \ CeO_2$
	SmBCO crystal	
	Thin film NdBCO-MgO seed	
Ag-doped GdBCO	NdBCO-MgO "generic" seed crystal [52]	$(75\% \ GdBa_2Cu_3O_7 + 25\% \ Gd_2BaCuO_5) +$ $10\% \ Ag_2O + 0.1\% \ Pt$

2.3.3. Magnetisation techniques

A bulk superconductor itself first needs to be magnetised using an external field in order to be utilised as a quasi-permanent magnet, i.e. as a stable, standalone source of magnetic field. Three techniques are used commonly to achieve this: zero field cooling (ZFC), field cooling (FC) and pulsed field magnetisation (PFM), although the latter two are more practical than the first. These techniques can be understood from the Bean model, as shown in Figure 2.12.

In ZFC, the bulk superconductor is cooled to the operating temperature $T < T_c$ in zero field before the external field is applied and then removed gradually to establish a trapped field in the sample. In FC, the external field is applied with the bulk superconductor held at $T > T_c$, followed by cooling the sample to the operating temperature in the external field. The field is then removed to establish a trapped field. To fully magnetise the sample such that it traps the maximum field permissible by its J_c, ZFC requires $2 \times H_p$, where H_p is the penetration field, whereas FC requires an applied field of H_p.

FC is often used as a benchmark test in research settings to determine the maximum superconducting capability, and therefore the quality, of a sample – the maximum surface trapped field at 77 K has become the figure of merit. However, in practice, ZFC and FC require large magnetising coils and power supplies, making these charging techniques impractical for most engineering applications.

Diagrams showing the evolution of field inside a bulk superconductor during ZFC and FC removed for copyright reasons.
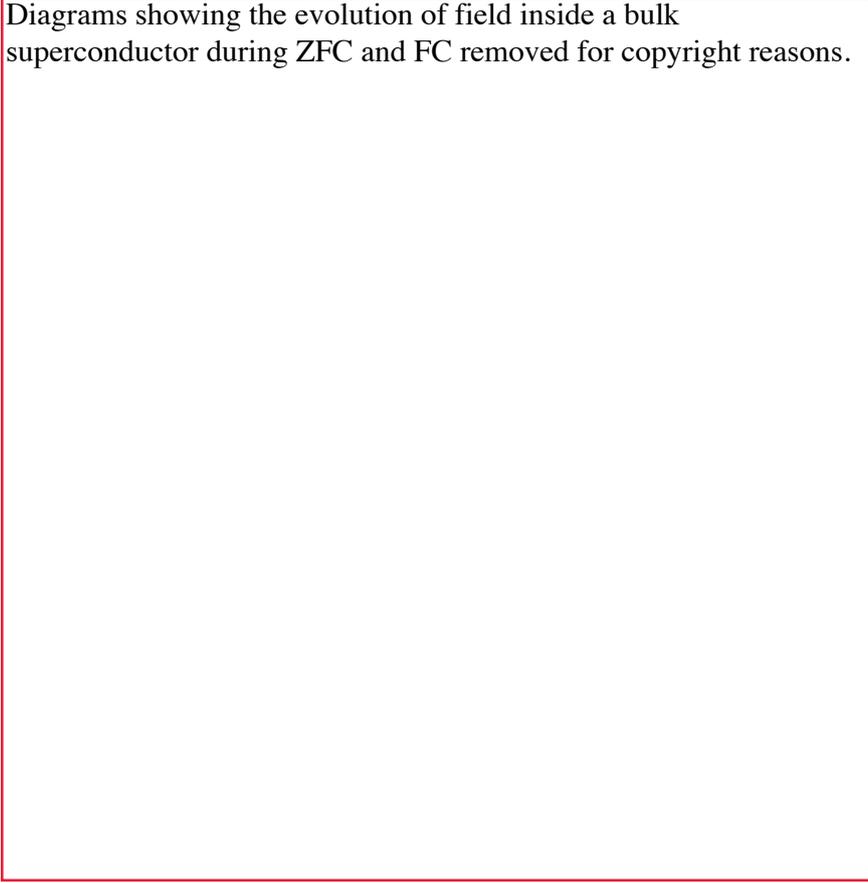
Figure 2.12. Field distributions during ZFC and FC magnetisation of a bulk superconductor, as approximated by the Bean model [50]. The field trapped after the removal of the external field is shown at the bottom.

Alternatively, PFM may be employed to magnetise a bulk superconductor. This is when a large magnetic field is applied to the superconductor in the form of a short pulse typically less than 1 s in duration while the sample is maintained at the operating temperature $T < T_c$. PFM usually requires an electronic control circuit with a capacitor bank capable of instantaneously discharging a large amount of stored energy through the magnetising coil. Due to the portability and relatively low cost of PFM charging facilities compared to large HTS magnetising coils required for ZFC and FC, PFM is generally considered the more practical option. Furthermore, high trapped fields of up to 5.2 T have been demonstrated using PFM [53], as shown in Figure 2.13.

It is important to note, however, that a major downside exists with magnetising and characterising bulk superconductors using PFM, namely the significant temperature rise in the samples as a result of the rapid dynamic movement of flux into and out of the samples. Consequently, trapped fields achieved with PFM are generally lower than the trapped field values achieved with FC on the same sample, although this difference in $B_{trapped}$ does decrease with increasing T.

Trapped field vs. time data from the 5.2 T trapped field experiment by Fujishiro *et al*. removed for copyright reasons.

Figure 2.13. Record trapped field of 5.2 T achieved by Fujishiro *et al.* [53] on a 45 mm diameter GdBCO sample using PFM. The inset in (a) shows the experimental set-up, where the GdBCO sample was attached to the cold stage of a GM cryocooler and magnetised using a solenoid coil submerged in LN_2.

2.4. Potential applications of (RE)BCO bulk superconductors

2.4.1. Magnetic levitation

One of the first applications proposed for (RE)BCO bulk superconductors was in stable magnetic levitation, which is only possible due to the unique ability of type II superconductors to pin magnetic flux [54]. Potential applications include levitated conveyor systems to minimise mechanical contact in clean rooms and magnetically levitated (MagLev) transport to carry passengers or cargos with minimal frictional losses. A cylindrical permanent magnet levitated above or suspended below a bulk superconductor also behaves as an ideal magnetic bearing as the magnet rotates freely about its axis of symmetry but has reasonable stiffness to lateral and vertical displacements [54].

The list of successful demonstrations over the years is substantial, as shown in Figure 2.14, which includes the levitation of a person on a simple platform [55], a 45 m-long Maglev evacuated tube transport test system with a 1 tonne levitation capability [56], a two-passenger prototype vehicle running across an 80 m track [57] and a 5 kWh flywheel energy storage system [58].

2.4.2. Trapped field magnets

The trapped fields achievable with (RE)BCO bulk superconductors can be an order of magnitude larger than the maximum field attainable by conventional iron-based permanent magnets of comparable size. This is illustrated by the measurement of trapped fields of over 17 T in single-grain (RE)BCO, as Tomita and Murakami demonstrated 17.24 T at 29 K in a stack of two 26.5 mm diameter YBCO discs [7] and Durrell *et al.* demonstrated 17.6 T at 26 K in a stack of two 24 mm diameter GdBCO/Ag bulk samples [8]. These record-setting single-grain bulk superconductor stacks are shown in Figure 2.15.

The high field-trapping ability makes single-grain (RE)BCO bulk superconductors an attractive alternative to permanent magnets in existing real-world applications, including firstly, in rotating machines, where an axial gap type synchronous machine utilising bulk GdBCO as rotor poles has been demonstrated by the Department of Marine Electronics and Mechanical Engineering, Tokyo University of Marine Science and Technology, for electric

ship propulsion [59], [60]; secondly, in magnetic separation, where the high field and steep magnetic gradient of bulk magnet systems have been utilised for the removal of ferromagnetic precipitates containing manganese and other heavy metal ions from waste water [61]; and thirdly, in compact NMR/MRI machines, where it has been shown annular bulk superconductors can be used for MR microscopy to produce clear images of small specimens such as a mouse embryo [61], [62]. Examples of these applications are shown in Figure 2.15.

Examples of demonstrated applications of magnetic levitation by HTS bulk superconductors, removed for copyright reasons.
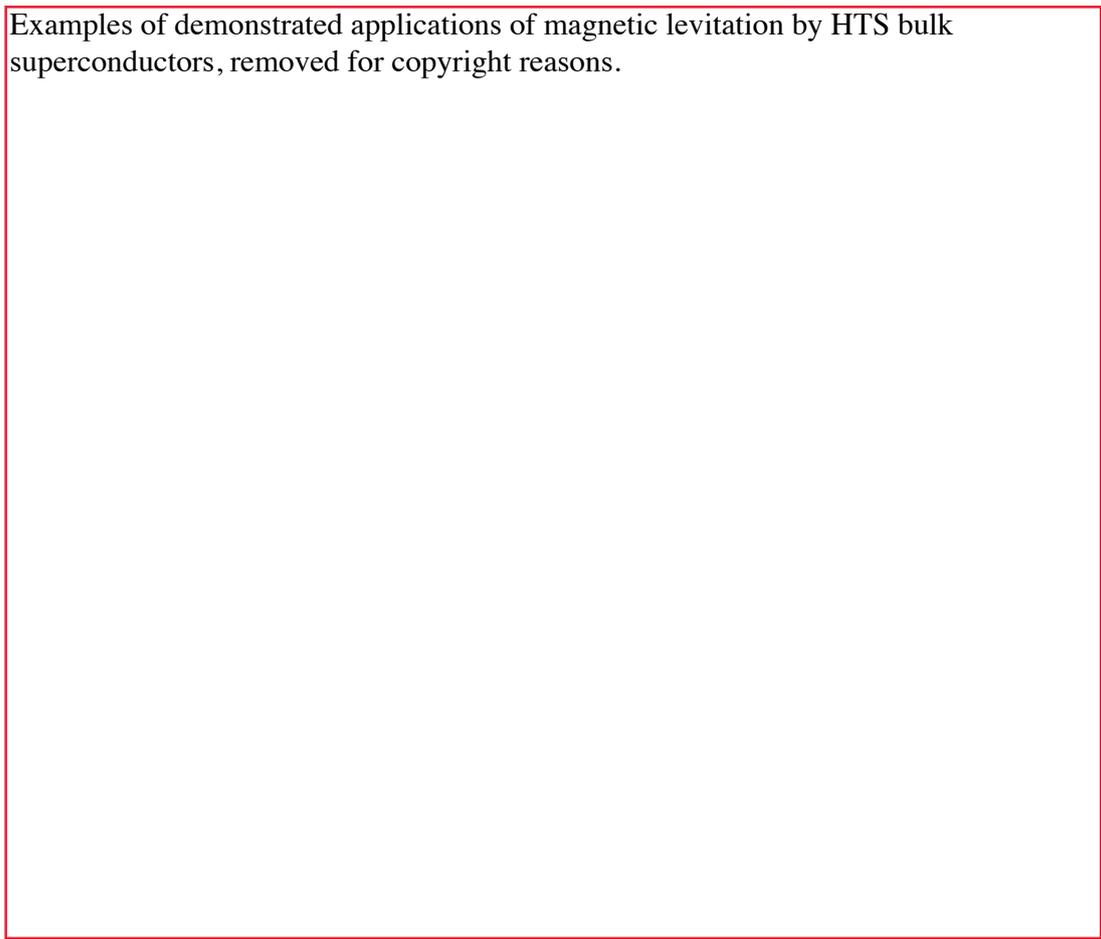
Figure 2.14. (a) A sumo wrestler levitated on a platform comprised of HTS bulk superconductors and Nd-Fe-B permanent magnets [55]. (b) The 45 m-long evacuated tube transport test system at Southwest Jiaotong University (SWJTU), China [63] (c) The 'SupraTrans' prototype vehicle at IFW Dresden, Germany. (d) The 5 kWh flywheel energy storage system manufactured by Boeing [58].

Examples of demonstrated applications of HTS bulk superconductor
trapped field magnets, removed for copyright reasons.

Figure 2.15. (a) Photograph of resin-impregnated YBCO discs, 26.5 mm in diameter, wrapped with carbon fibre fabric, which achieved 17.24 T between two samples in a stack configuration [7]. (b) Photograph of 24 mm diameter GdBCO/Ag discs enclosed in shrink-fit stainless-steel rings, which achieved 17.6 T between the two samples [8]. (c) A portable, single pole bulk magnet system that can generate over 2 T on the surface [64]. (d) Schematic illustration of a compact HTS motor containing eight GdBCO bulk magnets in the rotor plate [60]. (e) Ring-shaped EuBCO single grains used in the construction of a magnet system for high-resolution NMR spectroscopy [62]. (f) Schematic of the NMR magnet system, showing the cryostat and HTS bulk samples [62].

2.4.3. Magnetic shielding

Un-magnetised bulk superconductors can be used to screen or shield magnetic fields very efficiently either in systems requiring ultra-low background fields, i.e. in SQUIDs, or to protect a volume in space from the large stray fields of a nearby source, i.e. in accelerator projects or when working with superconducting magnets [9]. Magnetic shielding is only possible, again, due to the large flux density gradient of (RE)BCO bulk superconductors as a result of their high J_c.

2.4.4. Magnetic lensing

The shielding effect can also be used to concentrate an external magnetic field by designing superconductor geometries that deliberately bend flux lines towards a central region. A concentrated field of 12.4 T has been demonstrated at 20 K in a background field of 8 T with a GdBCO magnetic lens [65]. More recently, to sustain the effect of magnetic lensing after the removal of the background field, a hybrid trapped field magnet lens (HTFML) design was proposed and developed, using two types of bulk superconductor with significantly different T_c such that one sample is used as a lens and the other sample is used as a trapped field magnet to provide a stable field even after the background field has been removed [66].

2.5. Mechanical properties of (RE)BCO bulk superconductors

It is fairly well-established that one of the main concerns of scientists and engineers designing high-field applications of (RE)BCO bulk superconductors is the poor mechanical properties of these materials [9]. The perovskite structure of (RE)BCO makes them brittle, as the crystal lattice has limited dislocation mobility and exhibit little to no plasticity prior to a sudden and catastrophic mechanical failure. This behaviour is similar to that of other ceramic materials.

2.5.1. Lorentz force

A large Lorentz body force, as presented in Equation (2.10), which is the net force exerted by an electric and a magnetic field on a moving charged particle, develops during and after the

magnetisation of a (RE)BCO bulk superconductor due to the interaction between the circulating supercurrent and the corresponding trapped field. This radially outward force results in hoop and radial stresses that are tensile in nature and that become comparable to the tensile strength of the bulk samples at trapped fields of around 8 T to 10 T. In fact, the Lorentz force is also a concern for wound superconducting magnets for similar reasons.

Ren *et al.* derived analytically expressions for the hoop and radial stresses inside a fully magnetised bulk superconductor, as shown in Equations (2.18) and (2.19), with the following assumptions [67]:

    I.   The superconductor is a long cylinder, which simplifies the system to a 2D problem, loaded with only transversal forces such that solutions will be axially symmetric and end effects need not be considered.

    II.   The Bean model applies, i.e. J_c is constant and independent of field.

    III.   Stresses are within the elastic limit of the material and elastic properties are isotropic.

    IV.   The magnetic field is applied along the long axis.

$$\sigma_\theta = \mu_0 J_c{}^2 R^2 \left[\frac{7 + 5\nu}{24} - \frac{1 + 2\nu}{3} \left(\frac{r}{R}\right) + \frac{1 + 3\nu}{8} \left(\frac{r}{R}\right)^2 \right] \tag{2.18}$$

$$\sigma_r = \mu_0 J_c{}^2 R^2 \left[\frac{7 + 5\nu}{24} - \frac{2 + \nu}{3} \left(\frac{r}{R}\right) + \frac{3 + \nu}{8} \left(\frac{r}{R}\right)^2 \right] \tag{2.19}$$

Where σ_θ and σ_r are the hoop and radial stresses, respectively. R is the radius of the superconductor and r is the radial position, i.e. $r = 0$ at the centre of the sample. ν is the Poisson's ratio of the material.

The evolution of hoop stress across the bulk sample during field-cooling, as presented by Johansen [68], is shown in Figure 2.16.

The main takeaways from Equations (2.18), (2.19) and Figure 2.15 are, firstly, the maximum σ_θ and σ_r are always found at the centre of the sample; and secondly, the tensile stresses experienced by the sample scale with $J_c{}^2 R^2$, i.e. scaling quadratically with the trapped field $B_{trapped} = \mu_0 J_c R$. It is therefore clear the mechanical strength of a bulk superconductor, when unreinforced, limits the maximum field that can be trapped.

Diagrams showing the field and stress profiles as external field is ramped down, removed for copyright reasons.
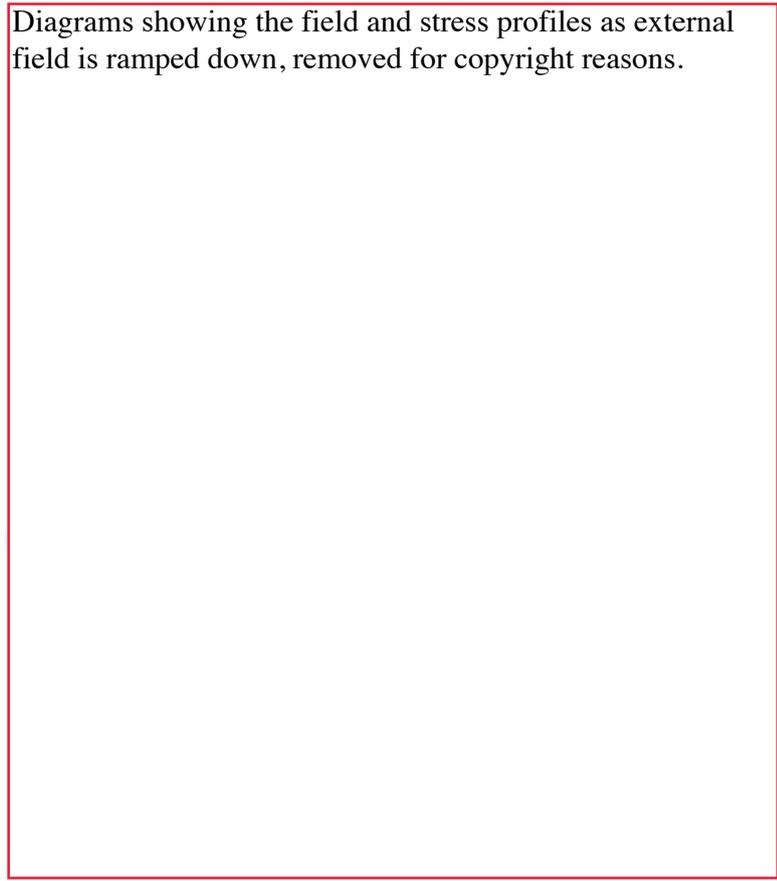
Figure 2.16. Evolution of the hoop stress profile as the external field B_a is decreased from the penetration field B_p to 0 to form the remanent state [68]. Here, the Bean model has been assumed and the stresses have been normalised by $\sigma_0 = B_p^2/2\mu_0$.

Ren *et al.* also showed that stresses can exceed the values given by Equations (2.18) and (2.19) during magnetisation, as supercurrents interact with both the self-field and external field. This explains why bulk samples tend to fail mechanically, i.e. crack, during magnetisation rather than at the end of the magnetisation process.

2.5.2. Fracture strength and fracture toughness

Strength and fracture toughness are both important measures of the mechanical behaviour of a material. From the perspective of atomic bonding and atomic structure, high strength is normally linked to strong directional bonding, high Peierls–Nabarro stresses and limited

dislocation mobility [69]. This restriction on plasticity, however, usually leads to low fracture toughness due to minimal stress relief.

Fracture can be categorised as ductile or brittle. Strength quantifies the resistance of a ductile material to permanent plastic deformation when stressed. This has an onset at the yield strength and often peaks at the ultimate tensile strength as a result of work hardening, which is commonly the case for metals. On the other hand, fracture toughness quantifies material resistance to the propagation of cracks – ductile materials tend to be tough as they yield, work harden and absorb a significant amount of energy before fracturing completely.

On the other hand, a brittle material behaves elastically up to the point at which catastrophic failure occurs, exhibiting little to no plastic deformation. In a brittle material, the strength is defined as where the sample fractures and fails. It is, however, not a direct indication of the fracture toughness of the material since it does not reveal the range of defects and flaws present in the sample that contributed to the fracture.

Cracks and defects concentrate stress in a material, with local stress rising sharply near defects. Kirsch was the first to derive a linear elastic solution for stresses around a circular hole in an infinite plate, which showed a factor of three concentration in stress at the hole when the plate was loaded uniaxially. In 1913, Inglis expanded this to an elliptical hole of any aspect ratio [70]. This was important as the ellipse could then be flattened to mirror a crack. However, this work prompted much discussion as the solution predicted the stress concentration could approach infinity for a thin crack, which was simply not physical as this meant the smallest stress could cause a material to fail if any crack was present.

In 1920, Griffith provided an energy-based failure criterion for the growth of cracks in brittle materials by considering the energy changes in the system as a result of incremental crack growth, and arrived at Equation (2.20) [71]. The theory states that a crack will grow/propagate spontaneously when the decrease in (or the release of) stored mechanical strain energy due to crack growth is greater than or equal to the increase in surface energy associated with new free surfaces being created by the crack. This also means when a crack exceeds a critical size, crack growth occurs without any additional energy input. It is, therefore, unstable, leading to the complete and catastrophic failure of the sample. The Griffith theory applies to elastic materials that fail in a brittle manner.

The energy-based approach was motivated by the orders of magnitude discrepancy between the theoretical strength of glass and other brittle materials $\sigma_{theoretical} = \sqrt{(E\gamma_S/a_0)}$ and experimental data. E is the Young's modulus, γ_s is the energy required to break the atomic bonds per unit surface area created by the crack and a_0 is equilibrium distance between the atoms. Griffith suggested that the low fracture strength observed experimentally, as well as the variation in strength with sample size, was due to the presence of microscopic flaws in the bulk material.

$$\sigma_{failure} = \sqrt{\frac{G_C E}{\pi a}} \qquad (2.20)$$

Where $\sigma_{failure}$ is the stress required to cause failure, E is the Young's modulus and a is the crack length. The Griffith critical energy release rate, given by $G_C = 2\gamma_s$, was introduced.

In 1957, Irwin modified the approach to define the stress intensity factor K and critical stress intensity factor K_C, also known as the fracture toughness of the material, as shown in Equations (2.21) and (2.22) [72]. σ_∞ is the far-field stress value and Y is a geometrical parameter generally on the order of unity.

The relationship between K_C and G_C is shown in Equation (2.23). K can be considered as the crack-driving force and describes the severity of the stress state at a crack tip. A crack propagates when K exceeds K_C.

K_C is often replaced with K_{IC} as the first mode of loading and crack propagation is usually considered the dominant mode in ceramic testing. The three modes are: tensile opening (mode I), in-plane shearing (mode II) and out-of-plane shearing/tearing (mode III).

$$K = Y\sigma_\infty\sqrt{\pi a} \qquad (2.21)$$

$$K_C = Y\sigma_{failure}\sqrt{\pi a} \qquad (2.22)$$

$$K_C = \sqrt{G_C E} \qquad (2.23)$$

It is important to note that the fracture toughness K_{IC}, unlike strength, is a material property independent of the sample geometry and test technique.

2.5.3. Weibull statistics for fracture strength analysis

As shown in Figure 2.17, ceramics generally have wide strength scatter that are slightly skewed and measured strengths that are dependent on the sample volume, even for the same nominal composition and processing conditions. On the other hand, metals and polymers can normally undergo significant plastic deformation, which means cracks initiating from flaws become blunted, and therefore the effect of flaw size distribution is not as severe. This results in a narrower and more Gaussian-like strength scatter in ductile materials, as shown in the figure.

Diagrams showing the typical strength distribution of a metal and a ceramic, removed for copyright reasons.

Figure 2.17. (a) Typical mechanical strength distribution for a metal. (b) Typical mechanical strength distribution for a high-strength ceramic [73].

The strength measured for a ceramic sample can be understood using the weakest link concept, i.e. a chain is only as strong as its weakest link, and a long chain with more links is statistically more likely to possess a weak link than a shorter chain. In ceramics, the strength of a sample depends on the probability of finding a critical flaw and this probability increases with the size of the sample.

The Weibull distribution is often used to describe mathematically the strength variability of ceramics resulting from a given distribution of flaw sizes, as illustrated in Figure 2.18. The probability of failure at a given stress level is given by:

$$P_{failure}(\sigma, V) = 1 - P_{survival} = 1 - exp\left(-\left(\frac{\sigma}{\sigma_0}\right)^m \frac{V}{V_0}\right) \quad (2.24)$$

Where $P_{failure}$ is the probability a sample (or the fraction of a large group of samples), of effective volume V, fails under a stress σ. σ_0 is the characteristic strength, m is the Weibull modulus and V_0 is the volume scale parameter. σ_0 and m are parameters relating to the defect distribution in the material. The failure of brittle materials follows such strength distribution since only a small proportion of samples contain flaws large enough to cause failure at low applied σ. At intermediate σ, most samples fail as most defects are of intermediate sizes. Only a small number of samples containing solely very small flaws will survive up to very high σ.

The effect of varying the Weibull modulus on the observed strength scatter is illustrated in Figure 2.18. A high m value is clearly desirable for engineering applications as this implies high homogeneity, low variability and a reliable ceramic material that fails predictably.

Another important consequence of the Weibull distribution, which is supported by experimental observations, is Equation (2.25). This relationship allows the normalisation of strength measured for one effective test volume to a different test volume, e.g. converting flexural strength measured using the three-point bend test to flexural strength expected for the four-point bend test or converting tensile strength measured from a small specimen to that for an actual-size component.

$$\frac{\sigma_1}{\sigma_2} = \left(\frac{V_2}{V_1}\right)^{1/m} \quad (2.25)$$

(a)

(b)
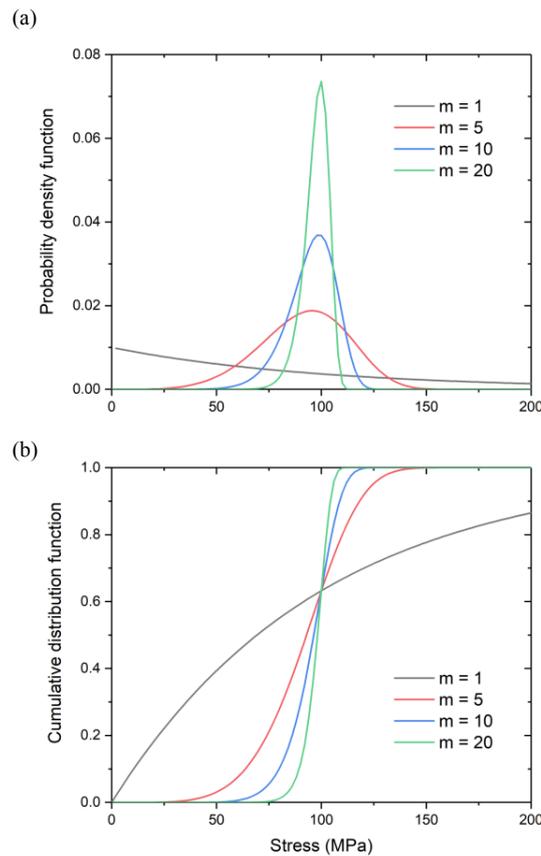
Figure 2.18. Cumulative failure probability of a brittle material as a function of applied tensile stress for increasing Weibull modulus *m*. The characteristic strength σ_0 has been set as 100 MPa.

2.5.4. Microstructure of (RE)BCO single grains

It is important to recognise that a (RE)BCO bulk superconductor is not a monolith, but rather a superconducting $REBa_2Cu_3O_{7-\delta}$ (RE-123) matrix made up of *ab*-direction and *c*-direction growth sectors that also contain pores, microcracks and non-superconducting RE_2BaCuO_5 (RE-211) inclusions, amongst other microstructural features and defects, throughout its volume. It is a composite material, and these microstructural features play a significant role in defining the superconducting and mechanical properties of the bulk superconductor. The various phases mentioned have been shown to demonstrate substantial variation as a function of position across a single grain and can sometimes vary significantly with distance from the seed crystal or proximity to the surface of the grown sample.

The cross section of a typical GdBCO bulk superconductor [74], 20 mm in diameter, is shown in Figure 2.19. The sample microstructure can be divided loosely into three regions. Region 1 contains a high density of pores, each approximately 50 μm in size. Large cracks are also visible. Region 2 displays significantly lower porosity and denser material, although small oxygenation cracks are visible. Region 3 covers the edge of the sample where growth has terminated. Gd-211 inclusions can be seen in the scanning electron microscope (SEM) image in Figure 2.19(b), where a Gd-211 free region is also visible in the microstructure, demonstrating inhomogeneity in the Gd-211 particle distribution. The concentration of Gd-211 particles also varies significantly on a more macroscopic scale (macro-segregation), i.e. over the length of the bulk sample, as a result of melt-processing.

Images of the cross section of a sample and of the Gd-211 particles dispersed throughout the Gd-123 matrix, removed for copyright reasons.

Figure 2.19. (a) Cross section of a GdBCO single grain, 20 mm in diameter, reported by Shi *et al.* [74], which can be divided loosely into three regions. (b) SEM image at 5000× magnification, showing Gd-211 particles (light) dispersed throughout the Gd-123 matrix (dark) and the presence of microscopic cracks.

2.5.5. Trapped fields > 17 T in bulk superconductor magnets

Considerable progress has been made over the years to improve on the maximum trapped field achievable in (RE)BCO bulk superconductors by developing new techniques to improve on the intrinsically poor mechanical properties of these materials, for example, by adding silver to the microstructure; or techniques to mechanically reinforce the samples after melt-processing, for example, by enclosing and compressing the samples with metallic rings.

To highlight the difficulties associated with surpassing the current trapped field record, there have only been two reports of trapped fields exceeding 17 T. In 2003, Tomita and Murakami demonstrated a trapped field of 17.24 T at 29 K in a pair of YBCO discs each 26.5 mm in diameter and 15 mm in thickness [7], as shown in Figure 2.20(a). The bulk samples were reinforced through firstly, resin impregnation, where epoxy resin was used to back-fill pores and microcracks in the samples to reduce the size of these defects and the corresponding stress concentration. The tensile strength of the bulk superconductors was shown to increase from 18 MPa to 77 MPa with resin impregnation alone. A small hole was also drilled into the centre of the trapped field magnets to allow for Bi-Pb-Sn-Cd alloy impregnation. Additionally, the samples were wrapped in carbon fibre fabric to compensate for the relatively high thermal contraction of the resin. The flat field profile towards the center of the sample arrangement at 29 K, as shown in Figure 2.20(a), suggests strongly partial magnetisation and that higher trapped fields could have been achieved with a larger applied field.

In 2014, Durrell *et al.* exceeded the field reported by Tomita and Murakami by demonstrating a trapped field of 17.6 T at 26 K in a pair of GdBCO/Ag discs each 24.15 mm in diameter and 13 mm in thickness [8], as shown in Figure 2.20. In this study, the bulk samples were instead reinforced with shrink-fit stainless-steel rings, each of which had an internal diameter of 24 mm to provide an interference fit and were fitted onto the samples at around 300 °C. Cooling to room temperature and subsequent cooling to cryogenic temperature generated a compressive pre-stress in the bulk superconductors since the steel rings contracted more rapidly than the samples themselves, which countered the tensile stresses that developed within the bulk samples as a result of the Lorentz force. The impact of metallic ring reinforcement on the mechanical properties of (RE)BCO bulk superconductors is illustrated in Figure 2.21.

Graphs showing the 17.2 T and 17.6 T record measurements, removed for copyright reasons.

Figure 2.20. (a) A trapped field of 17.24 T at 29 K reported by Tomita and Murakami [7]. The trapped field distribution at 46 K and 78 K are also shown. (b) A trapped field of 17.6 T at 26 K reported by Durrell *et al.* [8]. The field distribution after 160 minutes of flux creep and as the samples were warmed up at a rate of 0.5 K/min are shown. It can be seen that the trapped field was still above 10 T at 50 K.

Graph showing the calculated tensile stress in a bulk superconductor as a function of trapped field and the effect of adding an external steel ring, removed for copyright reasons.

Figure 2.21. Calculated maximum tensile stress in a bulk superconductor as a function of its trapped field [75]. A tensile strength between 20 MPa and 30 MPa has been assumed based on experimental results. The compressive pre-stress provided by the external steel ring and the corresponding increase in field attainable without the superconductor cracking are shown.

2.6.   Summary

This chapter has summarised the fundamental concepts regarding single-grain (RE)BCO bulk superconductors and highlighted the significance of their mechanical properties with respect to their trapped field performance and their suitability for practical applications.

Chapters 3 to 6 will present experimental studies carried out for this dissertation which were aimed at characterising and improving the mechanical properties of these technologically important materials.

Chapter 3

Flexural strength and indirect tensile strength of YBCO bulk superconductors

The mechanical properties of RE-Ba-Cu-O bulk superconductors are a key limiting factor to the application of these materials above trapped fields of around 8 – 10 T. Tensile stresses that develop in a magnetised bulk superconductor as a result of the Lorentz force can lead to fracture. Any resultant crack then forms a barrier to the flow of supercurrent, which causes an abrupt and irreversible drop in the field-trapping capacity of the sample. Therefore, the mechanical strength of bulk superconductors needs to be determined accurately to ensure the safe and reliable use of these quasi-permanent trapped field magnets in practical applications.

This chapter presents existing literature on the measurement of the mechanical properties of bulk Y-Ba-Cu-O discs, such as fracture strength and Young's modulus, will be presented. Small-scale investigations were then performed on single grains of Y-Ba-Cu-O at room temperature using three-point bend and Brazilian tests. The flexural strength measured at different locations across multiple 25 mm diameter Y-Ba-Cu-O discs allowed the spatial distribution of strength to be plotted, which was, in fact, not entirely random but exhibited a positional dependence as a result of the microstructure. The indirect tensile strength measured for a large batch of cylindrical, as-grown single grains was then used to indicate the bulk-to-bulk variation in sample strength, which was evaluated using the Weibull modulus.

YBCO was chosen for this study since this system has been investigated the most extensively over the past three decades and it is also the most readily available from commercial suppliers.

3.1. Background

3.1.1. Previous work on the mechanical characterisation of YBCO

The mechanical properties of Y-Ba-Cu-O (YBCO) bulk superconductors have been measured through mechanical and ultrasonic techniques prior to the melt processing of these materials and efforts have continued as single grains have become more readily available.

Young's modulus E values of 142 GPa and 165 GPa were recorded in a study of sintered YBCO with densities that were 87 % and 97 %, respectively, of the theoretical maximum density of YBCO [76], which is 6380 kg/m^3 as calculated from lattice parameter data. The theoretical E of a fully dense YBCO was then estimated to be around 180 GPa through extrapolation. The fracture toughness K_{IC} and flexural strength σ_f were also measured in the same study and reported to be 1.07 ± 0.18 MPa m$^{1/2}$ and 216.3 ± 16.4 MPa, respectively, at 80 % density. Alford $et\ al.$ discussed the wide spread in measured flexural strength, ranging from 80 MPa to 250 MPa [76], due potentially to the processing defects and to the strong strength–porosity dependence exhibited characteristically by brittle materials [77]:

$$\sigma = \sigma_0 e^{-bp} \qquad (3.1)$$

Where σ is the strength of a porous brittle polycrystalline body, σ_0 is the theoretical strength of a similar non-porous body, b is an empirical constant and p is the specimen porosity ($p =$ volume of voids/total volume of specimen).

The fracture strain of sintered YBCO was found to be less than 0.5 % as specimens break with little to no plastic deformation, and the ratio of tensile strength to compressive strength was observed to range from 1:17 to 1:12 [78], [79], which again are characteristic of brittle ceramics.

Anisotropy has been observed in the mechanical properties of textured, single-grain YBCO, as is the case with the superconducting properties of single grains, since characteristics along the ab-plane and c-axis have been found to differ considerably. For instance, Sakai $et\ al.$ reported average tensile strengths of 8.6 MPa along the c-axis and 23.7 MPa perpendicular to the c-axis of melt-grown YBCO [80], as a result of ab-plane cracks that form from thermal stresses at the RE-123/RE-211 interface during cooling. The tetragonal to orthorhombic phase transformation during oxygen annealing also contributes to the formation of these cracks.

Table 3.1 presents results from a number of relevant publications over the past three decades on measurements of the mechanical properties of YBCO single grains.

Table 3.1. Mechanical properties data (average values) for single-grain YBCO (unless stated otherwise) available in the existing literature.

Fracture strength σ (MPa) (values quoted are flexural strengths σ_f unless stated otherwise)	Young's modulus E (GPa)	Comments	Reference(s)
	182 ($\|ab$) 143 ($\|c$) 213 (measured on Y-211 particles only)	Young's modulus was measured at 300 K using a nano indenter, which moves a diamond indenter into the surface of the sample with a precisely controlled load while continuously monitoring the displacement. Elastic and thermal mismatch between the Y-123 and Y-211 phases suggests the rigid Y-211 particles enhance the fracture resistance of the matrix by energy dissipation through interfacial delamination and crack bridging.	Goyal *et al.* 1991 [81], [82]
		Fracture toughness was determined using the indentation fracture method with a Vickers indenter, resulting in $K_{IC} = 0.9 – 1.2$ MPa m$^{1/2}$ being measured without Y-211 particles, and $1.6 – 2.1$ MPa m$^{1/2}$ with Y-211 particles. The toughening of the Y-123 matrix was attributed to crack deflection, decohesion at the Y-123/Y-211 interface and crack bowing.	Fujimoto *et al.* 1992 [83]

		K_{IC} of samples that had not been cooled to cryogenic temperatures was found to be 1.5 – 2.0 MPa m$^{1/2}$ and the range was attributed to intrinsic microstructural variation. A 20 % decrease in K_{IC}, which gives the threshold for fracture, was observed after 50 thermal cycles, concluding that thermal cycling was partly responsible for the generation and enlargement of microcracks to a flaw size sufficient to act as nucleation sites.	Leenders *et al.* 1997 [84]
77.3 ± 8.3 (before flux avalanche) 55.7 ± 19.6 (after flux avalanche)	128 ± 11 (before flux avalanche) 100 ± 6 (after flux avalanche)	Properties along the *ab* direction were measured using the three-point bend test. Discs were subjected to flux avalanche with a 6.5 T applied field at 15 K and compared to pre-avalanche discs, showing a degradation of mechanical properties and an increase in microcracks as a result of the flux jumps. Annealing was also shown to increase the flaw population.	Yu *et al.* 1997 [11]
23.7 (tensile test ‖*ab*) 8.6 (tensile test ‖*c*) 13.4 (tensile test on SmBCO ‖*ab*)		Uniaxial tensile tests were conducted on cubic specimens cut from bulk YBCO and SmBCO. Each side of the cubes was 5 mm in length. Cracks formed from the thermal stress during thermal cycles and stress due to the tetragonal to orthorhombic phase transition.	Sakai *et al.* 2000 [80]
56.1 (without resin 293 K) 84.6 (without resin 77 K) 115.1 (with resin 77 K)		Commercial 46 mm YBCO samples from Nippon Steel were tested using the three-point bend test to determine the effects of resin impregnation. Weibull analysis revealed Weibull coefficients $m = 3.27$ and 5.62 at 293 K and 77 K, respectively, for YBCO before impregnation. m was increased to 16.03 and 12.56 at 293 K and 77 K, respectively, after impregnation.	Tomita *et al.* 2002 [85]

91 ± 19 (0 wt% Ag)		Three-point bend tests were performed at 77 K on 45 mm YBCO bulk superconductors containing different amounts of silver. The Weibull coefficient was 5.8 for the Ag-free specimens.	Fujimoto 2003 [86]
109 ± 34 (10 wt% Ag)			
134 ± 28 (20 wt% Ag)			
56 (tensile)	118 (tensile)	YBCO single grains with 15 wt% Ag were evaluated using tensile and bend tests. E and σ were found to be significantly higher for the bend test as a result of the smaller effective test volume. K_{IC} was also determined using notched specimens, and results from the two test techniques coincided at 1.9 MPa m$^{1/2}$.	Okudera *et al.* 2003 [87]
104 (bending)	136 (bending)		
39 (tensile)	122 (tensile)	Comparison of tensile and bend test results on YBCO samples at room temperature. Weibull coefficient was determined for each group, and the coefficient for the bending strength, 17.6, was significantly higher than that of the tensile strength, 6.8.	Katagiri *et al.* 2004 [88]
74 (bending)	132 (bending)		
74 (300 K)	132 (300 K)	Three-point bend tests were performed on 4 mm × 3 mm × 36 mm specimens cut from a large bulk superconductor at room temperature and at 77 K. E was slightly lower and σ_f was slightly higher in the top region of the sample than at the bottom of the sample.	Murakami *et al.* 2004 [89]
90 (77 K)	148 (77 K)		
73 (5 mol% Dy-211)		Three-point bend tests were performed on DyBCO/Ag samples with increasing molar percentage (mol%) of Dy-211. Microstructural analysis showed the number of cracks in the *ab* plane	Nariki *et al.* 2004 [90]
95 (40 mol% Dy-211)			

		decreased with increasing Dy-211 content.	
$\sigma_f = 104e^{-0.012p}$	$E = 156e^{-0.016p}$	Four-point bend tests were performed on GdBCO/Ag at 77 K, and the bending properties were correlated to the local porosity.	Fujimoto and Murakami 2012 [91]
53.6 (bending at 300 K) 71.4 (bending at 77 K) 31 ± 3 (cylinder splitting at 77 K)	94 ± 7 (bending at 300 K) 157 ± 13 (bending at 77 K)	Evaluation of the strength, toughness and hardness of 25 mm diameter TSMG YBCO single grains at 77 K and 300 K. Cylinder splitting tests (also known as the Brazilian test) were carried out on whole cylindrical samples.	Konstantopoulou *et al.* 2014 [92]

It is clear from the studies in Table 3.1 that a number of factors affect the mechanical properties of single grains, including porosity, RE-211 concentration and micro-crack density. Several studies have also explored the spatial distribution of fracture strength and Young's modulus within large (RE)BCO single grains [7], [89], [93]–[95]. However, these studies were often not sufficiently comprehensive, utilised Ag-doped samples (the ductile Ag phase introduces another variable to the microstructure and to the mechanical properties), or the causes of the distribution were not investigated in detail. A number of qualitative observations were made in these investigations, such as the increased strength of sub-specimens taken from the upper surface of the single grain compared to the weaker, higher porosity sub-specimens taken from the centre of the single grain [96], [97].

3.1.2. Motivation for the proposed study

A wide range of values have been measured and reported, as shown in Table 3.1, in terms of the mechanical properties of YBCO single-grain bulk superconductors, including in σ_f, E and K_{IC}. This could be attributed to the exact melt processing procedures differing from study to study, which culminates in differences in the microstructure of the samples such as the overall porosity, Y-211 particle size, Y-211 particle distribution and micro-crack density. In addition, the characterisation techniques and specimen dimensions may also differ, and a consequence of Weibull statistics is that a larger effective test volume would result in a lower apparent strength, even for the same material with the same defect distribution.

Although several studies have acknowledged a wide scatter of strength amongst specimens extracted from the same sample or same (RE)BCO system, it is not clear whether the scatter was entirely random or has a positional dependence, potentially from a variation in the local defects with position. In addition, there are very few reports on the variation of tensile strength of individual, as-grown bulk superconductors across a large batch of samples processed nominally under the same conditions, which may be the information most relevant to designing practical applications.

In order to investigate the above, small-scale mechanical tests were performed on single-grain YBCO bulk superconductors at room temperature. Three-point bend tests were performed on long beams cut from large, fully-grown bulk samples, allowing the flexural strength at multiple locations within a single-grain sample to be determined. Brazilian tests were subsequently performed on whole as-grown and as-annealed bulk superconductors to determine indirectly the tensile strength of individual samples, allowing the bulk-to-bulk variation to be quantified. In both cases, sample strength in the *ab*-direction was measured, since the Lorentz force produces hoop and radial stresses that are parallel to the *ab* planes.

YBCO was chosen for this study since a large number of experimental studies have been performed on this material due to the relatively widespread availability of well-established techniques to grow YBCO single grains. Furthermore, YBCO is also the most readily available system from commercial suppliers. Although this study focuses only on YBCO, the results acquired are expected to be applicable more generally to the other (RE)BCO systems since all systems display common microstructural defects, such as porosity and RE-211 inhomogeneities, which will be covered later in the chapter.

3.2. Experimental details

3.2.1. Fabrication of YBCO single grains

Two sizes of singe-grain YBCO were fabricated via top seeded melt growth (TSMG) in air in a conventional box furnace from: (75 wt% $YBa_2Cu_3O_7$ + 25 wt% Y_2BaCuO_5) + 0.5 wt% CeO_2 precursor powder. Bulk YBCO samples approximately 26 mm in diameter and 10 mm in thickness post-growth were prepared for the three-point bend test and YBCO samples approximately 16 mm in diameter and 6 mm in thickness for the Brazilian test. For reference, YBCO single grains of diameter 16 mm, as shown in Figure 3.1, were obtained by subjecting the precursor pellets to the TSMG heat profile shown in Figure 3.2. Two additional 26 mm diameter YBCO samples were fabricated via top seeded infiltration and growth (TSIG) [98]–[100], an increasingly popular technique to generate dense, uniform bulk samples with less shrinkage during growth. The fully-grown TSMG and TSIG bulk superconductors were annealed in flowing oxygen at $420 - 450\,°C$ for ~ 7 days to facilitate the tetragonal (non-superconducting) to orthorhombic (superconducting) phase transition of the Y-123 phase.

A larger diameter was chosen for the three-point bend test to maximise the number of beams that can be extracted from each sample grown. On the other hand, since the Brazilian test is performed on whole disc samples, a smaller diameter was chosen to minimise material cost and sample processing time.

To check the superconducting properties of the samples and confirm they are indeed single grains, the top and bottom surfaces were polished flat using SiC paper (up to 1000 grit) for trapped field measurements. Each sample was then magnetised at 77 K by field-cooling with an external applied field of 1.2 T in LN_2 before the peak trapped field on the top surface was measured using a hand-held axial gaussmeter (Hirst Magnetic Instruments). The field profile was also mapped using a rotating linear array of 20 Hall sensors (Lakeshore HGT-2101). A typical field scan displayed a conical profile with a high peak field, which confirmed that the sample comprised of a single grain.
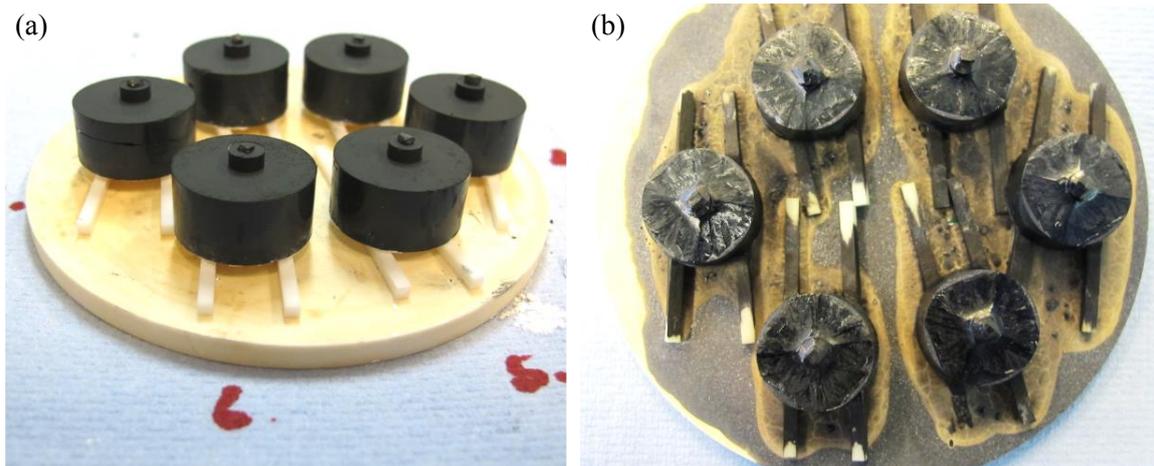
Figure 3.1. (a) A batch of pressed precursor pellets, along with NdBCO seed crystals and buffer pellets, ready for TSMG processing in a box furnace. (b) Resultant fully-grown YBCO single grains after TSMG. The four-fold growth facet lines in the *ab*-plane, which are characteristic of single grain growth, can be seen in the top surfaces of the samples.
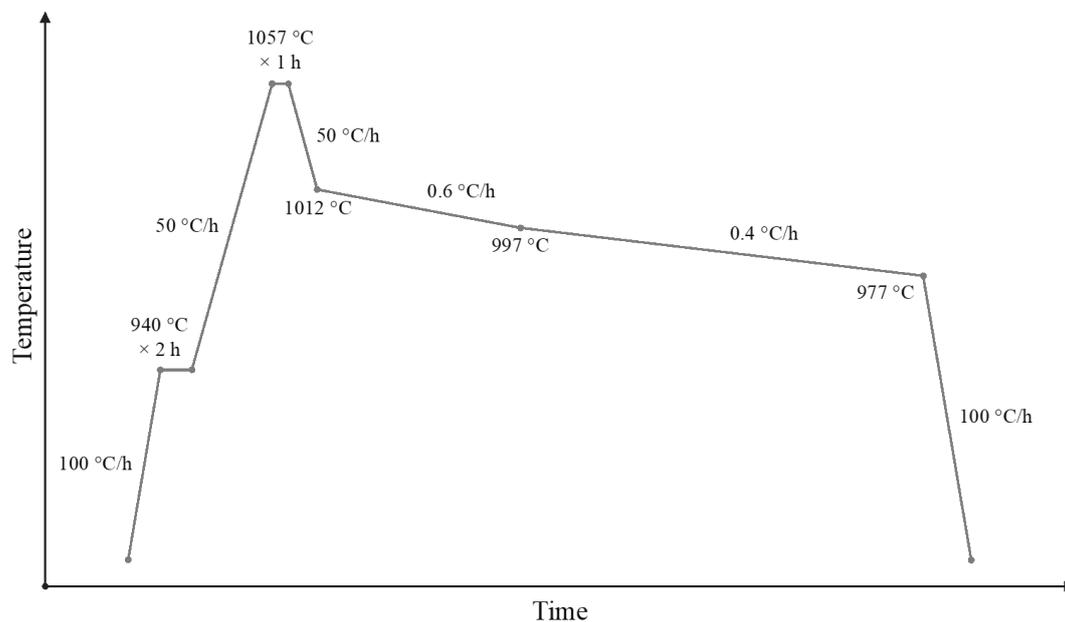
Figure 3.2. Thermal profile used to grow the 16 mm diameter YBCO characterised in this study. The temperatures indicated are target temperatures. Most furnaces contain a small temperature offset to the temperature displayed on the controller, which was measured and taken into account when deriving the temperature profile. A full heating cycle takes approximately 100 hours to complete.

3.2.2. Mechanical testing I – the three-point bend test

The three-point bend test is a traditional method in engineering mechanics and is used to determine the behaviour of various types of material when subject to simple beam loading. The elastic modulus in bending, stress-strain characteristic, flexural strength and fracture toughness (if samples are pre-notched) can all be obtained using this technique.

In a three-point bend test, an external load is applied to the mid-point of a long beam of specimen while each end is supported on a point of contact, as shown in Figure 3.3, thereby placing the convex side of the specimen in tension and the concave side in compression. The bend test is commonly used on polymers, ceramics and composites due to the ease of specimen preparation and testing. In addition, specimens do not need to be gripped or clamped, like in direct tensile tests, which can lead to a severe stress concentration in brittle materials.

In the three-point bend test, the flexural stress σ at the mid-point of the side under tension is given by:

$$\sigma_{flexural} = \frac{3Fl}{2bd^2} \tag{3.2}$$

Where F is the load required to achieve a given deflection, l is the span length, b is the width of the specimen and d is the depth/thickness of the specimen. The flexural strength of a specimen can be calculated by testing it to failure.

The flexural modulus E_f can be calculated from the slope s of the force–deflection curve:

$$E_{flexural} = \frac{sl^3}{4bd^3} \tag{3.3}$$

$$s = \frac{\Delta F}{\Delta z} \tag{3.4}$$

Where Δz is the displacement of the centre of the test beam in the direction of the applied load.
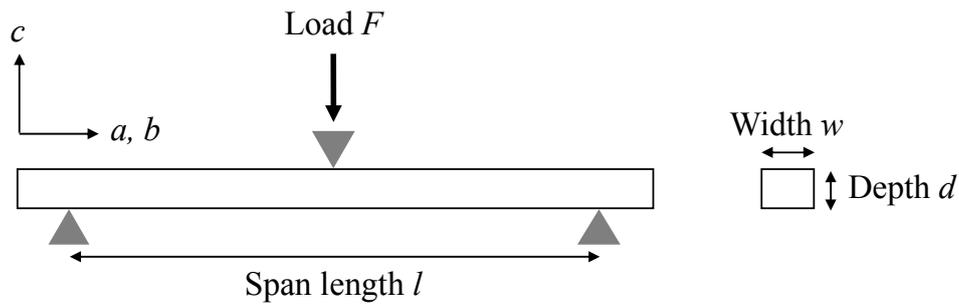
Figure 3.3. Schematic illustration of the three-point bend test on beams cut from (RE)BCO bulk superconductors. The crystallographic directions of the (RE)BCO sample are also shown.

Rectangular bar specimens approximately 2 mm in width, 1.5 mm in thickness and at least 20 mm in length were cut from the 26 mm diameter YBCO single grains using a diamond cut-off wheel (Struers). Cuts were first made parallel to the c-axis, to produce vertical slabs, and then subsequently along the ab-axes, to produce beams. The cuts were carried out in this order such that any tilt in the crystallographic planes could be seen, and compensated for, after the initial cut. The positions of the bars in the parent bulk superconductor and their identifying labels are shown in Figure 3.4. The bars were cleaned in warm acetone to remove any remaining wax in the pores or on the specimen surface and subsequently polished using 2400 Grit SiC paper to eliminate any surface defects introduced during the cutting process.

To determine the flexural strength, each beam was loaded in an electro-mechanical tensile testing machine (Instron) with a 100 N load cell at a crosshead speed of 0.12 mm/min until failure. The beams were positioned such that the load was applied along the c-axis and the tensile stress produced was along the ab planes, as shown in Figure 3.3.

In general, a beam can be subjected to three- or four-point bending. In the three-point bend test, a small effective volume under the central pin is under peak stress. On the other hand, the entire volume between the two central pins is under uniform stress in four-point bending. According to Weibull statistics, the larger effective test volume in four-point bending would generate strength values more representative of the material. However, the three-point bend test was chosen for our study due to ease of comparison to literature and ease of rig and sample alignment along the horizontal plane. The current study certainly could be extended to four-point bending for completeness.
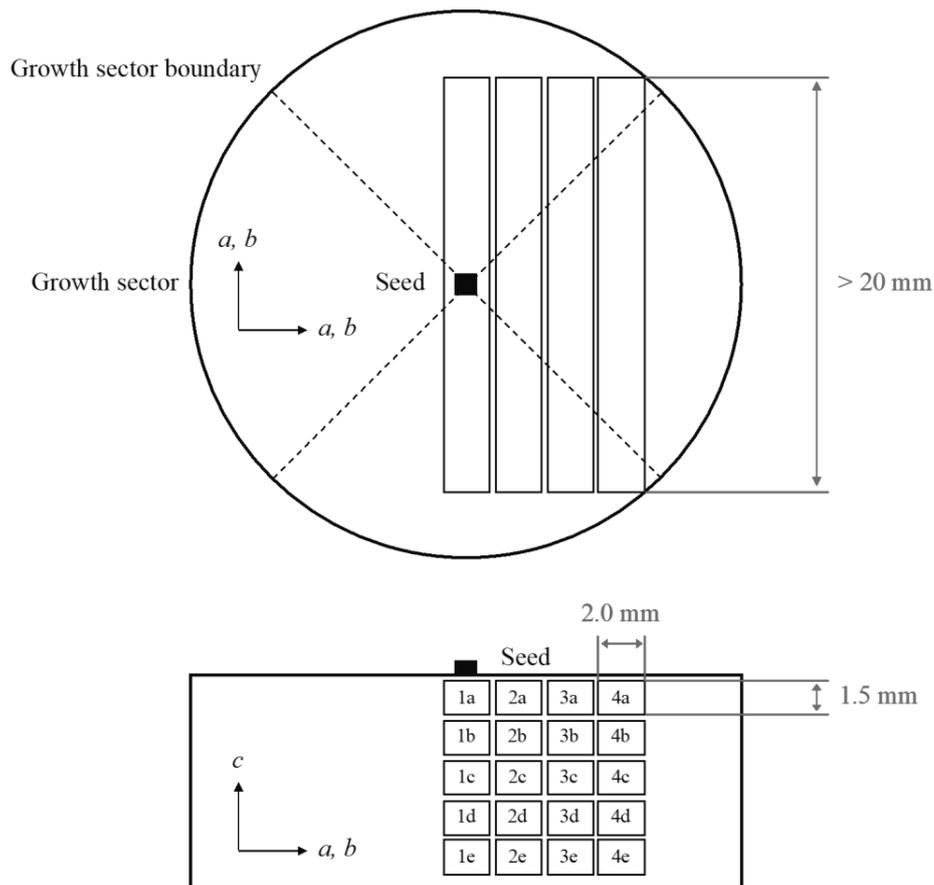
Figure 3.4. Schematic illustration of beams cut from a large, single-grain bulk superconductor for the three-point bend test. The location and label of each sub-specimen is shown in the bottom half of the figure.

3.2.3.   Mechanical testing II – the Brazilian test

The Brazilian test, first proposed by Carneiro in 1943 [101] and given a complete 2D stress solution by Hondros in 1959 [102], is an indirect tensile testing technique used to determine the tensile strength of brittle materials such as concrete, rocks and ceramics. A cylindrical specimen is loaded under compression by two opposing platens, with the compression inducing perpendicular tensile stress that is almost constant across the centre of the cylinder, until the specimen cracks, as shown in Figure 3.5.

Tensile strength of a cylindrical specimen determined through the Brazilian test is given by:

$$\sigma_{indirect} = \frac{2P}{\pi Dt} \qquad\qquad (3.5)$$

Where P is the load at failure, and D and t are the diameter and thickness of the cylinder, respectively.

The stress evaluation is based on a number of assumptions [103], [104], including firstly, that the load is applied uniformly over a small arc angle between 9 and 14 °; secondly, the frictional tangential stresses at the specimen–platen contacts can be neglected; thirdly, the material failure follows the Griffith criterion, i.e. a crack will propagate under constant stress if the increase in surface energy due to increasing crack length is compensated by a decrease in elastic strain energy; fourthly, the specimen is taken to be homogeneous, isotropic and linearly elastic prior to brittle failure. The validity of the test is also based on the practical observation that most brittle materials in a biaxial stress field fail in tension at their tensile strength rather than in compression due to the high ratio of compressive strength to tensile strength.

The Brazilian test can be a suitable technique for characterising (RE)BCO single grains since the common cylindrical geometry of bulk superconductors lends itself well to the test technique and therefore minimal machining is required. This means, firstly, that there are fewer opportunities to introduce defects that can affect the mechanical test results, and, secondly, the strength of whole/individual bulk samples can be determined.

The 16 mm diameter YBCO bulk samples used in the Brazilian tests were grown in three batches from the same precursor powder and with the same heating profile to assess reproducibility. These were prepared for mechanical testing by polishing their circumferential surfaces on a lathe to remove any irregularities. The top and bottom surfaces were also polished to ensure they were flat and parallel.

The polished samples were compressed along the a-growth sectors under aligned steel loading platens in an Instron machine with a 100 kN load cell at a crosshead speed of 0.01 mm/min until a hairline crack formed along the direction of the compressive load, as shown in Figure 3.5.

(a)

Load *P*

a, b

a, b

Diameter *D*

a, b

c

Thickness *t*
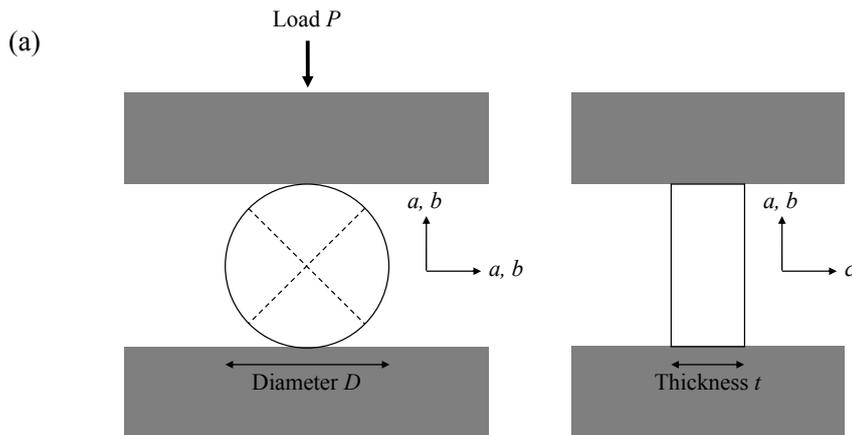
Diagram showing the magnitude of the principal stresses in a Brazilian test disc removed for copyright reasons.

Figure 3.5. (a) Schematic illustration of the Brazilian test on as-grown (RE)BCO single grains. (b) Principal stresses, which are normalised by $2P/\pi Dt$, determined numerically and using Hondros' solution, along the centre of a compressed Brazilian disc [104].

3.2.4. Microstructural analysis

The growth of single grains is axially symmetric and proceeds from the seed which is placed at the centre of the upper surface of the pressed precursor pellet. As a result, axial symmetry has been assumed when analysing the microstructure of the as-grown YBCO samples. For the three-point bend tests, half of each bulk superconductor was cut into bar specimens while the other half was retained for imaging using an optical microscope (Nikon Eclipse ME600 optical microscope with a Moticam Pro 282A CCD camera). The cross section of the bulk sample was polished using progressively finer SiC paper and finished with a diamond paste ≤ 1 µm in particle size, until a mirror finish was achieved, to obtain high-quality optical images.

Optical micrographs under low and high magnification were taken at radial and axial positions that correspond to the mid-point of each flexure beam, such that the porosity and Y-211 content at each location with mechanical strength data could be estimated. The images were evaluated using ImageJ image processing software following the instructions provided by the National Institutes of Health, the supplier of ImageJ. The micrographs were inserted into the software, converted into *8-bit* images, then made *binary*, before being analysed using the *analyse particles* function [105], which determined the percentage area coverage of the microstructural feature of interest. Examples of optical micrographs showing the presence of pores and Y-211 particles embedded in the Y-123 matrix are shown in Figures 3.6 and 3.7. The typical size of these features can be deduced from the micrographs.

The resolution of the camera at 50× magnification was 0.670 µm/pixel, and 0.0667 µm/pixel at 500× magnification, both of which were significantly smaller than the smallest feature size anticipated in the bulk microstructure, implying sufficient resolution for this investigation.
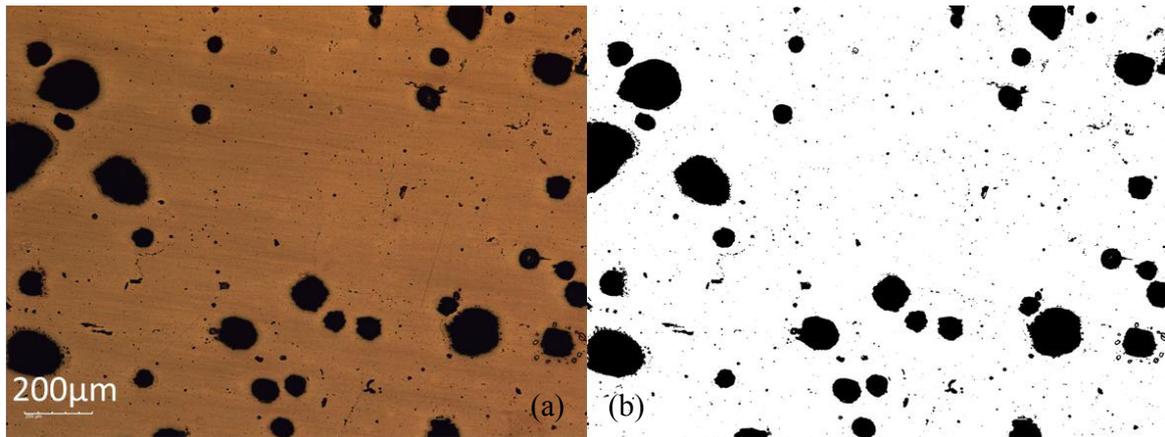
Figure 3.6. (a) Example of an optical micrograph of the cross section of an YBCO bulk superconductor under 50× magnification, displaying a range of pores and voids that formed during the growth process. (b) Optical micrograph converted into a binary image for ImageJ processing, showing in black the pixels that are counted as pores.
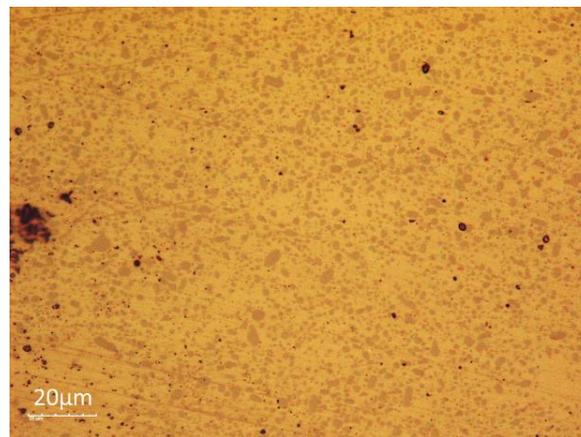
Figure 3.7. Example of an optical micrograph of the cross section of an YBCO bulk superconductor under 500× magnification, displaying the fine, micron-scale Y-211 particle inclusions (dark) embedded in the Y-123 matrix (light).

3.3. Results and discussion

3.3.1. Spatial distribution of flexural strength within YBCO

Figure 3.8 shows the typical load-displacement curves measured on YBCO single grains using the three-point bend and Brazilian tests, where load was applied at a constant crosshead speed for each test technique. Three slightly different responses are shown in Figure 3.8(a). Curve 1 represents the brittle failure of most YBCO beams under bending, as the material response is linearly elastic prior to sudden and complete fracture at the peak load as a result of a macroscopic crack forming rapidly across the specimen.

However, quasi-brittle failure was also observed in some of the specimens, as illustrated by curves 2 and 3. Quasi-brittle behaviour can be observed in certain concrete, fibre reinforced concrete, toughened ceramics and composites. This type of failure involves a gradual degradation of the material near the peak load, leading eventually to an abrupt, catastrophic failure. The degradation is a consequence of the slow, stable growth of defects in the specimen, such as microcracks and voids. The latter load-displacement curves suggest quasi-brittle behaviour since they displayed noticeable non-linear regions and stiffness reduction at their peaks. Strain softening was subsequently observed past the peak stress, which is indicative of stable crack growth, before complete fracture.

This behaviour is likely observed in the specimens since (RE)BCO single-grain bulk superconductors are heterogeneous materials and different types of toughening mechanisms exist in the material to shield crack growth. Most notably, the dispersed RE-211 inclusions, as a secondary phase, help to bridge and deflect cracks that initiate in the RE-123 matrix, providing additional energy absorption at the crack front and enhancing fracture toughness as crack length increases. This is analogous to the role of fibres in fibre-reinforced concrete and ceramics.

The stable crack growth with each magnetisation cycle, i.e. loading cycle, could also explain the gradual degradation of the mechanical properties, including strength and stiffness, and the trapped field performance of (RE)BCO single grains in practice, as discussed by Yu *et al.* [11]

Figure 3.8(b) shows the typical load-displacement curve for a single-grain YBCO disc under Brazilian testing, again illustrating brittle fracture.

(a)

(b)
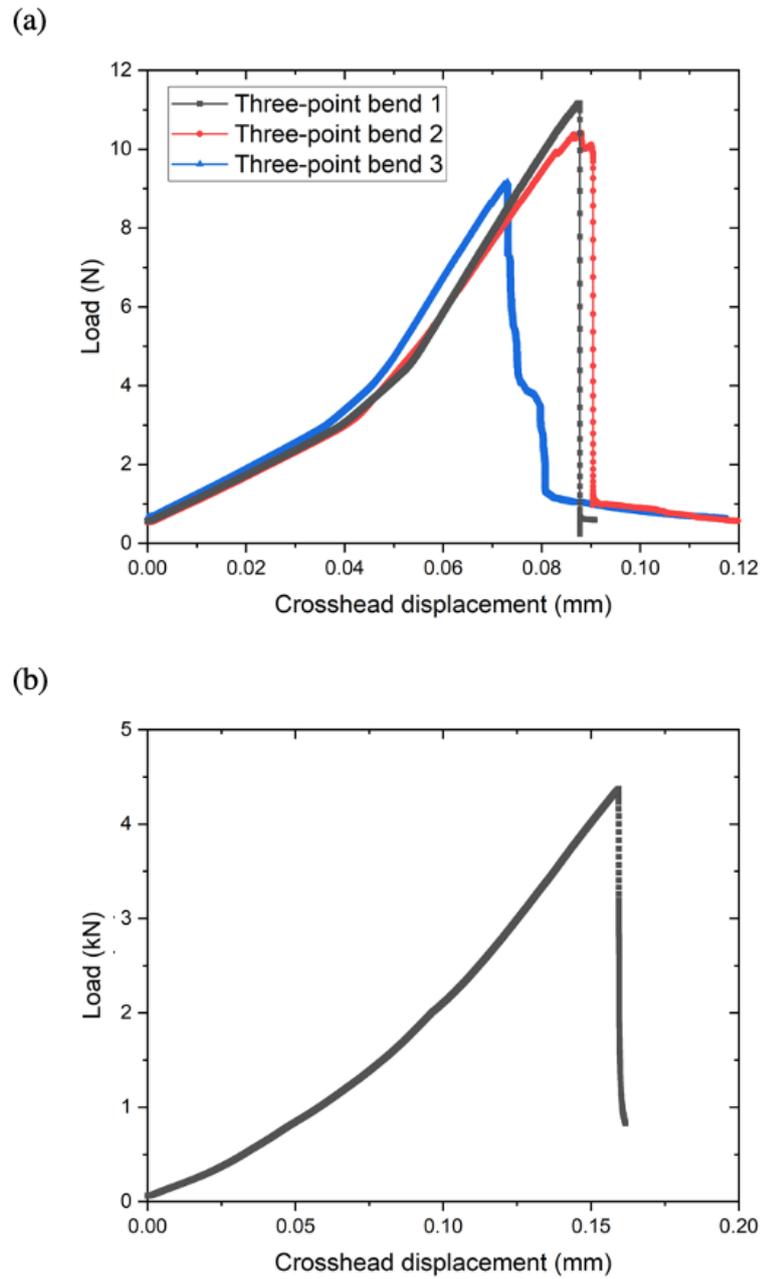
Figure 3.8. (a) Typical load-displacement curves measured on a YBCO flexure beam using the three-point bend test. (b) Typical load-displacement curve measured on a cylindrical disc of single-grain YBCO using the Brazilian test.

Figure 3.9 shows the spatial distribution of flexural strength σ_f across four YBCO bulk superconductors of approximately 26 mm in diameter, two of which were grown by top seeded melt growth (TSMG) and two by top seeded infiltration and growth (TSIG). The samples were produced by Dr Yunhua Shi and Dr Devendra Namburi.

It is apparent from these data that the strength measured at a given position in a bulk sample is not entirely random but that there is, firstly, a general increase in σ_f with distance from the seed, particularly in the *ab* direction; and, secondly, a low strength region at the centre of the YBCO samples. The average value measured for all beams was 49.3 ± 12.7 MPa (one standard deviation), and the cause of the relatively large spread was further investigated. Weibull analysis revealed a Weibull modulus of 4.5 in terms of the strength distribution, which is consistent with existing literature shown in Table 3.1.

The variation of the microstructure across a typical YBCO bulk sample was examined in order to explain the positional dependence of fracture strength shown in Figure 3.9. The results of the ImageJ analysis are shown in Figure 3.10, where the porosity and Y-211 content can be seen to vary significantly with distance from the seed in both growth directions. These variations are also illustrated schematically in Figure 3.10(c) and (d). Optical micrographs taken from the cross section of the representative YBCO sample are shown in Figure 3.11 and Figure 3.12 to illustrate the microstructural variation along the *ab* and *c* directions.

Firstly, high porosity is generally observed at the centre of a bulk superconductor and reduces gradually towards the surface with a thin pore-free region at the surface, which is consistent with reports in the literature [106], [107]. This is due to the evolution of oxygen gas during the peritectic reaction which becomes trapped in the viscous melt in the partially molten state. Gas bubbles produced near the surface have a shorter diffusion path and hence are more likely to escape into the atmosphere. On the other hand, gas bubbles at the centre cannot escape so they tend to coalesce into large visible voids.

(a)

(b)
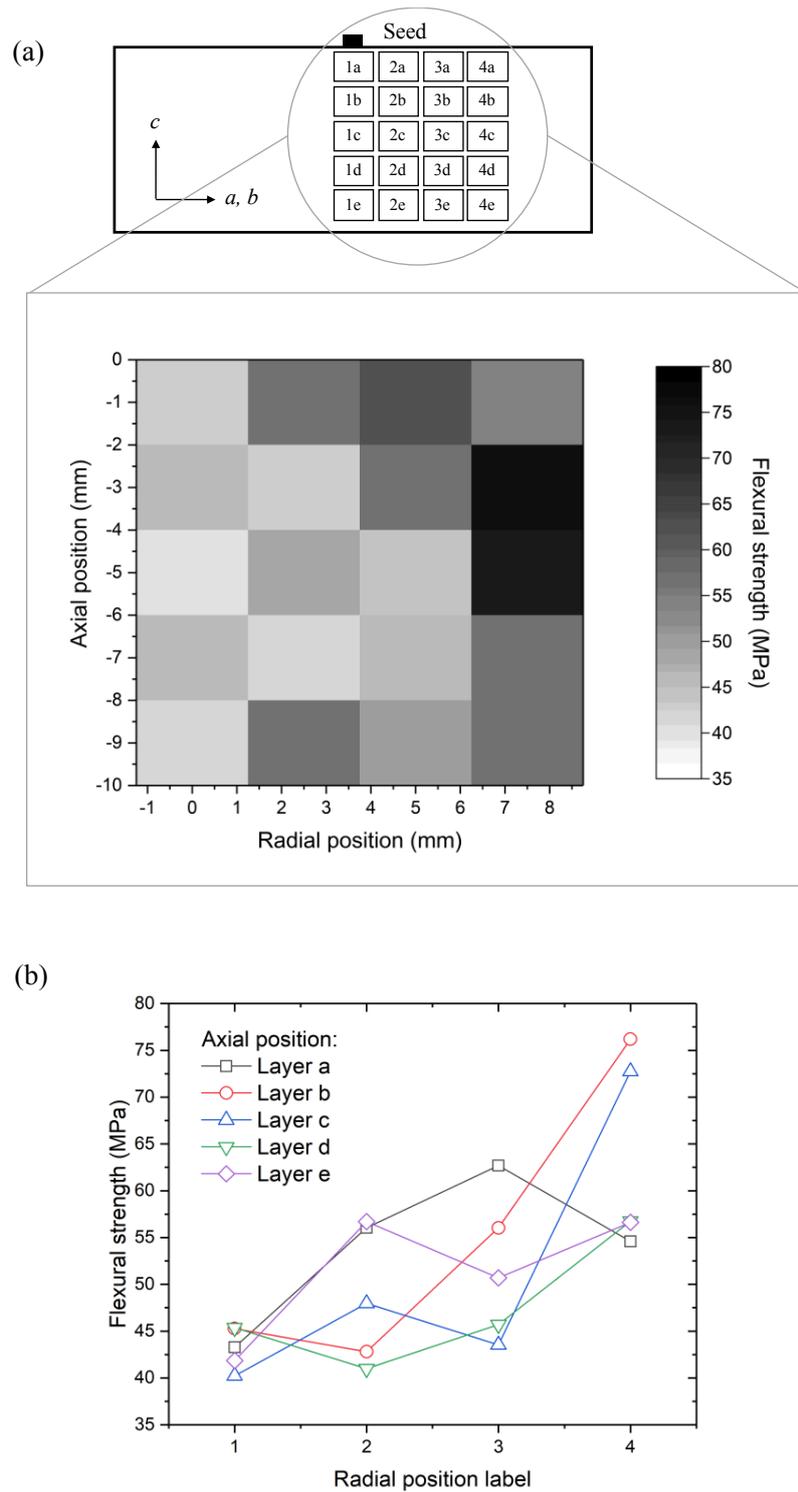
Figure 3.9. Spatial distribution of flexural strength, as (a) a greyscale intensity plot and as (b) a line plot, averaged across four 26 mm diameter YBCO single grains fabricated under slightly different conditions.

(a)

(b)

(c)

Porosity variation

(d)

RE-211 content variation
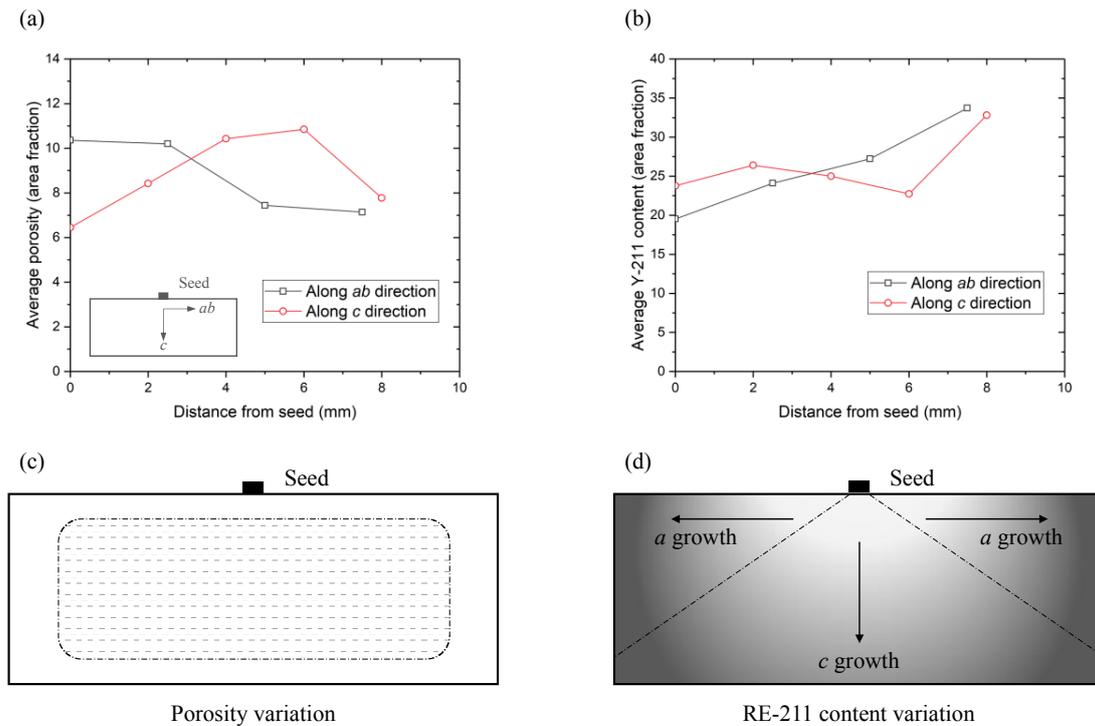
Figure 3.10. (a) Porosity and (b) Y-211 content measured across a 26 mm diameter TSMG YBCO sample as a function of distance from the seed crystal, along the two principal growth directions. Illustrations of the systemic variations in (c) porosity and (d) Y-211 content with position as a result of the seeded melt growth process. Darker regions represent higher porosity and concentration of Y-211 particles. The RE-211 content is often slightly higher in the *a*-growth sectors than the *c*-growth sector due to the different entrapment critical radii *r** for the *ab* and *c* growth directions at the same level of undercooling.

Secondly, significant macro-segregation of RE-211 particles is evident as the RE-211 volume fraction is generally observed to increase with distance from the seed, which is explained partially by the particle push–trap theory describing whether foreign, inactive particles are pushed or trapped by an advancing solid–liquid interface [108], [109], i.e. the growth front, during solidification. The theory considers the two dominant forces, namely the drag force due to viscous flow around the particle and the force due to the interfacial energy $\Delta\sigma_0$, acting on a particle during solidification. The theory dictates the probability that particles of a certain size become trapped by a growth front moving at a rate of R in a melt with viscosity η. Particles smaller than the critical radius *r**, which can be determined from R and η using Equation (3.6), will be pushed by the growth front whereas particles larger than *r** will be trapped.

$$R \propto \frac{\Delta\sigma_0}{\eta r^*} \qquad (3.6)$$

At the beginning of the growth process, the undercooling ΔT and growth rate R are relatively low so only large particles become trapped by the growth front, giving a low concentration of RE-211 particles in the vicinity of the seed. As the growth front extends further away from the seed, ΔT and R increase, causing the large quantity of smaller particles to become trapped in the single grain as well. As a result, there is generally an increase in RE-211 volume fraction and a decrease in the average particle size with distance from the seed, as observed experimentally in Figure 3.10. This is also shown in Figure 3.12, where it is clear the Y-211 volume fraction has increased significantly with distance from the seed.

However, it is important to note the conventional particle push–trap theory does not fully explain the distribution of RE-211 particles in a (RE)BCO bulk superconductor since the RE-211 particles are not entirely inactive; but are expected to become smaller when being pushed by the growth front due to self-decomposition and/or become larger due to Ostwald ripening.

By plotting the flexural strength measured at each position against the local porosity and Y-211 content, as shown in Figure 3.13, the spatial distribution of strength that was shown in Figure 3.9 can be understood. In order to distinguish the effects of porosity and Y-211 inclusions, the strength data in Figure 3.13 were binned and averaged at 2.5 % and 5 % intervals for the porosity and Y-211 content, respectively. The binned averages are represented by red diamonds in the figures. The averaging was carried out because, at any given porosity, Y-211 content may not be a fixed variable, and vice versa. Best fit lines have also been added to illustrate the general trends.

The strength can be seen to decrease with increasing porosity, due to the stress concentration introduced by voids within the material, which initiates cracks and also lowers the Young's modulus. On the other hand, strength increases with increasing Y-211 content due to enhancement of the fracture toughness by the high-modulus Y-211 inclusions through energy dissipation by interfacial delamination and crack bridging. These two driving factors, combined with the reproducible microstructural inhomogeneities in melt-grown YBCO and (RE)BCO bulk superconductors, are responsible for the spatial distribution observed in Figure 3.9.
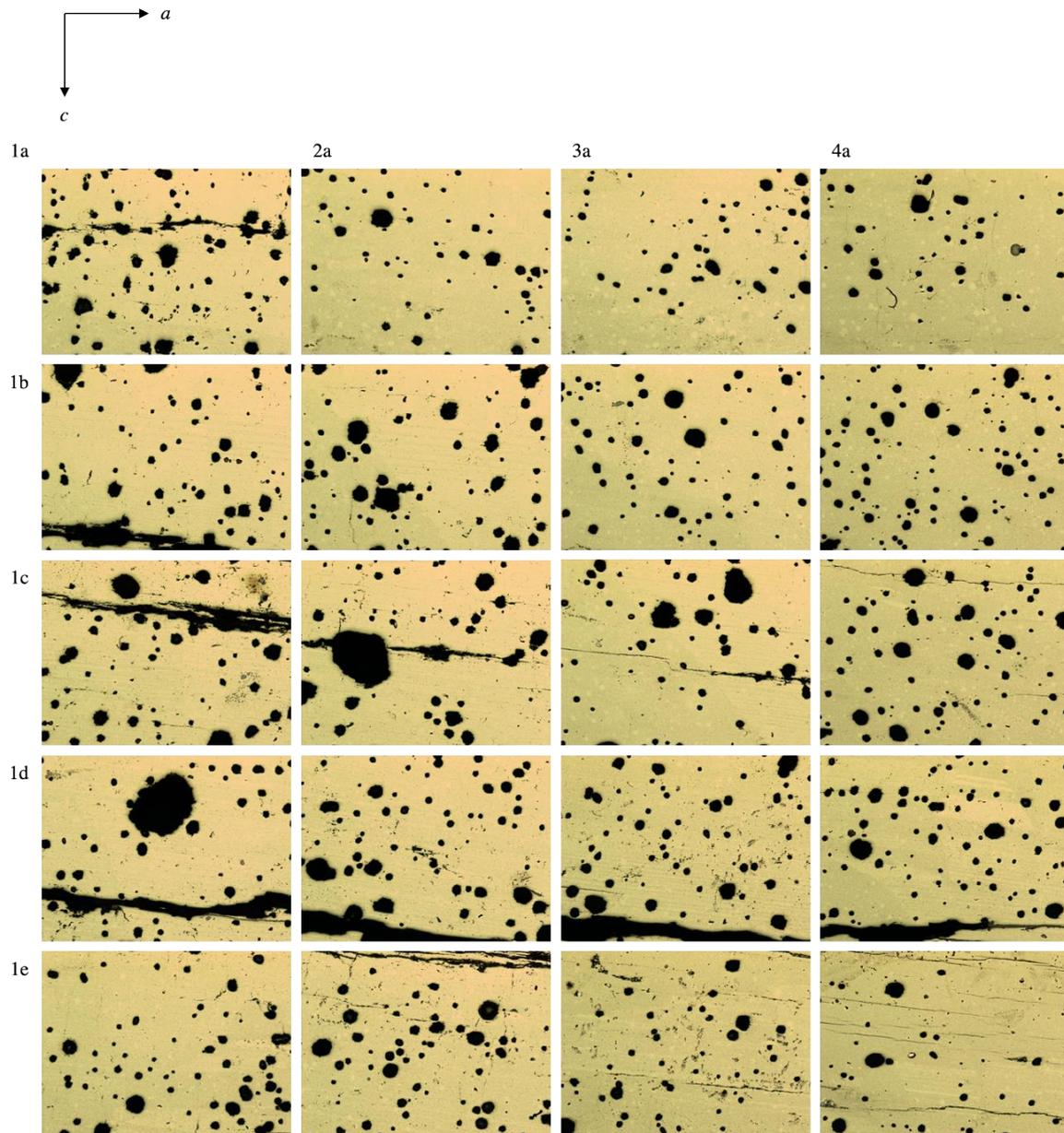
Figure 3.11. Optical micrographs taken at 50× magnification of the porosity in a typical 26 mm diameter YBCO single grain along the *ab* and *c* directions. The labels correspond to those presented in Figure 3.4.
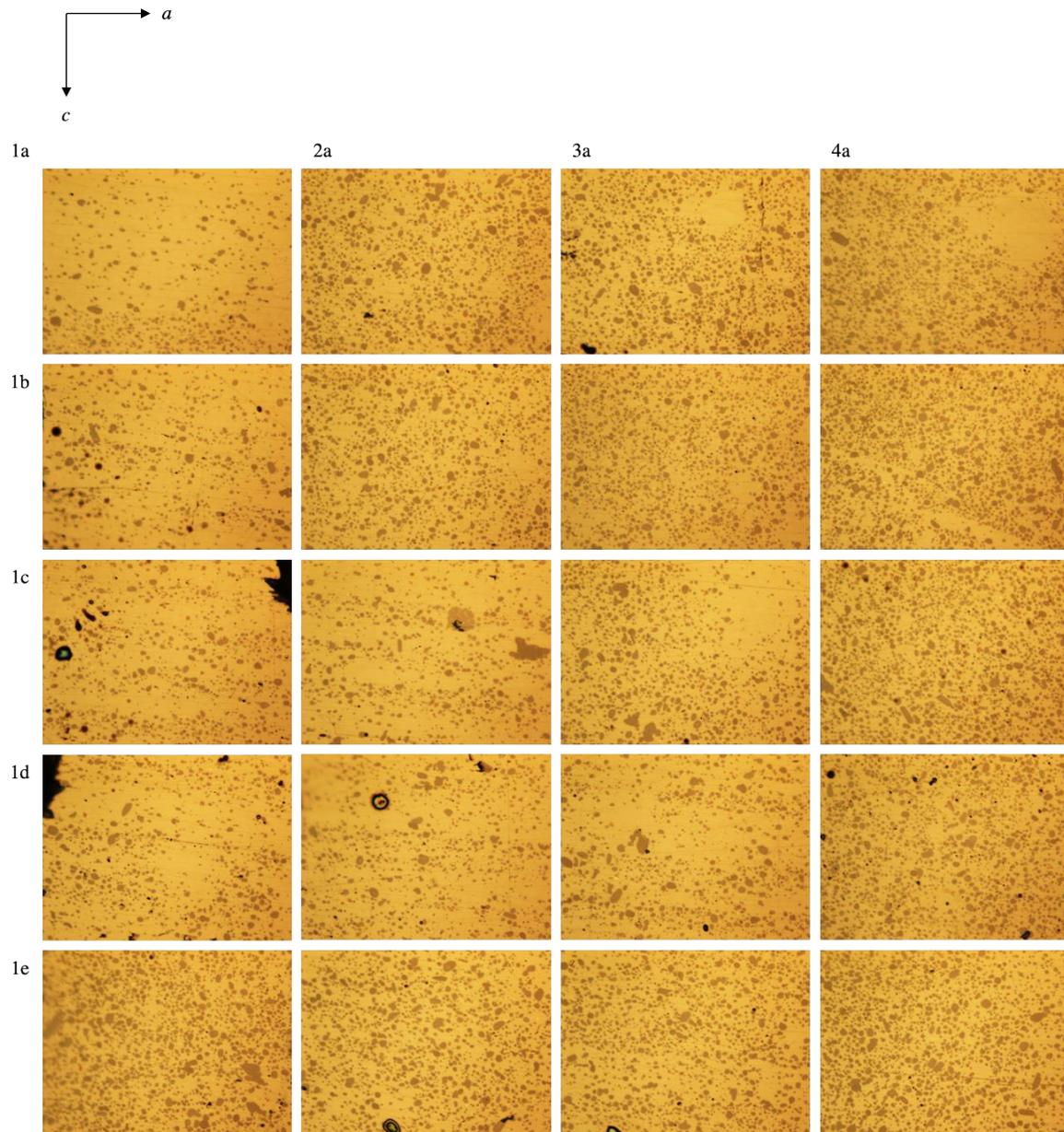
Figure 3.12. Optical micrographs taken at 1000× magnification of the Y-211 content in a typical 26 mm diameter YBCO single grain along the *ab* and *c* directions. The labels correspond to those presented in Figure 3.4.

(a)

(b)
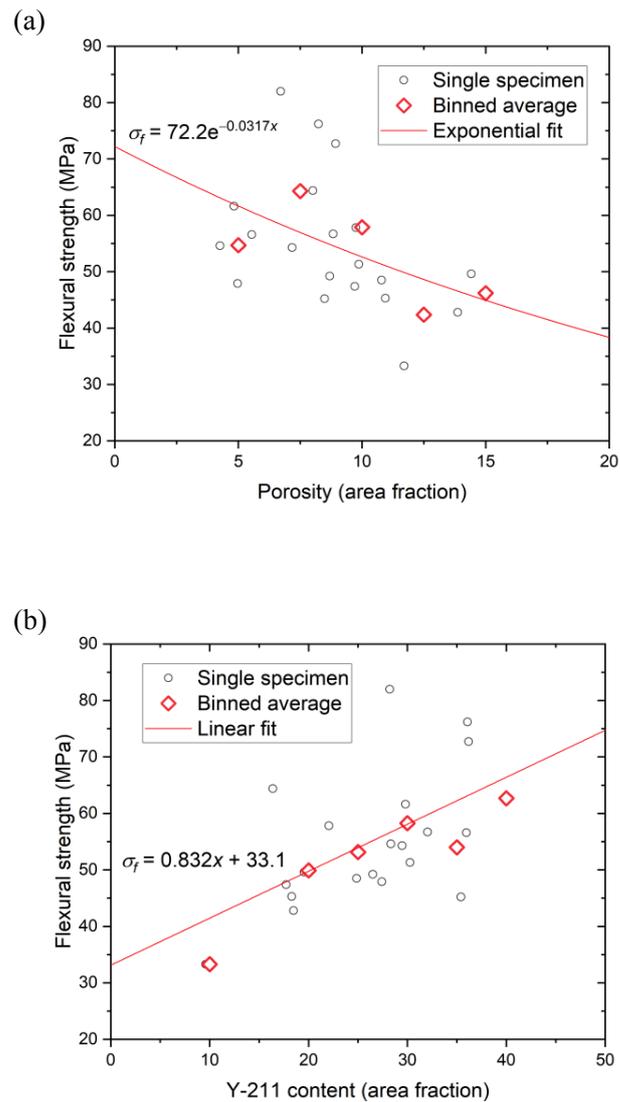
Figure 3.13. Measured flexural strength as a function of (a) the local porosity and (b) the local Y-211 content for a typical TSMG YBCO bulk superconductor. The circles correspond to data points for individual test beams and the diamonds correspond to the binned averages.

3.3.2.   Bulk-to-bulk variation in the tensile strength of YBCO

The 16 mm diameter YBCO single grains used for this study were grown in three batches and showed consistent peak trapped fields at 77 K, with an average of 0.460 ± 0.046 T at 77 K.

Figure 3.14 shows the probability of failure as a function of the applied stress for twelve discs characterised using the Brazilian test, with an example of a fractured sample shown in Figure

3.15. The probability of failure was approximated by assigning an equal probability to each of the failure strengths measured.

From the gradient of Figure 3.14, the Weibull modulus m was found to be 10.1, which is significantly higher than $m = 4.5$ calculated from the flexural strengths in Section 3.3.1 and $m \approx 5$ reported by previous studies in Table 3.1. This would suggest that, despite the high variation in fracture strength within a given bulk superconductor due to the microstructural inhomogeneities discussed in detail in Section 3.3.1, batch processing still produces bulk samples with highly consistent overall strengths. $m = 10.1$ is, in fact, comparable to Al_2O_3 ceramics [110]. Consequently, this suggests that batch processed bulk superconductors possess the high structural reliability required for practical applications and that the failure conditions of these materials can be predicted and modelled with fairly high precision.
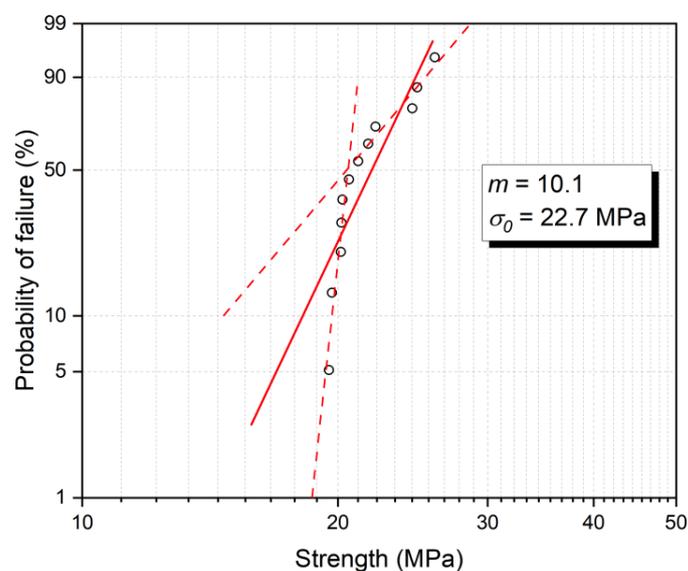
Figure 3.14. Weibull plot of the failure probability of twelve YBCO discs as a function of applied stress. The Weibull modulus and characteristic strength (value at 63.2 % probability of failure) have been calculated from the slope and intercept of the line of best fit. The plot shows the line of best fit for the entire dataset, which yielded a Weibull modulus of 10.1. It also shows separate fits for the low and high strength regimes, where the Weibull modulus exceeded 40 for the low strength regime.
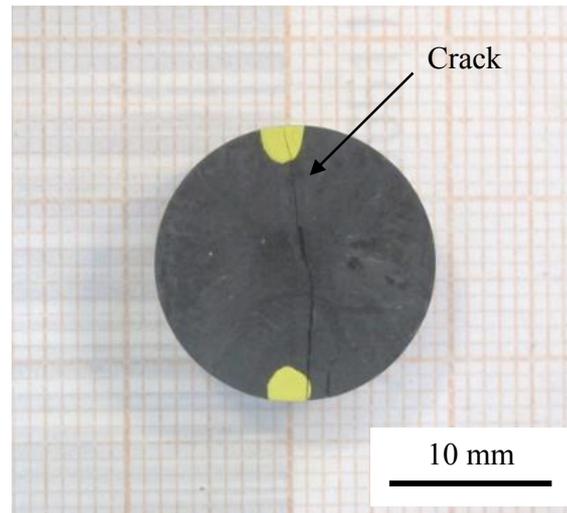
Figure 3.15. A typical 16 mm diameter single-grain YBCO bulk superconductor that fractured during the Brazilian test. The yellow marks on the sample indicate the direction of the applied compressive load. A hairline crack, as a result of tensile failure in the perpendicular direction, can be seen in the top surface of the sample.

The larger test volume of Brazilian discs, where whole 16 mm diameter bulk superconductors were placed in a stress field, in comparison to flexural beams, should yield a more reliable Weibull modulus value. Therefore, $m = 10.1$ can be seen as more representative of the (RE)BCO bulk magnets.

In addition, it is important to note that the magnitude of the measured tensile strength, which ranged from 19.5 MPa to 26.0 MPa, also correlates extremely well with magnetisation experiments conducted by Fuchs *et al.* [14], who deduced the tensile strength of YBCO bulk superconductors to be around 25 MPa based on the magnetic field (~ 8.5 T) at which samples cracked due to the Lorentz force. The procedure implemented by Fuchs *et al.* is a more direct means of determining the failure conditions of these materials when operated as trapped field magnets. It can be seen that, on the other hand, flexural strengths measured in this study and other studies exceed 25 MPa significantly. This discrepancy is expected as the entire bulk superconductor is placed under a stress field in the Brazilian test, whereas only a small beam, a fraction of the size of a typical bulk sample, is subjected to bending in the bend test.

3.4. Conclusions

In this study, the fracture strength of YBCO bulk superconductors was characterised using the three-point bend test and the Brazilian test, both of which offer the advantages of ease of sample preparation and scalability.

The three-point bend test enables the characterisation of a large number of beams extracted from a single bulk sample and can be used to identify the weakest and strongest regions within the sample. The bending modulus can also be determined for each beam, and therefore, for each position within the single grain. Mechanical data obtained using the bend test could be useful for the accurate modelling of the stress–strain characteristic of (RE)BCO bulk superconductors during magnetisation and for the design of mechanical reinforcements.

On the other hand, the Brazilian test enables cylindrical specimens to be characterised, which lends itself well to the natural geometry of as-grown and as-annealed bulk superconductors, and therefore greatly simplifies sample preparation. This is also a straightforward means of evaluating the overall strength of superconductor discs, allowing for a more accurate estimate of the magnetic field conditions at which catastrophic fracture is expected to occur.

The three-point bend test revealed a spatial distribution of flexural strength within YBCO samples at room temperature, which averaged 49.3 ± 12.7 MPa. The large scatter intrinsic to each single-grain YBCO was reflected by a low Weibull modulus of 4.5 across 60 specimens taken from the four bulk samples, which is in close agreement with several existing studies. The present study is significant in identifying that the scatter is not entirely random, as for sintered ceramics with a more homogeneous microstructure, but actually demonstrated a positional dependence as a result of the spatially varying microstructure. These microstructural defects and variations, in particular the porosity and Y-211 content, develop due to the seeded melt growth process but are fairly reproducible. As a result, the spatial distribution observed in the current study should be applicable to most (RE)BCO systems. At the very least, the procedure described can be implemented for any system of interest.

The bulk-to-bulk variability in strength was evaluated using the Brazilian test. Although a majority of studies in the literature have utilised the uniaxial tensile tests, flexure tests or hardness tests on small volumes of specimen extracted from a large bulk superconductor, the Brazilian test provides a means of determining the strength of whole bulk superconductor discs.

A Weibull modulus of 10.1 was determined for a batch of nominally identical YBCO discs, indicating a very narrow scatter in strength from one single-grain sample to another.

In conclusion, we have shown that despite the large scatter of strength within any given YBCO single-grain bulk superconductor due to the underlying microstructural variation with position, the batch processing of bulk superconductors can be used reliably to produce samples with very similar overall fracture strengths. This ultimately means that mechanical failure during magnetisation can be expected under similar field conditions, making these materials sufficiently reliable structurally for engineering applications.

Chapter 4

Strain measurements on GdBCO/Ag bulk superconductors during field-cooled magnetisation

To determine the exact point of failure, in spatial and temporal terms, of a bulk superconductor during magnetisation, the stress and strain evolution as a result of the Lorentz force must be modelled and measured. An understanding of such behaviour would benefit a strategy for targeted mechanical reinforcement and the choice of appropriate parameters for the magnetisation procedure. Furthermore, the results would also help give insight into possible deviation of the material properties and mechanical behaviour of a real bulk superconductor from an ideal scenario modelled in simulations.

In this chapter, spatially resolved measurement of the flux-pinning-induced strain in between a pair of large, single-grain GdBCO/Ag discs during field-cooled magnetisation is presented. The hoop and radial strains were measured at four positions along the radius of one of the bulk discs using cryogenic strain gauges aligned along the corresponding directions. By magnetising the sample stack at 64 K with various applied fields ranging from 5.0 T to 9.6 T, the biaxial stress and strain evolution were observed for different trapped fields within the stack. At 64 K, the stack was capable of trapping a maximum of 6.9 T at its centre.

The experimental strains were then compared to simulations conducted using a three-dimensional finite element model resembling the experimental set-up. Attempts to improve the agreement between the experimental and simulation results indicate that the realistic and inhomogeneous distribution of various material properties within a bulk superconductor, such as the Young's modulus and critical current density, must also be considered.

4.1. Background

4.1.1. Pinning-induced strain in (RE)BCO bulk superconductors

The use of strain gauges to measure the mechanical strain of a material is a conventional and well-established technique. The electrical resistance of a strain gauge transducer varies with the strain it undergoes, so when it is adhered to the material of interest it can be used to determine strain in the material as a function of parameters such as external force and temperature change. The various types of strain gauges include wire, metallic foil, single-crystal semiconductor and thin-film strain gauges. The type of strain gauge used in a certain application may be selected based on a number of factors including operating temperature, gauge resistance, gauge factor, magneto-resistivity and magnitude of the maximum expected strain.

A number of other means and techniques are available for measuring the deformation and strain of a material in-situ, including optical techniques like Fibre Bragg Grating (FBG) [111], [112] and Digital Image Correlation (DIC) [113]–[116]. These techniques have also been applied to measure strain in (RE)BCO bulk superconductors. For instance, Latka *et al.* used an array of FBGs to characterise the spatially-varying flux-pinning-induced strain in an YBCO bulk superconductor as a function of radial position during field-cooling and zero-field-cooling at 60 K [117]. Zeisberger *et al.* also used FBGs to measure the thermal expansion of melt-textured YBCO from 30 K to 300 K [118].

The metallic foil strain gauge, which is the most commonly used gauge type and the one used in the present study, works on the principle of electrical conductance and its dependence on the geometry of the conductor. When a strain gauge is stretched within its elastic limit, the metallic grid becomes longer and narrower, causing the end-to-end electrical resistance to increase. Conversely, if the gauge is compressed, the grid becomes shorter and wider, decreasing the electrical resistance. The sensitivity of a strain gauge is given by its gauge factor *GF*:

$$\frac{\Delta R}{R_G} = GF \times \varepsilon \tag{4.1}$$

Where ΔR is the change in the resistance of the gauge, which has a resistance of R_G when undeformed/unstressed, as a result of strain ε.

As the superconducting properties and trapped fields of (RE)BCO bulk superconductors were improved and it became clear samples could fracture at high field and low temperature as a result of the large Lorentz force, investigations were carried out using strain gauges to evaluate the stress and strain in bulk samples during magnetisation. Miyamoto *et al.* measured the strain at multiple positions on an YBCO disc, including the use of a strain gauge rosette at the centre, as the sample was field cooled from 10 T at 50 K [119], [120]. This was then repeated for YBCO and SmBCO, both containing 0 wt%, 10 wt% and 20 wt% Ag addition. The YBCO without Ag cracked during ramping of the external field and the position of the crack was reflected by signal overshoots in the gauges spanning the crack. On the other hand, YBCO samples containing Ag survived the magnetisation process.

More recently, Takahashi *et al.* reported measurement of strains in the circumferential direction in an EuBCO ring bulk superconductor during cooling from 298 K to 50 K and subsequent field cooled magnetisation from 5.3 T and 6.3 T at 50 K [121]. The experimental results were compared to numerical simulation results, which showed excellent qualitative agreement. Namba *et al.* expanded on the study by measuring the electromagnetic strains in the same EuBCO ring sample along both the hoop and radial directions [122], such that the hoop and radial stresses could be calculated. In addition to modelling the EuBCO bulk ring, they also revised the model to represent the exact experimental set-up by including the sample holder and any mechanical support structure, i.e. copper plates, indium sheets and stainless-steel bolt and nut. The results showed excellent qualitative and quantitative agreement.

Experimental studies were supported by developments in the modelling of the mechanical behaviour of bulk superconductors, which has helped explain where cracks tend to form during sample failure under load. Analytical studies of the stress evolution during magnetisation were first carried out by Ren *et al.* and Johannsen for infinitely long disc- and ring-shaped samples during field cooling and zero field cooling [67], [68]. They showed that for a bulk superconductor fully magnetised along the axial direction, the hoop and radial stresses are maximum at the centre with a magnitude of $\sigma_{max} = 0.71 \times (B^{*2}/2\mu_0)$ and decrease towards the edge. B^* is the trapped field at the centre of the superconductor and μ_0 is the permeability of free space. This would imply peak tensile stresses of up to 28 MPa and 113 MPa acting on the sample at trapped fields of 10 T and 20 T, respectively.

For a partially magnetised superconductor, the stress profile is instead flat at the centre, resembling the trapped field profile, with a magnitude less than σ_{max}. Ren *et al.* also showed

that according to the Bean model, the maximum stress experienced by the superconductor during magnetisation increases with increasing applied field, even when the applied field greatly exceeds the maximum trapped field $B^* = \mu_0 J_c R$ permissible by the critical current density J_c. This implies the lowest applied field, just sufficient to magnetise the sample completely, should be used in order to minimise the peak stress and avoid crack formation during the magnetisation process.

The stresses that develop during magnetisation have also been evaluated numerically using the finite element method and assuming the Bean model applies [123]. More recently, a number of authors, including Fujishiro $et\ al.$ [124] and Ainslie $et\ al.$ [125], have used numerical models to study the mechanical behaviour of bulk superconductors with a finite height and realistic $J_c(B)$ dependence. They have also investigated the influence of various parameters, such as the ramp rate of the external field, on the stress state.

Wu $et\ al.$ analysed the stresses that develop during pulsed field magnetisation [126], where both the electromagnetic and thermal stresses were evaluated. In pulsed field magnetisation, significant thermal stresses can develop as a result of the non-uniform heat generation across the superconductor as field penetrates, which leads to varying degrees of thermal expansion.

4.1.2. Motivation for the proposed study

The mechanical properties of bulk superconductors can be determined via mechanical tests on non-magnetised specimens in a tensile testing machine and discussed in the context of analytical solutions of the flux-pinning-induced stress within the superconductor, much like the study presented in Chapter 3. However, an exact understanding and validation of where a bulk superconductor is most severely stressed and when a crack is most likely to occur during magnetisation can only be achieved through in-situ measurement of the evolution of stress and strain as the sample is being magnetised.

The study proposed in this chapter contributes to the general understanding of the development of stress and strain in (RE)BCO bulk superconductors. This is one of the first studies to measure both the hoop and radial strains simultaneously in a single-grain bulk superconductor disc, which allows the hoop and radial stresses to be calculated through Hooke's law in cylindrical coordinates. Secondly, the effect of using an applied field that exceeds the maximum trapped

field considerably on the stresses during magnetisation has been established. Thirdly, the realistic and inhomogeneous distribution of a number of material properties spatially, which are observed regularly in melt processed samples but had not been modelled in great detail previously, have been determined empirically and incorporated into the simulations.

4.2. Experimental details

4.2.1. Strain measurements during magnetisation

Two single-grain, Ag-containing GdBCO bulk superconductors, approximately 40 mm in diameter and 12 mm in thickness, were fabricated by TSMG from commercial powders following the composition: (75 wt% $GdBa_2Cu_3O_7$ + 25 wt% Gd_2BaCuO_5) + 10 wt% Ag_2O + 1 wt% BaO_2 + 0.2 wt% Pt. The samples were fabricated and supplied by Dr Yunhua Shi. The quality of the single grains was first evaluated using field cooled magnetisation (FCM) at 77 K, where the samples showed peak surface trapped fields of 1.4 T and 1.7 T and high uniformity in the field profiles.

Eight CFLA–1–350–11 strain gauges (Tokyo Sokki Kenkyujo), with a gauge length of 1 mm, were attached to the top surface of the sample that trapped 1.7 T, at radial positions of r = 2.5 mm, 7.5 mm, 12.5 mm and 17.5 mm from the centre. The top surface here refers to the surface on which the seed crystal was placed during melt growth. The experimental set-up is shown in Figure 4.1. Four of the gauges were attached along the circumferential direction to measure the local hoop strains while the other four were attached along the radial direction to measure local radial strains. Strain gauge rosettes could have been used similarly to measure the perpendicular strains, however, the large size of the backing of the rosettes made that less preferable. A cryogenic epoxy adhesive EA–2A (Tokyo Sokki Kenkyujo) was used to bond the gauges to the surface of the sample following the recommended procedures. The mechanical strain measured by each gauge $\varepsilon = \Delta L/L = (1/GF) \times (\Delta R/R_G)$ was then determined via four-point resistance measurement using a nanovoltmeter (Keithley 2182A) with an excitation current of 0.5 mA from a current source (Keithley 2602A).

In addition, HGT–2101 transverse Hall sensors (Lake Shore Cryotronics) were attached at r = 0 mm and 10 mm for trapped field measurements, utilising the same excitation current as the strain gauges. The gauges and Hall sensors were placed in the middle of the growth sectors,

as shown schematically in Figure 4.1(b). The samples were then assembled using polyimide tape to form a stack as shown in Figure 4.1. Finally, the stack temperature was measured using a Cernox® sensor and controlled with a heater placed in good thermal contact with the samples, as the stack was cooled from all directions through helium gas.
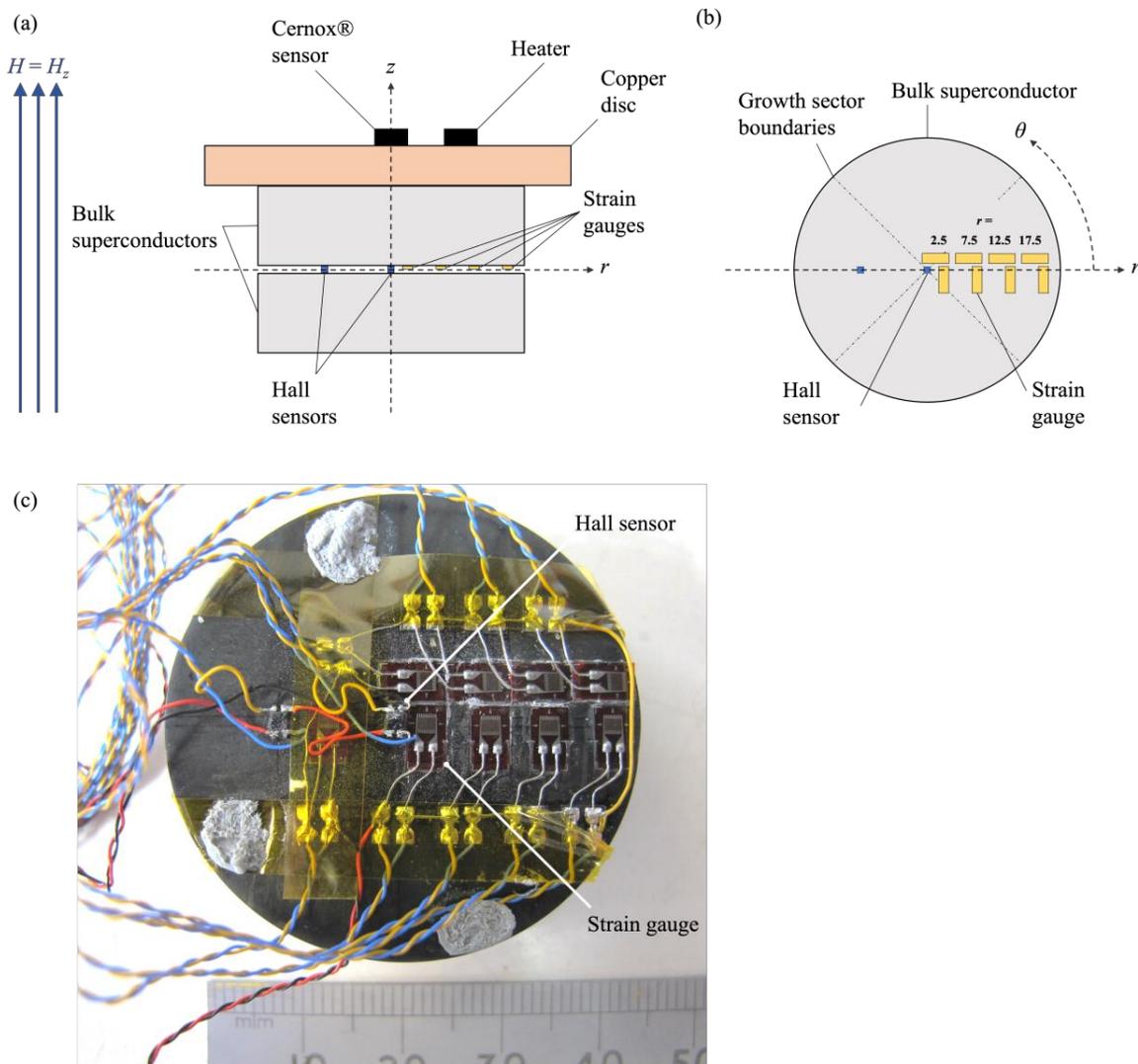
Figure 4.1. (a) Cross-sectional view of the experimental set-up for simultaneous measurement of the hoop and radial strains in a two-sample stack configuration, shown in an r–θ–z cylindrical coordinate system. Strain gauges were placed at $r = 2.5$ mm, 7.5 mm, 12.5 mm and 17.5 mm, while the Hall sensors were placed at $r = 0$ mm and 10 mm. (b) Top view of the measurement surface. (c) The 40 mm diameter GdBCO/Ag sample with strain gauges and Hall sensors attached to its top surface.

A LabView program was written for the continuous acquisition of the strain gauge and Hall sensor voltages, which were then converted into strains (in micro-strain $\mu\varepsilon$) and trapped fields, respectively.

The GdBCO/Ag stack was magnetised by FCM in the 100 mm variable temperature bore of a 12 T superconducting magnet. The stack was cooled from 100 K to 64 K in an external applied field B_{app} = 5.0, 6.0, 7.0, 8.0, 9.0 and 9.6 T. The external field was subsequently ramped down at a constant rate of 0.12 T/min once temperature of the samples stabilised at 64 K. A constant and sufficiently slow ramp rate of 0.12 T/min was chosen such that thermal effects could be ignored. A target temperature of 64 K was chosen such that the resultant stresses would not exceed the tensile strength of GdBCO/Ag bulk samples, which have been reported to be 34 ± 3 MPa at 77 K [92]. After FCM at each B_{app}, the stack was warmed slowly to 100 K to ensure all of the trapped field was removed before the next set of measurements.

4.2.2. Critical current density measurement

$J_c(B)$ behaviour has been shown in experimental studies to vary across a large (RE)BCO single grain [74], [127], [128]. This is expected in part due to the melt growth process, where the concentration and average particle size of RE-211 pushed or trapped by the growth fronts vary throughout the growth process due to the varying degree of undercooling. Additionally, the supply of liquid phase at any particular point in time during growth also plays a part due to its reaction with RE-211 to form RE-123. Therefore, the microstructures observed in (RE)BCO bulk materials have been reported to vary considerably even within the same sample, including where RE-211 content and average particle size have been shown to change with distance from the seed [109]. The vital role of RE-211 in flux pinning would consequently lead to variations in the $J_c(B)$ characteristics between different parts of the sample. In addition, grain misorientation angle and impurities are expected to increase gradually with distance from the seed, which would also impact J_c.

To determine how the $J_c(B)$ behaviour changes across the GdBCO/Ag bulk superconductors in this study, a SQUID magnetometer (Quantum Design MPMS XL) was used to measure the magnetisation $M(H)$ loops of small cuboid specimens cut from a 25 mm diameter representative GdBCO/Ag bulk single grain, with approximate specimen dimensions of 2.0 mm $\times$ 2.2 mm $\times$ 1.6 mm. The $J_c(B)$ curves at 77 K and 64 K were then calculated for each

specimen/position using the extended Bean model [34]. The coordinate system used by this study to identify the specimens is shown in Figure 4.2.

Cross section of bulk superconductor
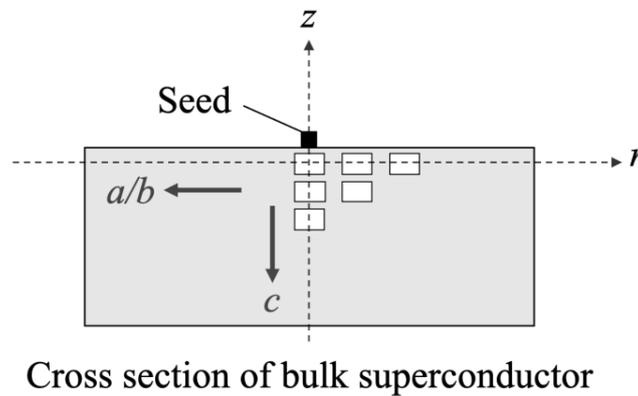
Figure 4.2. *r–z* coordinate system used to identify specimens cut from the parent/representative bulk superconductor for critical current density and Young's modulus measurements. For example, the specimen directly beneath the seed is labelled as $r = 0$ mm and $z = 0$ mm. The crystallographic directions are also shown.

4.2.3. Young's modulus measurement

As discussed in Chapter 3, the mechanical properties of a bulk superconductor can display a spatial distribution as a result of the microstructural variations introduced during melt growth. The findings of that part of the study prompted examination of the spatial distribution of Young's modulus E across a typical GdBCO/Ag single grain, which is important since E governs the stress–strain behaviour of a material and affects how much it would deform when subject to a given body force.

To determine the spatial distribution of E, three-point bend tests were carried out at room temperature on bar specimens of dimensions of 2.0 mm × 1.5 mm × 20 mm (length actually varied depending on where the beam was taken from the sample but had to be at least 20 mm) cut from a 31 mm diameter representative GdBCO/Ag bulk single grain. The coordinate system used to identify the specimens is shown in Figure 4.2.

The load was applied at a crosshead speed of 0.012 mm/min and a strain gauge attached to the centre of the tensile side of each beam was used to record the resultant strain ε, which allowed E to be calculated for each beam and therefore each position in the superconductor disc.

$$\sigma = \frac{3Fl}{2bd^2} \tag{4.2}$$

$$E = \frac{\sigma}{\varepsilon} \tag{4.3}$$

Where σ is the tensile stress generated by load F on a rectangular beam of length l, width b and thickness d.

The Young's modulus could also have been estimated from the gradient of the load–displacement curve measured by the crosshead of the tensile testing machine. However, due to the relatively small displacements involved, attaching a strain gauge to each beam to determine the strain directly was expected to yield more accurate results.

4.3.   Modelling framework

4.3.1.   Analytical and numerical models

Modelling of (RE)BCO bulk superconductors is a powerful tool for reproducing experimental results, assisting in the interpretation of these results and predicting the performance of devices or machines based on these materials [129]. Modelling can be carried out either analytically or numerically.

An analytical solution is an exact mathematical solution to a physics problem. Since analytical solutions are given as mathematical expressions, they provide a clear view of the response of a system to changes in various variables and subject to any assumption in the model. Although analytical models can be easier, faster and more accurate than numerical methods, such as those based on the finite element method (FEM), analytical models are restricted to particular geometries and assumptions.

On the other hand, FEM can readily handle extremely complex geometries and boundary conditions for a wide variety of problems. FEM is a computational technique that involves

solving the space- and time-dependent partial differential equations (PDEs) representing the underlying laws of physics, such as Maxwell's equations, linear elasticity equations and the conservation of energy, relevant to the problem in-hand by constructing approximations to these equations and solving for their solutions using numerical methods. In turn, the solution obtained is an approximation to the exact solution to the PDEs with the minimal associated error function. To solve a complex problem, a system is divided into smaller parts called finite elements, which are connected at nodes, and for which local solutions are found before a global solution can be constructed.

4.3.2. Homogeneous case

The field cooled magnetisation process was modelled using three-dimensional (3D) finite element models based on the *H*-formulation and implemented in the commercial finite element software package COMSOL Multiphysics [125]. The 'Magnetic Field Formulation', 'Heat Transfer in Solids' and 'Structural Mechanics' interfaces were coupled together to allow for a comprehensive study of, firstly, the electromagnetic stresses σ and strains ε arising from the interaction between the current and magnetic field when the sample is in the superconducting state; and secondly, the projected trapped field, which would indicate whether the $J_c(B)$ characteristic used in the model was similar to that of the bulk superconductors used in the experiments.

The model implemented in COMSOL is shown in Figure 4.3. To minimise processing time, symmetry has been applied at the boundaries such that only one-eighth of a single GdBCO/Ag sample had to be modelled in order to construct a complete solution.

In this study, two models were constructed, namely the 'homogeneous' case and the 'inhomogeneous' case. The homogeneous model was an extension of work carried out by Ainslie *et al.* [125] and was used to provide a basis for comparison. The model assumes uniform material properties across the whole superconductor. The full list of relevant properties is provided in Table 4.1. In practice, large, single-grain bulk superconductors exhibit noticeable inhomogeneity in material properties as a direct result of the growth process, which is why an inhomogeneous case was also developed to investigate the influence of spatial variations in particular material properties.
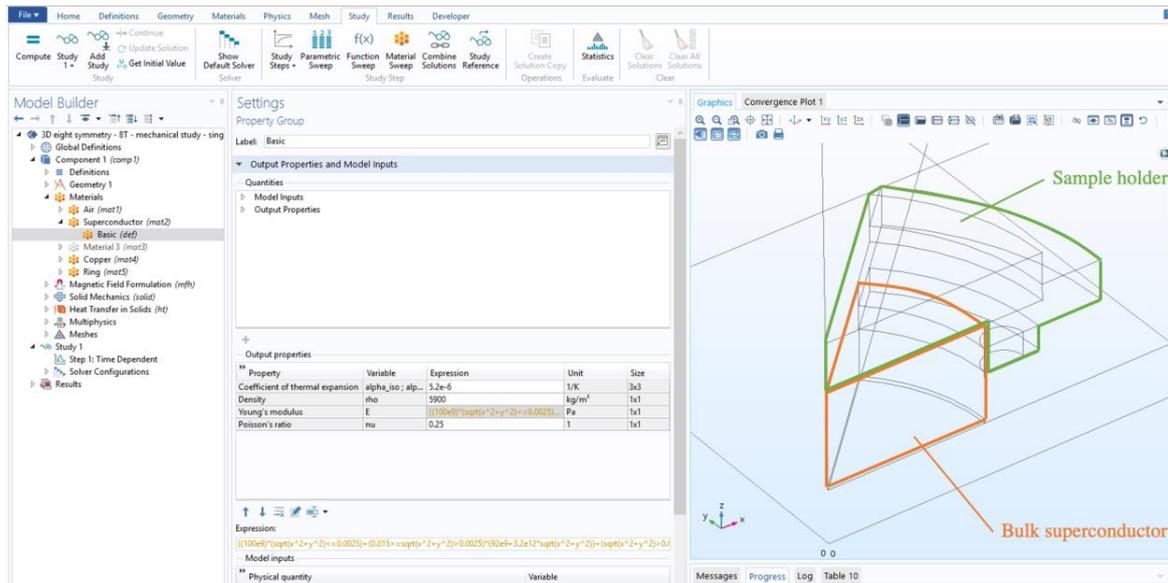
Figure 4.3. The COMSOL user interface, which shows, on the left, the modules used for the modelling of the mechanical behaviour of a bulk superconductor disc during magnetisation. The geometry built in COMSOL is shown on the right, which reflects the experimental set-up used. The bulk superconductor and sample holder (stainless steel and copper) are highlighted.

The form of $J_c(B)$ in Equation (4.4) was proposed by Jirsa *et al.* to fit the pronounced fishtail effect observed in the magnetic hysteresis loop of (RE)BCO single crystals [130]. This has been used to fit and extrapolate the experimentally measured $J_c(B)$ data (which could only be measured up to a maximum field of 5 T with the SQUID magnetometer available) to the required field, as shown in Figure 4.4. J_{c1}, J_{c2}, B_L and B_{max} are the fit parameters. y is a fit parameter normally set as 1.0.

$$J_c(B) = J_{c1} exp\left(-\frac{B}{B_L}\right) + J_{c2}\frac{B}{B_{max}} exp\left[\frac{1}{y}\left(1 - \left(\frac{B}{B_{max}}\right)^y\right)\right] \tag{4.4}$$

The non-linear relationship between the electric field E and the current density J of the superconductor, as described in Equation (4.5), was also included in the model. This relationship, commonly referred to as the E–J power law, is used in simulations to model the resistivity and flux creep of the material.

$$E = E_0 \left(\frac{J}{J_c}\right)^n \qquad (4.5)$$

Where E_0 is the characteristic electric field, J_c is the critical current density and n is the parameter used to describe the behaviour of the superconductor.

$n = 20$ is usually assumed in the modelling of high-quality (RE)BCO bulk superconductors with a low rate of field decay. When $n = 1$, the E–J power law becomes the Ohm's law. When n approaches ∞, one gets the Bean critical state model.
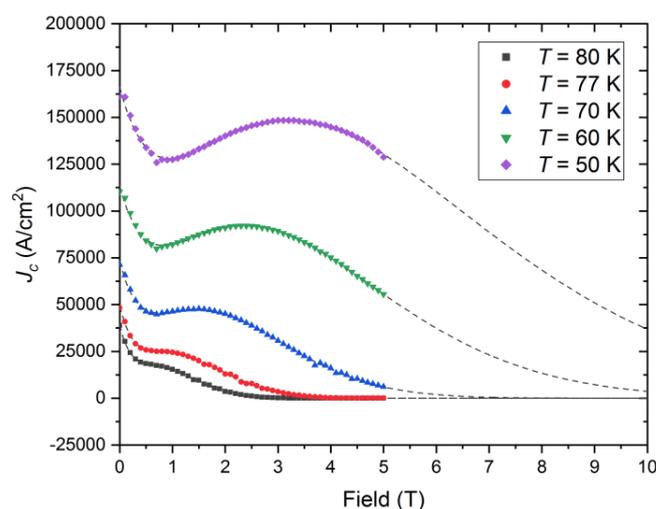
Figure 4.4. $J_c(B, T)$ used in the homogeneous model, which has been obtained experimentally from a single, representative SQUID specimen cut from a large, single-grain GdBCO/Ag bulk superconductor and measured up to 5 T over a temperature range of 50 K to 80 K. This $J_c(B, T)$ is identical to the one presented in [125], [131], [132]. The curves have been extended to 10 T using the equation presented by Jirsa *et al.* [130]. The data were input into the model using interpolation with temperature and field as the two variables.

Table 4.1. Material properties and experimental parameters used in the homogeneous model.

Parameter	Description	Value	Reference(s) (if applicable)
n	n value for the E–J power law	20	[129]
E_0	Characteristic electric field for the E–J power law	1×10^{-4} V/m	[129]
$J_c(B, T)$	Field- and temperature-dependent critical current density	Interpolation from data on a single SQUID specimen (Figure 4.4)	[125], [131], [132]
E	Young's modulus	100 GPa	[133]
v	Poisson's ratio	0.33	[134]
ρ	Density	5900 kg/m^3	[135]
κ_{ab}	Thermal conductivity along the ab-plane	20 W/mK	[129]
κ_c	Thermal conductivity along the c-axis	4 W/mK	[129]
C	Specific heat capacity	Measured data	[131]
α	Coefficient of thermal expansion	5.2×10^{-6} /K	[133]
T	Operating temperature	64 K	
dB/dt	Ramp rate of the external field	0.002 T/s	

4.3.3.   Inhomogeneous case

The two material inhomogeneities this study considered were the critical current density $J_c(B)$ and Young's modulus E, as the inhomogeneous case incorporated the positional dependence of these properties into the bulk superconductor. All other aspects of the two models, such as mesh size, experimental parameters and modelling framework, were identical.

The positional variations of $J_c(B)$ and E were determined empirically from smaller representative samples given that the large 40 mm diameter GdBCO/Ag samples needed to be preserved for future strain and trapped field measurements.

$J_c(B)$ measured at 77 K is shown in Figure 4.5, which is symmetric about the central axis. The symmetry confirms the SQUID specimens were extracted from appropriate locations within the bulk single grain. The $z = 0$ mm plane denotes the top surface of the superconductor, which is where the strain gauges would have been attached. Figure 4.6 shows the $J_c(B)$ curves measured at 64 K at various positions. It is clear from the $J_c(B)$ comparisons that $J_c(B)$ varies significantly, in terms of magnitude and shape, along both the horizontal plane, as shown in Figures 4.6(a) and (c); and the vertical plane, as shown in Figure 4.6(d).

Some trends can be deduced from Figures 4.5 and 4.6. Firstly, $J_c(0\text{ T})$ appears to reach a maximum at some distance away from the seed crystal, then drops-off with increasing distance, i.e. towards the edge of the sample. Secondly, the secondary peak appears to shift towards $\mu_0H = 0$ T in position and decrease slowly in magnitude with increasing distance from the seed.

The change in shape of the $J_c(B)$ with position can be understood in terms of the pinning mechanisms and the underlying variations in the microstructure. The two types of pinning are discussed in detail by Koblischka and Murakami [136]. The insulating RE-211 inclusions are effective across the entire temperature range and are primarily responsible for the "quasi-background" pinning and the central peak at $J_c(0\text{ T})$, which decays with increasing field. This is the so-called δl-pinning, which results from a scatter of the electron mean free path l. The presence of RE-211 particles does not affect significantly the secondary peak, i.e. the fishtail, provided their concentration is below a certain limit. This can effectively explain the observed peak in $J_c(0\text{ T})$ with radial position in Figure 4.5(b) and Figure 4.6(b) since RE-211 concentration is expected to increase gradually with distance from seed, resulting in a peak in J_c where RE-211 concentration is optimal before J_c drops off further away from the seed.
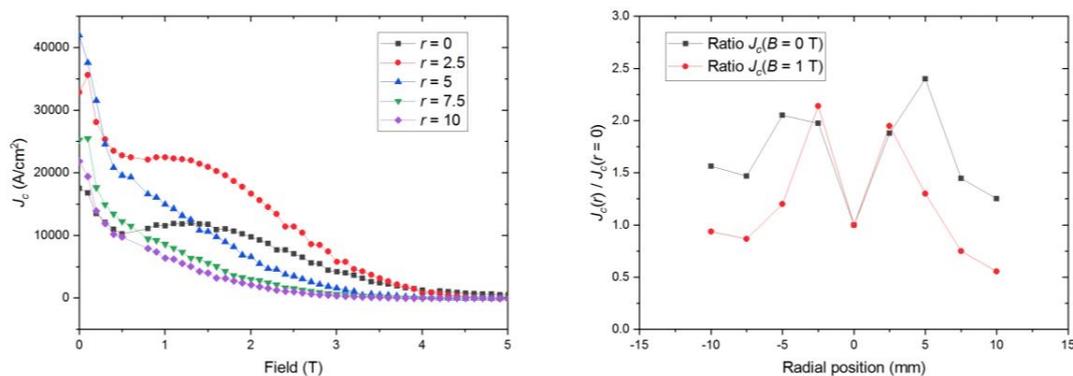
Figure 4.5. (a) $J_c(B)$ measured at 77 K at different radial positions r along the top surface $z = 0$ mm of the 25 mm diameter representative GdBCO/Ag bulk, single grain superconductor. (b) Ratio of $J_c(0$ T) and $J_c(1$ T) at position r along the top surface to the $J_c(0$ T) and $J_c(1$ T) at $r = 0$ mm, i.e. directly underneath the seed.

On the other hand, the secondary peak effect, where pinning strength actually increases with increasing field up to an intermediate field, is the so-called δT_c-pinning regime. This is primarily a property of the superconducting matrix, including the presence of oxygen vacancy clusters and LRE/Ba solid solution, resulting in a spatial scatter of the superconducting transition temperature T_c.

The δl and δT_c pinning contributions are also represented in Equation (4.4) from Jirsa *et al.*, where one contribution is primarily responsible for the central $J_c(B)$ peak at 0 T and the other is responsible for the formation of a secondary peak at an intermediate field. It can be seen from the $J_c(B)$ curves in Figures 4.5 and 4.6 that the peak of the fishtail generally shifts towards the $\mu_0 H = 0$ T axis with distance from the seed.

The spatial distribution of $J_c(B)$ observed in the present study is not abnormal, as similar trends in $J_c(B)$ have also been reported by Nariki *et al.* for their GdBCO/Ag samples [137].
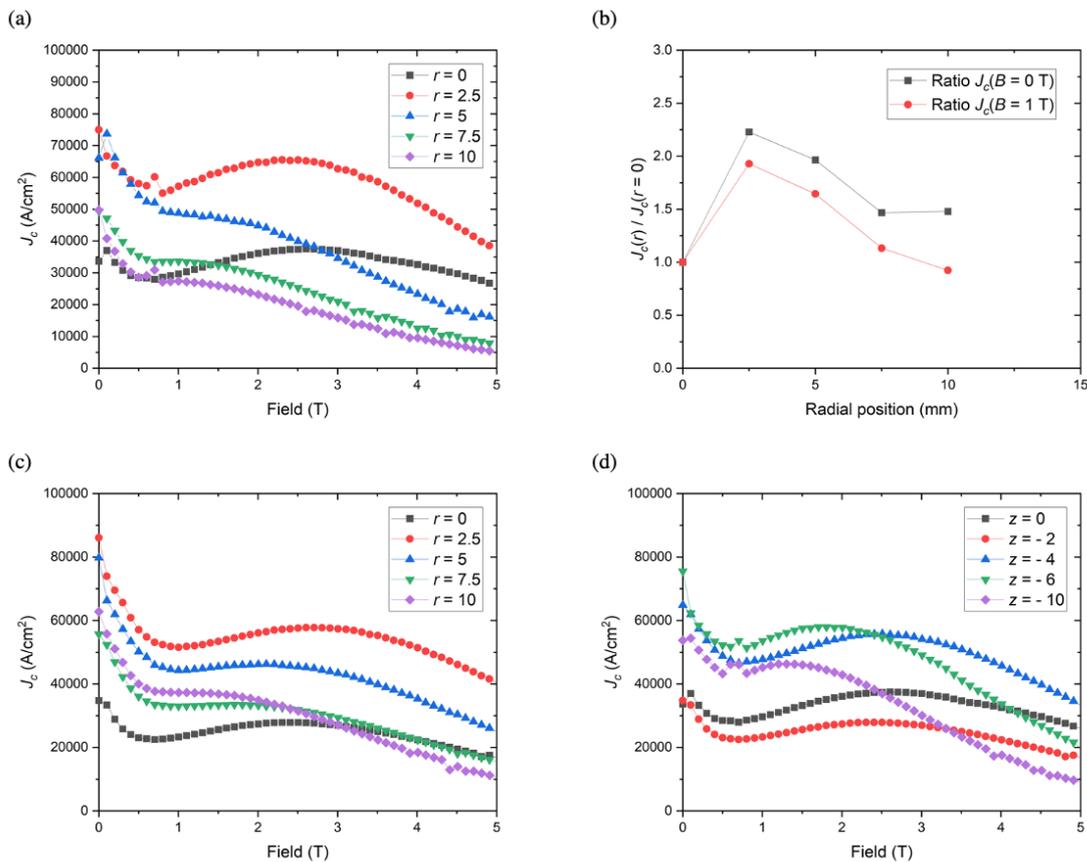
Figure 4.6. (a) $J_c(B)$ measured at 64 K at different radial positions r along the top surface $z = 0$ mm of the 25 mm diameter representative GdBCO/Ag bulk, single grain superconductor. (b) Ratio of $J_c(0\text{ T})$ and $J_c(1\text{ T})$ at position r along the top surface to the $J_c(0\text{ T})$ and $J_c(1\text{ T})$ at $r = 0$ mm, i.e. directly underneath the seed. (c) $J_c(B)$ measured at different radial positions r along $z = -2$ mm. (d) $J_c(B)$ measured at different vertical positions z along $r = 0$ mm.

The spatial variation of E was subsequently determined for a representative GdBCO/Ag sample at room temperature, and the results are shown in Figure 4.7. It can be seen the top surface shows significant random scatter whilst the mid-plane, specifically across $z = -4$ mm, exhibits increasing E towards the edge of the sample. This can be explained by considering the porosity within the bulk superconductor. Porosity is generally higher at the centre of the sample and decreases towards the surface. Since E decreases exponentially with porosity, the centre of a bulk superconductor is expected to exhibit lower E compared to that at its surface. Furthermore, since RE-211 particles are stiffer than the surrounding RE-123 matrix, increasing concentration of RE-211 away from the seed will also result in increasing E.
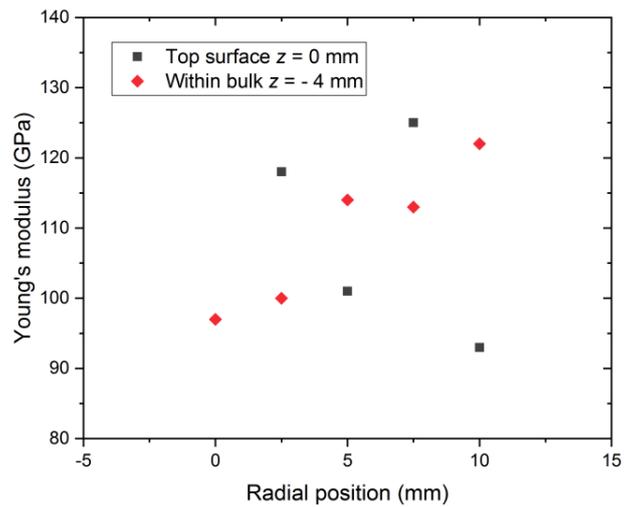
Figure 4.7. Young's modulus measured at different radial positions along the top surface and approximate mid-plane of a 31 mm diameter representative single-grain GdBCO/Ag bulk superconductor.

The origin of the scatter in E measured along the top surface of the sample is less clear but could potentially be due to the additional effect of different concentrations of Ag particles throughout the sample or to surface defects introduced during melt growth.

Lastly, an additional feature was added to the bulk superconductor in the inhomogeneous model to reflect particle pushing–trapping by the growth fronts during melt processing and the development of a "square" grain as a result of the formation of four a-growth sectors.

A thin layer 2 mm in thickness has been included in the model from the outer edge of each growth sector, as illustrated in Figure 4.8, where it has been assumed that there is significantly higher concentration of unreacted RE-211 and other impurity phases. This follows from visual observations of as-grown (RE)BCO single grains, examples shown in Figure 4.9, where particle build-up can be seen on the circumferential surface of the samples outside the growth sectors. The photographs are from [138]–[142]. Moreover, the proposed square grain geometry would also support the occasional observation of trapped field profiles which are somewhat square in appearance on cylindrical samples. The assumptions used for these edge layers were $E = 200$ GPa and $J_c = 0$ A/m^2.
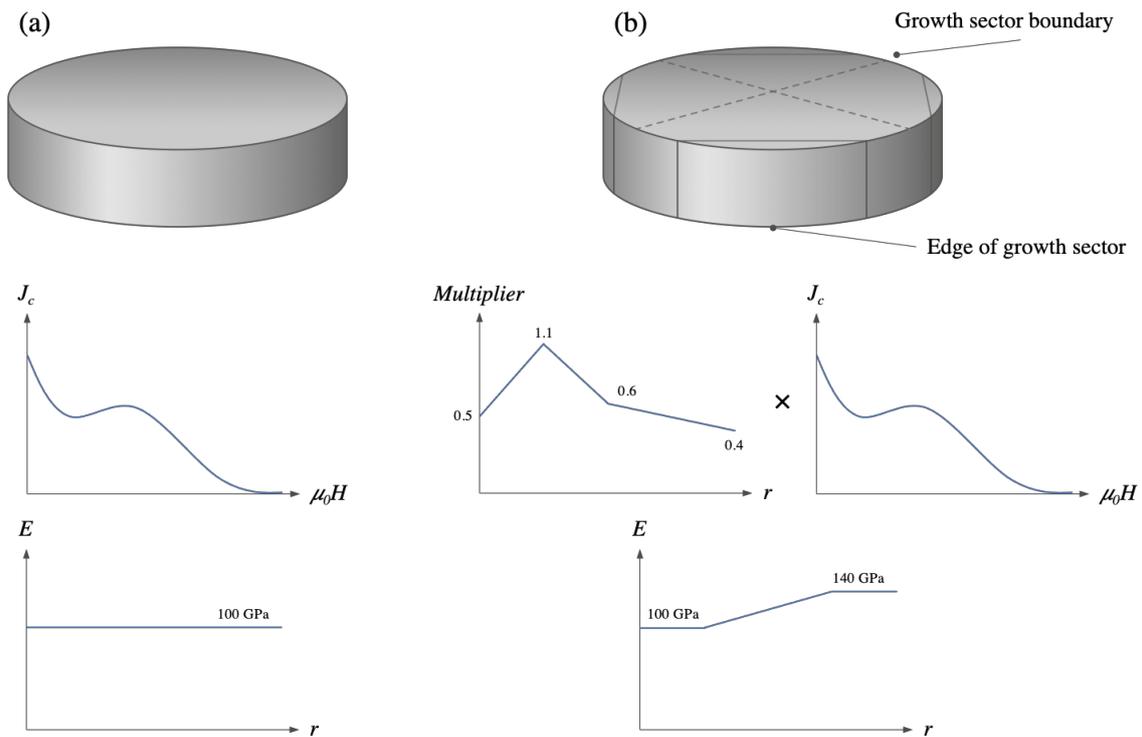
Figure 4.8. (a) Illustration of the homogeneous model, where perfect homogeneity was assumed for the superconducting and mechanical properties. (b) Illustration of the inhomogeneous model, where radial dependencies and an edge layer were included to reflect the properties of a realistic (RE)BCO single-grain bulk superconductor.

Photographs of single grains with signs of accumulation of RE-211 particles towards the edge of the growth sectors, removed for copyright reasons.

Figure 4.9. Photographs of typical YBCO and GdBCO/Ag single grains reported in the literature. Accumulation of RE-211 secondary phase and impurities is visible towards the edge of the growth sectors. (a) 22 mm diameter TSMG YBCO manufactured by Chaud *et al.* [138] (b) 16 mm diameter TSMG YBCO manufactured by Chaud *et al.* [139] (c) YBCO grown using a modified infiltration growth technique by Li *et al.* [141] (d) Recycled GdBCO/Ag single grains, 25 mm in diameter, produced by Shi *et al.* [142]

4.4. Results and discussion

4.4.1. Trapped field at the centre of the stack

Figure 4.10 shows the field measured at the centre ($r = 0$ mm) and halfway along the radius ($r = 10$ mm) on the top surface of the GdBCO/Ag sample in the stack, i.e. measured between the two GdBCO/Ag samples. The fields were measured as the external field was decreased from various initial/applied fields B_{app} to zero at a constant rate of $dB/dt = 0.12$ T/min.

At 64 K, the maximum trapped field $B_{trapped}$ achievable at the centre of the stack was 6.9 T, as shown in Figure 4.10, and applying external fields greater than 8 T did not result in a higher trapped field at the end of FCM. The data also show that the measured fields overlap towards the end of the ramp, which is especially clear for measurements taken at $r = 10$ mm. This implies that the J_c distribution induced within the samples as the external field was ramped down to a certain point/value must have been independent of the magnitude of B_{app} used to magnetise the samples. This observation will later help to explain the strains and stresses observed for the wide range of B_{app} implemented.

4.4.2. Hoop and radial strains for an applied field of 8 T

This sub-section will focus on the results for $B_{app} = 8$ T since the bulk stack was only fully magnetised when $B_{app} \geq 8$ T.

The field dependence of the hoop and radial strains, denoted by ε_θ and ε_r respectively, measured at different positions on the bulk superconductor are shown in Figure 4.11. The electromagnetic strains were assumed to be zero at the start of FCM since persistent currents were not yet induced.

During FCM, all hoop strains ε_θ increased (sample in tension) as the external field was ramped down, exhibiting higher values towards the centre of the sample. This is expected as the Lorentz force acts radially outwards, resulting in tensile hoop stress that should be highest at the centre of a cylindrical sample. On the other hand, most radial strains ε_r increased at the beginning of FCM, reaching a maximum in tension before becoming compressive towards the end of the FCM process. This was not expected for a cylindrical superconductor as ε_r is expected to follow a similar trend to ε_θ according to analytical and numerical simulations.
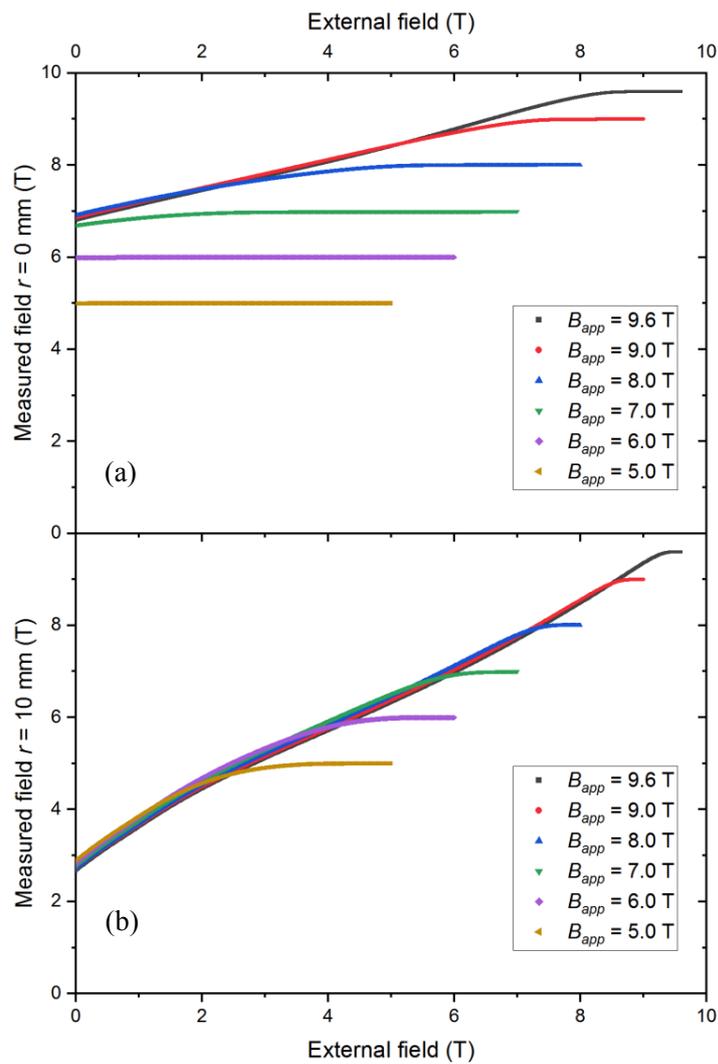
Figure 4.10. Trapped fields, achieved by field cooling, measured at (a) $r = 0$ mm and (b) $r = 10$ mm between the two-sample GdBCO/Ag bulk stack during ramp down of the external field from different applied fields B_{app} at $T = 64$ K.
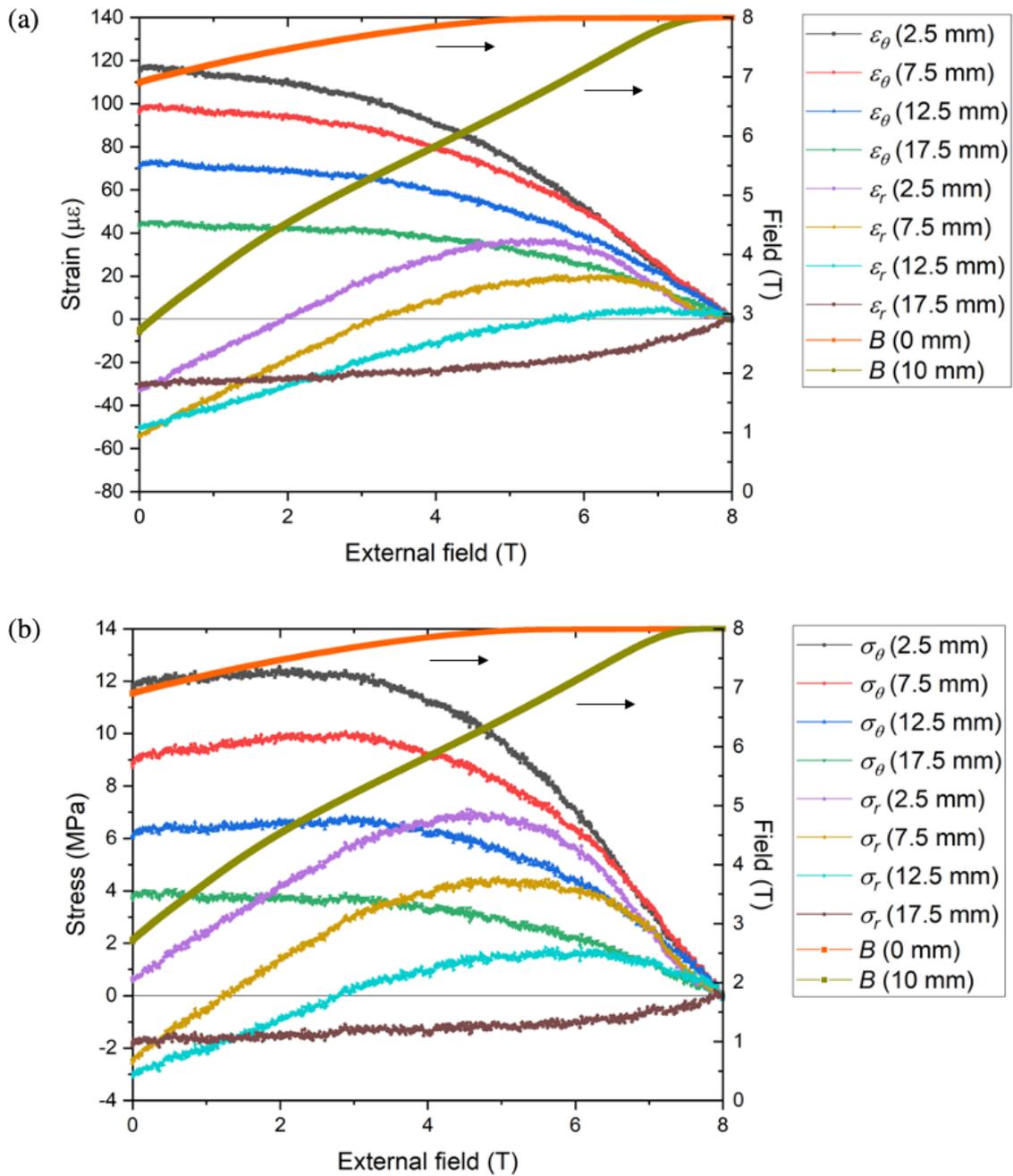
Figure 4.11. (a) Hoop and radial strains, denoted by ε_θ and ε_r respectively, measured along the radius of the bulk superconductor during ramp down of an 8 T applied field. The measured fields are shown on the secondary y-axis. (b) Hoop and radial stresses, denoted by σ_θ and σ_r respectively, along the radius of the bulk superconductor, as calculated from the measured strains.

The hoop and radial stresses, denoted by σ_θ and σ_r respectively, were subsequently calculated using Hooke's law, Equations (4.6) – (4.8), by assuming $E = 100$ GPa, $v = 0.33$ and $\sigma_z = 0$ (i.e. plane stress applies, which assumes the sample is a thin body and is only acted upon by stresses along the *ab*-plane).

$$\varepsilon_r = \frac{1}{E}[\sigma_r - v(\sigma_\theta + \sigma_z)] \tag{4.6}$$

$$\varepsilon_\theta = \frac{1}{E}[\sigma_\theta - v(\sigma_r + \sigma_z)] \tag{4.7}$$

$$\varepsilon_z = \frac{1}{E}[\sigma_z - v(\sigma_\theta + \sigma_r)] \tag{4.8}$$

The maximum hoop stress measured during FCM was $\sigma_\theta(r = 2.5 \text{ mm}) = 12.6$ MPa when the external field was decreased to 2.0 T. σ_θ then decreased slightly to $\sigma_\theta(r = 2.5 \text{ mm}) = 11.8$ MPa by the end of FCM. A comparison to the analytical solutions presented by Ren *et al.* [67] for an infinitely long superconductor shows the final hoop stress to be in agreement, as the analytical solution predicts $\sigma_\theta(r = 2.5 \text{ mm}) = 10.8$ MPa based on the 6.9 T trapped field of the stack. On the other hand, the maximum radial stress experienced by the sample was $\sigma_r(r = 2.5 \text{ mm}) = 7.1$ MPa when the external field was at 4.5 T, peaking significantly earlier than the hoop stress. σ_r then decreased to $\sigma_r(r = 2.5 \text{ mm}) = 0.6$ MPa by the end of FCM. In comparison, Ren *et al.* predict analytically $\sigma_r(r = 2.5 \text{ mm}) = 9.7$ MPa.

The stress profiles, which are shown in Figure 4.12, peak at the centre of the sample. These are consistent with analytical solutions as well as experimental observations that cracks tend to initiate at the centre of a superconductor disc and that cracks tend to occur during FCM and not afterwards.
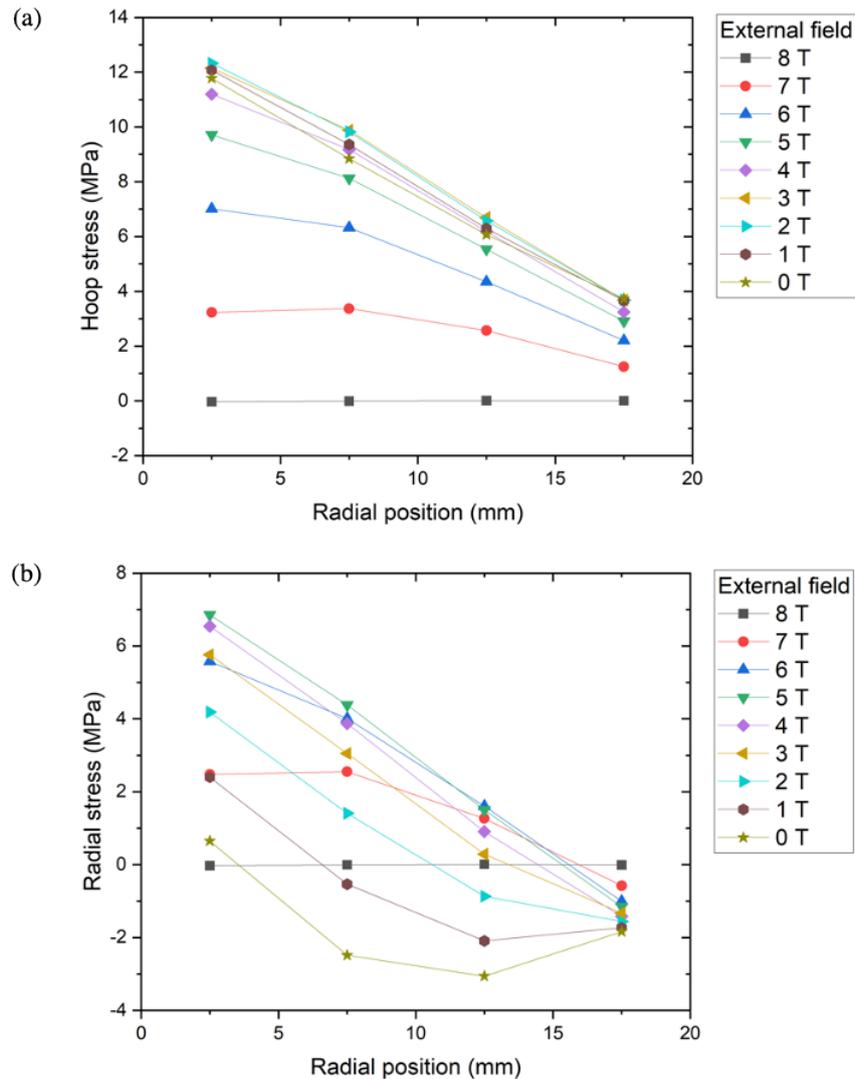
Figure 4.12. Evolution of the (a) hoop and (b) radial stresses at discrete points along the radius of the sample during ramp down of an 8 T applied field. Each set of data represents the stress state at field intervals of 1 T.

4.4.3. Hoop and radial strains for all applied fields

The next part of the study was to investigate the effect of different applied fields on the strains and stresses experienced by the bulk superconductor. This is important as solutions based on the Bean model predict the maximum stresses experienced by a bulk superconductor to continue to increase with increasing applied field regardless of the magnitude of the applied field relative to the trapped field capability of the superconductor. This means the application

of an external field just sufficiently large to magnetise the sample fully would be ideal. However, the field-trapping capability of a sample is often not known precisely prior to trapped field measurements, making the choice of an appropriate magnetising field difficult.

Figure 4.13 presents the strains and stresses at $r = 2.5$ mm since both the hoop and radial strains are most tensile at $r = 2.5$ mm and bulk superconductors fail in tension. The strain and stress evolution are shown for all B_{app}, which ranged from 5 T to 9.6 T.
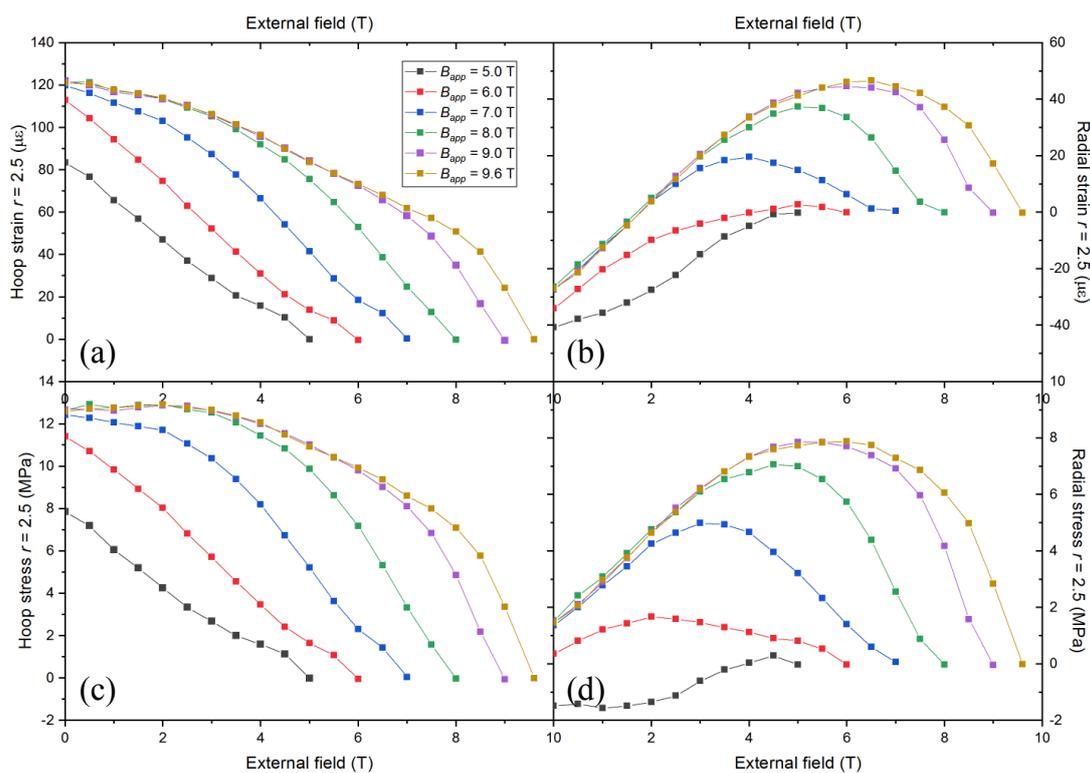
Figure 4.13. (a) Hoop and (b) radial strains measured at $r = 2.5$ mm during ramp down of the external field for all B_{app}. (c) Hoop and (d) radial stresses, as calculated from the strains, at $r = 2.5$ mm during ramp down of the external field for all B_{app}.

The bulk superconductor stack was not fully magnetised for $B_{app} < 8$ T, resulting in hoop and radial stresses that are smaller than that for the cases of $B_{app} \geq 8$ T. This can be understood in terms of the Lorentz force distribution $F_L = J \times B$, where increasing the applied field increases the region of superconductor penetrated by field as well as the resultant trapped field. This increases the magnitude of the body force directed radially outwards as well as the volume of material acted upon by the Lorentz body force. Therefore, the electromagnetic stresses are expected to increase with increasing B_{app}.

However, once fully magnetised with $B_{app} = 8$ T, the maximum stresses experienced by the bulk superconductor actually did not increase further with further increases in B_{app}, as shown in Figure 4.13. This is a crucial feature not predicted by analytical solutions based on the Bean model and suggests that as large of an external magnetic field can be used to magnetise a sample without being limited by the mechanical properties of the sample. The observed plateauing of stresses can be understood in terms of the field trapped within the bulk stack. As shown in Figure 4.10, the fields measured in between the GdBCO/Ag samples overlapped for a wide range of B_{app}, implying the same current density distribution, and hence trapped field, must be induced regardless of the magnitude of B_{app}. As a result, identical Lorentz force distribution $F_L = J \times B$ must also exist across the bulk superconductors regardless of the magnitude of B_{app}.

An upper limit to the electromagnetic stresses experienced by a given superconductor sample and operating temperature, as the results have shown, was in fact first suggested by Johansen, who recognised the magnetostriction of a superconductor would reach a plateau at high fields if $J_c \propto 1/B$ [68]. The present study confirms this experimentally and further verification has been obtained from numerical simulations of a bulk stack with a trapped field of around 6.9 T when magnetised with various $B_{app} = 4$ T, 8 T, 12 T and 16 T. The results are shown in Figure 4.14, which also shows a limit on the maximum hoop stress that a sample can experience during FCM that is fundamentally linked to its trapped field capability.
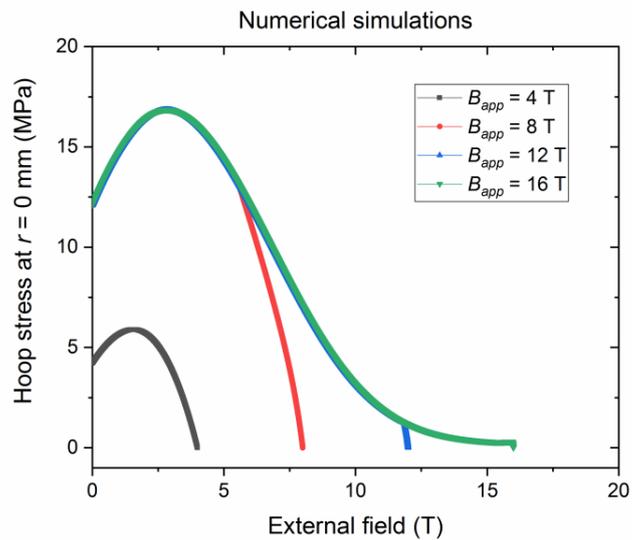
Figure 4.14. Numerical simulations of the hoop stress experienced at the centre of a two-sample stack during magnetisation with different applied fields. The $J_c(B, T)$ implemented is shown in Figure 4.4.

4.4.4. Comparison between experimental and numerical simulation results

The trapped fields were analysed initially to ensure the current density distributions could be reproduced with the models. Figure 4.15 shows a comparison of the simulated trapped fields and the experimental results. Assuming the $J_c(B)$ characteristic shown in Figure 4.4 applies to the entire bulk superconductor, the homogeneous model was able to predict accurately the trapped field at the centre of the stack, at $r = 0$ mm, given that 6.9 T was measured experimentally. However, the simulated trapped field at $r = 10$ mm was 4.6 T, differing significantly from the value of 2.7 T measured experimentally.

The next step in the investigation was to utilise the various $J_c(B)$ behaviour determined experimentally, i.e. inputting directly the $J_c(B)$ characteristics from Figure 4.6(a) into the inhomogeneous model as a function of radial position. This is plotted as the Inhomogeneous case B in Figure 4.15. Only data measured from the top surface of the sample was utilised to minimise computing time and since the strain gauges would have been attached to the top surface. However, the resultant trapped fields were not satisfactory either, with significant discrepancy observed in the shape of the field profiles as the external field was ramped down.

The disagreement is likely due to the invalid assumption that the $J_c(B)$ behaviour in planes further into the sample were aligned with the measurement plane, which is clearly not true based on the $J_c(B)$ curves shown in Figure 4.6.

In an attempt to achieve closer agreement without requiring the complete spatial distribution of $J_c(B)$, a variation in $J_c(0\,\text{T})$ with radial position was applied to the $J_c(B, T)$ data as a numerical factor instead, as the $J_c(B, T)$ used in the homogeneous model was scaled using a constant that varied radially according to the experimental data. This approach is the example depicted in Figure 4.8. This yielded much closer agreement, as shown by the Inhomogeneous case A in Figure 4.15.

Figure 4.16 compares the experimental and modelled results for the electromagnetic hoop strains that develop at different points on the sample with an 8 T applied field. It can be seen that incorporating the inhomogeneous $J_c(B)$ leads to the slight plateauing of strains towards the end of FCM, displaying better qualitative agreement with experiment. The discrepancies in magnitude in the inhomogeneous case may simply be associated with the exact values of Young's modulus used in the model instead of the trend in this parameter with position, since a material that is stiffer overall will exhibit less strain when subject to the Lorentz force.

Figure 4.17 compares the experimental and modelled results for the electromagnetic radial strains that develop at different points on the sample with an 8 T applied field. The inhomogeneous $J_c(B)$ results in significantly more compressive strains in the middle sector of the bulk superconductor, i.e. at $r = 7.5$ mm and 12.5 mm. Additionally, the strains measured at $r = 17.5$ mm also displayed similar evolution as the experimental strains. As is the case with the hoop strains, the inhomogeneous case shows closer qualitative agreement with the experimental results than the homogeneous case, although strains at $r = 2.5$ mm were still significantly different.

For reference, Figure 4.18 shows the modelled hoop strains for the inhomogeneous case with direct input of the experimental $J_c(B)$ characteristics, corresponding to Inhomogeneous case B in Figure 4.15. It can be seen even more pronounced plateauing of the hoop strains could be achieved this way, resembling the experimental results closely. However, it should be noted that the radial strains in this case showed significant differences. As a result, it is likely that a combination of the two inhomogeneous cases discussed may be required to reproduce the experimental results more closely.
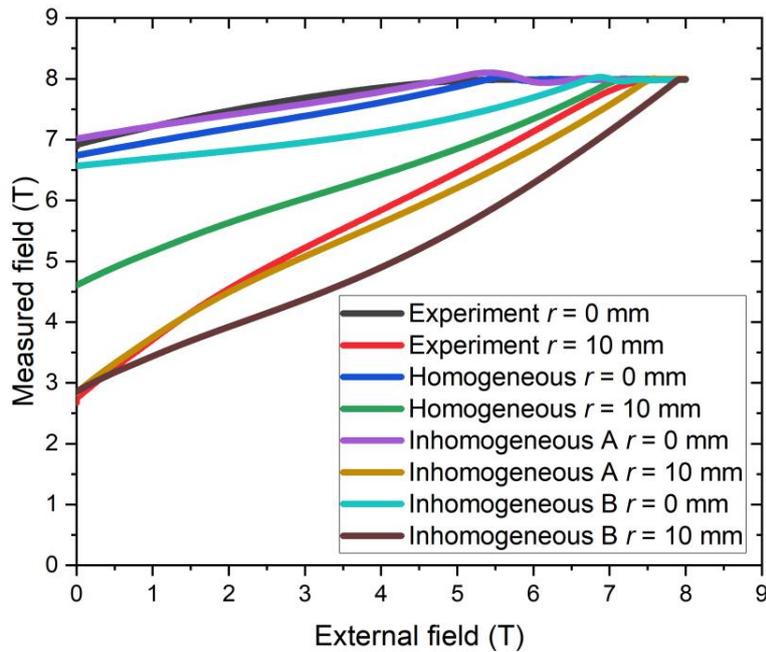
Figure 4.15. Comparison of the experimental and simulation results for the field measured at $r = 0$ mm and $r = 10$ mm in the single grain bulk stack during ramp down of the external field from 8 T. The trapped field for each case can be determined at the end of the ramp when the external field reaches 0 T. $J_c(B, T)$ used in these numerical models can be found in Figure 4.4, Figure 4.5 and Figure 4.6.
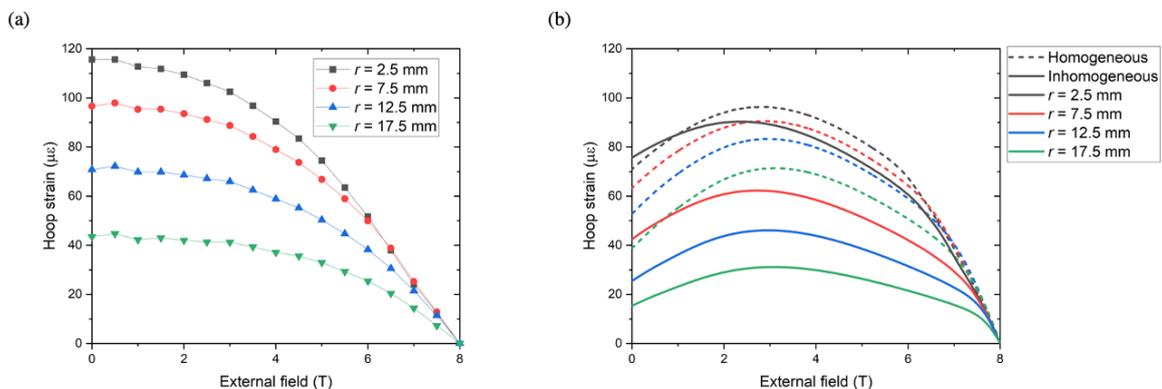
Figure 4.16. Comparison of the (a) experimental and (b) simulation results for the electromagnetic hoop strains at different radial positions during ramp down of the external field from 8 T.
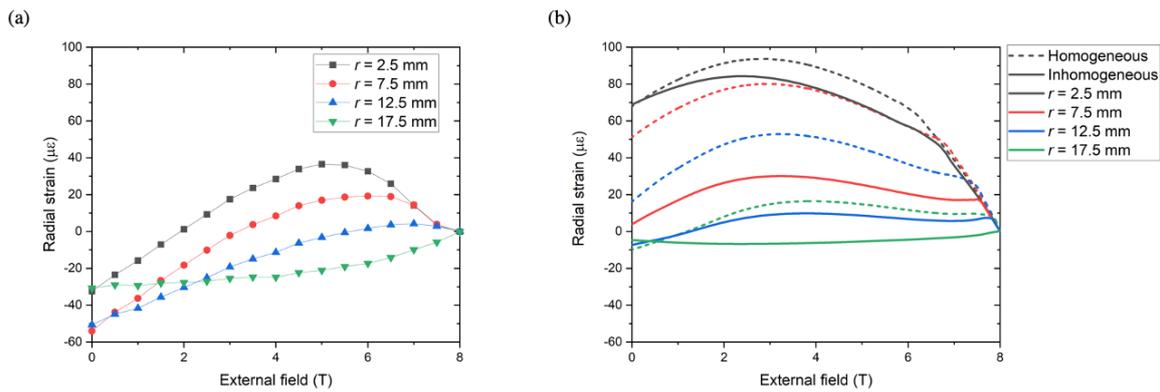
Figure 4.17. Comparison of the (a) experimental and (b) simulation results for the electromagnetic radial strains at different radial positions during ramp down of the external field from 8 T.
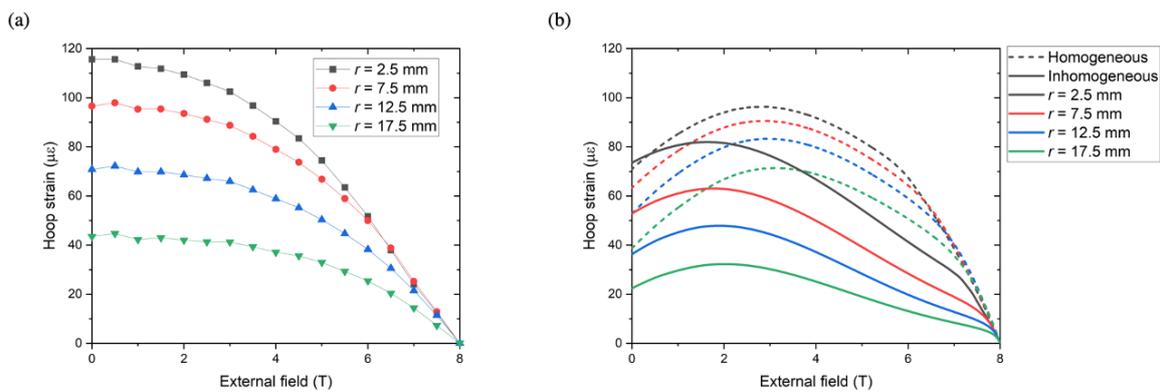
Figure 4.18. Comparison of the (a) experimental and (b) simulation results for the electromagnetic hoop strains at different radial positions during ramp down of the external field from 8 T.

The plateauing of the hoop strains experimentally, which is a fairly significant feature of the experimental results from the present study, may be understood physically by considering the local Lorentz force/pinning force $F_L = J_c \times B$. F_L is expected to vary according to the local $J_c(B)$ and the local field B experienced by each part of the superconductor sample during FCM.

If the peak of the local Lorentz force, $J_c \times B$, is not exceeded at every point in the bulk superconductor as the external field is ramped down, magnetostriction of the sample will rise monotonically as $J_c \times B$ across the entire sample rises with decreasing field. The spatial variation in $J_c(B)$ shown in Figure 4.5 and Figure 4.6 support this argument, where the peak of the fishtail shifts gradually towards $\mu_0 H = 0$ T as r increases, i.e. towards the edge of the sample. This means it becomes increasingly more difficult to cross the peak in the $J_c \times B$ product towards the edge of the sample.

Despite the discrepancies shown in the present study, it should be noted that Latka *et al.* [117] observed very similar behaviour in their experimental study, specifically the compressive nature of the radial strains during FCM, in measuring the pinning-induced strains in an YBCO disc using fibre Bragg gratings. This gives a degree of confidence to the results presented in this chapter as FBG is an entirely different, but complementing, measurement technique.

Lastly, another method of recreating the realistic $J_c(B)$ of a single-grain GdBCO/Ag in the numerical model, suggested by Dr Mark Ainslie, could be to reverse-engineer a global $J_c(B)$ to match the trapped field profile observed experimentally between the two-sample stack. This $J_c(B)$ could subsequently be used to predict the electromagnetic strains using the established modelling framework.

To conclude, there are a number of possible explanations for the remaining discrepancies between the experimental and simulation results. Firstly, simplifications were used to speed up the modelling time and the spatial distributions of $J_c(B)$ and E are simply incomplete. Secondly, the effects of geometry may be significant for the strain gauges attached at $r = 2.5$ mm. Due to the cylindrical geometry of the GdBCO/Ag samples, a strain gauge attached radially near the centre may be severely affected by the perpendicular hoop strain. This would explain why strains from the $r = 7.5$ mm, 12.5 mm and 17.5 mm gauges showed significantly closer agreement with the model. Thirdly, other material properties may also need to be considered for a more comprehensive analysis. For instance, the spatial variation of Ag in large GdBCO/Ag single grains could play a significant role in altering the local Young's modulus, Poisson's ratio or thermal expansion coefficient (which could lead to significant residual stresses when cooling the samples).

4.5.   Conclusions

In this study, the hoop and radial strains at four positions along the radius of a 40 mm diameter GdBCO/Ag bulk superconductor were measured during field cooled magnetisation (FCM). The sample was part of a two-sample stack that trapped 6.9 T at 64 K, where the stack structure was implemented to resemble arrangements used for record-setting trapped magnetic fields and to assist with the determination of strain across the centre of a long superconductor. The stack was subjected to FCM at 64 K with applied fields ranging from 5 T to 9.6 T, and the flux-pinning-induced strains were measured continuously as supercurrents were established and a magnetic field was trapped. Hoop and radial stresses were also calculated from the measured strains to illustrate their evolution through the field-cooling and field-trapping process. The significant contributions of this study are summarised below.

Firstly, by measuring the hoop and radial strains simultaneously, the biaxial stresses that develop within the *ab*-plane of a bulk superconductor as a result of the radially outward Lorentz force were determined. This study is one of the first to consider stress and strain components in both directions. The hoop stress measured at the end of the FCM process also showed good agreement with the analytical solutions presented by Ren *et al.*, while both the hoop and radial stress profiles at the end of FCM showed good qualitative agreement.

Secondly, by magnetising the single-grain bulk stack with an external applied field significantly greater than the maximum trapped field achievable by the stack, we showed that the maximum stress experienced by the sample during and after FCM did not increase with further increases in the magnitude of the applied field. This behaviour was not predicted by modelling based on the Bean model. This is significant since an upper limit in stress that depends only on the sample and operating temperature would benefit high-field magnetisation of these trapped field magnets significantly and would make it possible to predict the failure conditions of these magnets.

Thirdly, two FEM models were constructed in order to reproduce the experimental results, namely a homogeneous case and an inhomogeneous case. By incorporating the spatial distributions of the critical current density and Young's modulus, both of which were determined empirically, the inhomogeneous model achieved better agreement with the experimentally measured trapped fields and strains. This shows that in order to model large single grains accurately, the inhomogeneity of the relevant material properties should also be

considered. (RE)BCO single grain bulk superconductors inevitably possess microstructure that varies spatially due to the kinematics of the melt growth process, and one may expect this inhomogeneity to become more prominent with an increase in the size of the single grain.

Chapter 5

Artificial holes for improving the intrinsic strength of YBCO bulk superconductors

Porosity, arising from oxygen produced during melt processing and subsequently trapped during solidification, has a detrimental effect on the mechanical and superconducting properties of RE-Ba-Cu-O bulk superconductors. A simple method to reduce the porosity of single-grain samples is to fabricate them in a thin-wall geometry, where a network of artificial columnar holes is patterned into the preforms to reduce the oxygen diffusion path and to allow gas to escape at elevated temperature during processing.

In this chapter, the tensile strength of thin-walled YBCO bulk superconductors provided by CAN SUPERCONDUCTORS was determined using the Brazilian test and the porosity across a typical sample was analysed. The thin-walled samples showed lower porosity and an average tensile strength that was up to 93 % higher compared to standard YBCO discs fabricated under identical conditions. The enhancement in mechanical properties was validated using high-field magnetisation experiments, where the standard YBCO sample failed when it was field cooled magnetised with 10 T at 35 K, suffering permanent damage, as evident from the field profile. On the other hand, the thin-wall YBCO sample survived all magnetisation cycles, including a magnetisation field of 11.5 T at 35 K, demonstrating that this sample was able to survive considerably higher magnetisation fields, and therefore electromagnetic stresses. In the process, the thin-wall sample trapped successfully a surface field of 8.8 T at 30 K when magnetised with 11 T, demonstrating the practical level of field that can be generated by engineering the samples in this form.

This study demonstrates, firstly, thin-wall YBCO discs can be used to make better trapped field magnets compared to standard YBCO discs due to a higher tensile strength intrinsically and the potential for improved cooling. Secondly, the accuracy of the Brazilian test in predicting

the field at which bulk superconductors are expected to fail during magnetisation as a result of the Lorentz force has been validated.

5.1. Introduction

5.1.1. Thin-wall bulk superconductors

Significant porosity can often be observed in large RE-Ba-Cu-O [or (RE)BCO] single grains as a result of residual inert gas and pockets of oxygen gas being trapped in the viscous melt during melt processing and solidification. The oxygen gas originates from the peritectic decomposition reaction and thus is an inevitable by-product of the melt process. Porosity is undesirable due to the well-established detrimental effects it has on the mechanical properties of (RE)BCO bulk superconductors [143] (and brittle materials in general) as well as their superconducting properties. Furthermore, the number of defects is also expected to increase with increasing domain size. For example, porosity would likely increase with sample size due to a longer oxygen diffusion path. This defect scaling could further limit the trapped field performance of larger single-grain samples.

A variety of melt-processing techniques for the texturing of (RE)BCO bulk superconductors with reduced porosity, and therefore better mechanical properties, have been investigated. These include firstly, infiltration and growth, which can generate denser, more homogeneous microstructure than the traditional top seeded melt growth [100]. Secondly, processing in a controlled atmosphere other than air, since entrapment of gas and sample porosity have been observed to increase with an increase in partial pressure of the inert gas during melting [144]. For example, Sakai *et al.* reported an increase in tensile strength from 37.4 MPa to 48.0 MPa by melting the precursors in 100 % oxygen followed by growth in an argon atmosphere, although the superconducting properties showed degradation as a result of this process [145]–[147]. Thirdly, it is also possible to reduce sample porosity with the inclusion of silver particles [86], [148], although issues with chemical compatibility and differences in melting temperatures mean there are only a few viable options when it comes to metallic inclusions. All of the above techniques can be somewhat challenging to achieve, most notably requiring adjustments to well-established melt-processing procedures and heating profiles or requiring furnaces with a controlled atmosphere.

Another established method to reduce the porosity of (RE)BCO bulk superconductors is to fabricate the single grains with an array of artificial columnar holes patterned into the pressed pellets of precursor powder in the so-called thin-wall geometry. The artificial holes, typically each around 1 mm in diameter, decrease the effective wall thickness and provide easier paths for gas to escape during processing. An example of such a thin-wall sample is given in Figure 5.1. In addition to reduced porosity, the artificial holes also increase the specific surface area of the samples, potentially allowing for improved cooling. Improved thermal properties are beneficial as they can help mitigate flux jumps, which occur in part due to the low thermal conductivity of (RE)BCO at low temperature. The use of artificial holes is an easy-to-implement technique as it only requires integrating a simple step into the growth process. Otherwise, the precursors can be subjected to the same heating profile as conventional hole-free samples. Reducing the effective wall thickness could also lead to a more efficient and homogeneous oxygenation of the as-grown single grains as well as a reduced level of oxygenation cracks.

Ideas of patterning YBCO were explored in the early 2000s as it became clear melt-processed (RE)BCO samples can be engineered, mechanically and thermally, to achieve trapped fields as high as 17 T [7]. Reddy *et al.* reported the fabrication of YBCO bulk samples with pre-defined 3D interconnected channels that can be filled with resins or alloys for reinforcement post-growth [149]. They achieved this by casting a water-based Y-211 slurry into a mold containing a pre-defined 3D wax structure to embed the channel structures into the Y-211 pre-forms. This was followed by dewaxing and growing the pre-forms into single domains by infiltration and growth. Reddy *et al.* and Noudem *et al.* also demonstrated the application of this technique to fabricate single-domain Y-123 foams containing large, open porous structures [150], [151].

Noudem *et al.* reported the growth of "perforated" YBCO samples textured with artificially patterned holes parallel to the *c*-axis to facilitate oxygenation and decrease crack formation [152]. Regularly spaced holes up to 2 mm in diameter were drilled into the sintered samples prior to melt processing. Their goal was to address the issue of hot spot formation in fault current limiter applications. The results showed, firstly, the porosity was reduced, exhibiting compact, crack-free regions around the holes; secondly, the holes did not hinder domain growth; and thirdly, J_c was improved at a number of locations compared to the hole-free samples.

Chaud *et al.* reported bulk samples with a dense network of holes such that the effective thickness of the samples that were several centimetres in diameter could be considered to be less than 1.5 mm [138]. They confirmed the growth of a thin-wall single domain up to 50 mm in diameter without significant grain misorientation, although they did observe the presence of minor surface defects as a result of growth fronts interacting with the holes. Two methods of forming the holes were described in their study, namely the drilling of sintered pellets and the pressing of holes directly into the pre-forms with dies containing long, stainless-steel needles. Their study showed no visible pores in samples grown on these drilled or pressed pellets, which was typical of the thin-wall geometry with a hole spacing below 4 mm. This was shown visually with a direct comparison of the cross section of a drilled and a plain sample [153], showing a dramatic porosity reduction in the drilled pellet. Remarkably, Chaud *et al.* reported that the drilled thin-wall sample exhibited a trapped field (0.532 T) that was around 40 % higher than the hole-free sample (0.375 T) despite an 18 % reduction in superconducting volume due to the holes.

Another advantage of the thin-wall geometry lies in the potential for further post-melt-processing treatments and enhancement in performance of a thin-wall bulk magnet system, which was discussed by Kenfaui *et al.* [154]. The trapped field performance of a 16 mm diameter thin-wall YBCO sample was increased from 5.2 T, when the sample was unreinforced, to 6.34 T, when the sample was reinforced through Al wire inserts and impregnated in resin loaded with Al particles. This study demonstrates heating within (RE)BCO samples during magnetisation, the impact on trapped field and the scope for further improvement.

More recently, YBCO bulk superconductors processed with artificial holes have also gained commercial attention for potential use as superconducting bearings. Mechanical [155] and levitation properties [156] were measured for batches of samples manufactured by CAN SUPERCONDUCTORS. The study by Hlásek *et al.* reported Young's moduli of 32 ± 3 GPa and 47 ± 2 GPa at 295 K, as well as 52 ± 5 GPa and 76 ± 3 GPa at 77 K, for the standard and thin-wall samples [155], respectively. The difference between the sample types is most likely due to the denser microstructure that forms in thin-wall samples.
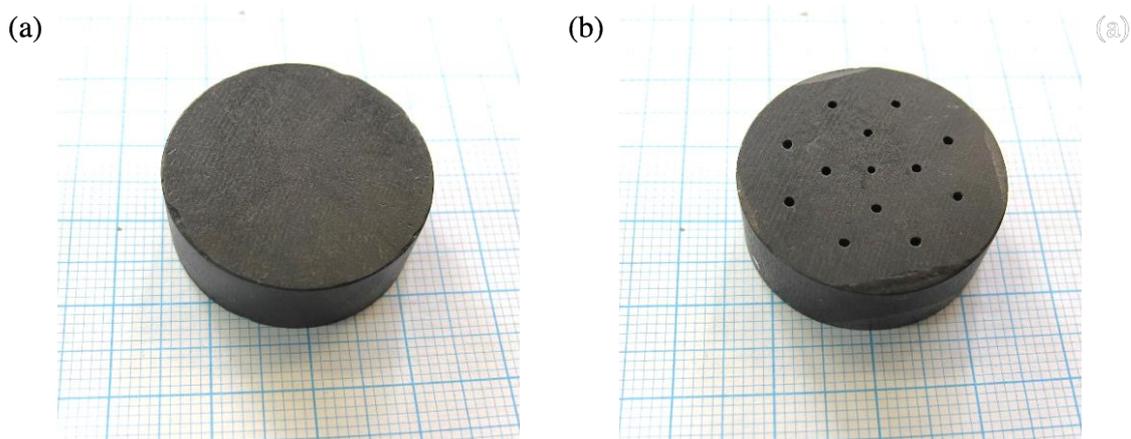
Figure 5.1. (a) A standard YBCO disc 27 mm in diameter. (b) A thin-wall YBCO disc 27 mm in diameter. Small columnar holes around 1 mm in diameter are visible on the surface of the bulk superconductor. Both samples were produced by CAN SUPERCONDUCTORS.

5.1.2.   Motivation for the proposed study

This chapter presents a comprehensive characterisation of the mechanical strength of 27 mm diameter, thin-wall YBCO bulk superconductors, which was then compared to standard YBCO of the same size grown under similar conditions. To confirm the mechanical strength indeed has an impact on the peak trapped field performance achievable, the samples were subjected to field-cooled magnetisation at 35 K with gradually increasing applied fields. The purpose of these magnetisation experiments was to fracture the samples deliberately under the Lorentz force and determine whether the thin-wall YBCO sample could survive more extreme field conditions due to an improved tensile strength (and potentially improved thermal properties). This is a useful experimental study since most methods of determining the mechanical properties of bulk superconductors involve mechanical tests on small unmagnetised specimens cut from a large single grain. By magnetising whole superconductor discs until failure, we can determine directly the limitations of these materials. A study utilising both mechanical and magnetisation tests on a batch of nominally identical samples could also help us assess the accuracy of the strength values obtained using the Brazilian test, which, in theory, should be more accurate than the tensile test or the bend test due to the significantly larger specimen volume.

5.2. Experimental details

5.2.1. Fabrication of thin-wall YBCO

The single-grain YBCO samples used in this study were fabricated and supplied by CAN SUPERCONDUCTORS. The sample fabrication procedure is described in detail in [155]. In summary, precursor powder with stoichiometric composition of $Y_{1.8}Ba_{2.4}Cu_{3.4}O_x + 0.5$ wt% CeO_2 was uniaxially pressed into pellets containing columnar holes using a "spiked die", as shown in Figure 5.2. The pellets were then processed via top seeded melt growth (TSMG) in air under isothermal conditions with commercial thin films of Nd-123 on MgO (2 mm × 2 mm) as seed crystals to produce YBCO single grains. To facilitate the tetragonal to orthorhombic transition, the samples were then annealed in flowing oxygen between 300 °C and 450 °C for 150 h. Finally, the YBCO discs were all machined to a diameter of 27 mm and thickness of 10 mm for characterisation.
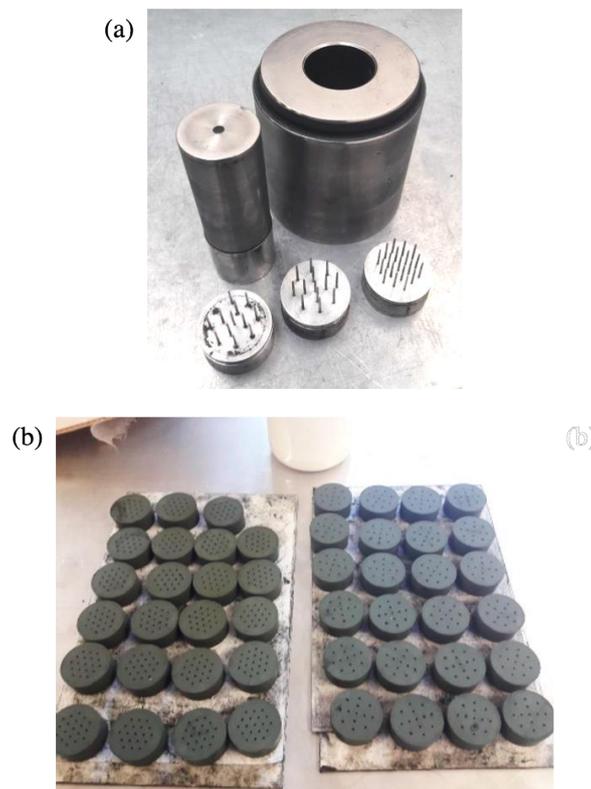
Figure 5.2. (a) A die and spiked punches used to produce columnar holes in pellets of pressed precursor powder [157]. (b) After uniaxial pressing, the pellets underwent melt processing, as usual.

A reference batch of standard YBCO discs without the artificial holes was also prepared under similar conditions for comparison.

5.2.2. Mechanical and microstructural characterisation

As discussed in previous chapters, a number of test techniques are available for determining the mechanical strength of bulk superconductors. The Brazilian test, described in detail in Chapter 3, was selected for this study to determine the strength and mechanical reliability of the thin-wall YBCO bulk superconductor produced commercially. The benefits of using the Brazilian test for this particular study include firstly, minimal sample preparation is required, which minimises the introduction of defects through cutting and polishing; secondly, a strength value representative of the whole bulk superconductor can be acquired, which would ideally correlate more closely with the field at which mechanical failure is expected during magnetisation compared to results from other test techniques; thirdly, a direct strength comparison is possible between different sample types; and, lastly, the bulk-to-bulk variation in strength can also be determined, which would make it apparent if the strength scatter is improved by the array of artificial holes.

For the Brazilian test, thin-wall samples were compressed along their growth sector boundaries, as shown in Figure 5.3. The crosshead speed was fixed at 0.03 mm/min. The tensile strength was determined from the failure load via Equation (5.1), where σ is the indirect tensile strength, P is the load at failure, and D and t are the sample diameter and thickness, respectively.

$$\sigma_{indirect} = \frac{2P}{\pi D t} \qquad (5.1)$$

Optical micrographs were taken along the cross section of a typical thin-wall sample at halfway along the thickness/height to determine the influence of the artificial holes on the porosity at various locations. ImageJ software was used subsequently to quantify the porosity as an area fraction, following the methods described in Chapter 3. The above procedures were then repeated for standard YBCO discs of the same diameter and thickness.
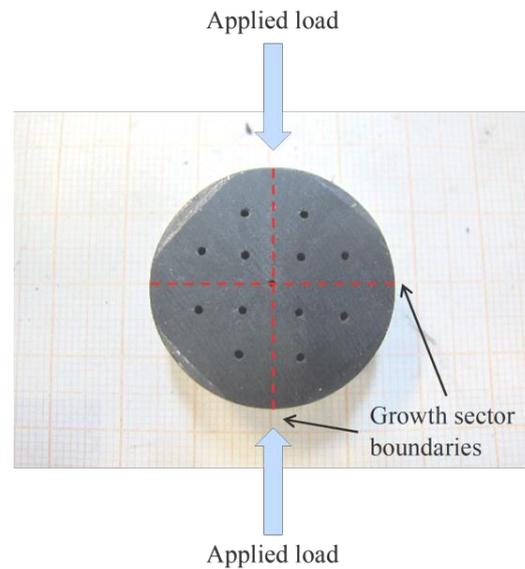
Figure 5.3. Thin-wall YBCO for Brazilian testing. The growth sector boundaries are marked, and the direction of the applied load is illustrated.

5.2.3.   Trapped field measurements

The YBCO bulk superconductors were field cooled magnetised in a 12 T superconducting magnet. The samples were fitted loosely in a copper sample holder using Apiezon N vacuum grease to ensure good thermal contact to the holder, Cernox® sensor and heater but with minimal mechanical reinforcement. The experimental set-up is shown in Figure 5.4(a). Field cooling involved applying an external field between 7 T and 11.5 T to the sample with the sample temperature held at 100 K. Once the field was reached, the sample was cooled to the measurement temperature of 35 K. The external field was removed slowly at a rate of 0.04 – 0.18 T/min when the temperature had stabilised (0.180 T/min from 0 T to 4.3 T, 0.128 T/min from 4.3 T to 8.6 T, 0.077 T/min from 8.6 T to 11.1 T and 0.040 T/min from 11.1 T to 11.5 T due to the magnet limits), as shown in Figure 5.4(b), to establish a trapped field in the sample. The sample was then de-magnetised by warming to 100 K before the next set of measurements were made at a slightly higher applied field. The process was repeated with an increasingly higher magnetisation field to determine the point at which the electromagnetic stresses due to the Lorentz force would exceed the tensile strength of the superconductor.

A linear array of Hall sensors (Lakeshore HGT-2101) was placed on the surface of the sample to measure the field continuously at multiple points along the sample diameter as the external field was ramped down.

The magnetisation experiments described above were carried out for thin-wall YBCO and standard YBCO samples with similar surface trapped fields at 77 K. The thin-wall YBCO sample exhibited a trapped field of 0.84 T (measured using the hand-held gaussmeter) while the standard YBCO sample exhibited a trapped field of 0.81 T, both of which are typical of samples of this size.
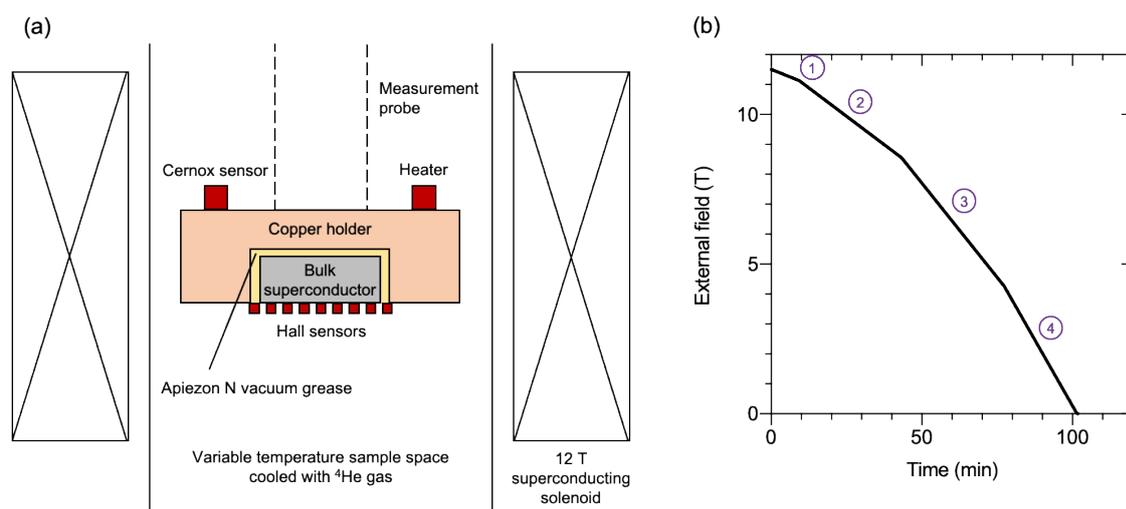
Figure 5.4. (a) Schematic illustration of the magnetisation set-up used. (b) Ramp rates used for the different field ranges: 1. 0.040 T/min. 2. 0.077 T/min. 3. 0.128 T/min. 4. 0.180 T/min. The rates were set based on the magnet limits and were fixed for each field range regardless of the starting field.

5.3. Results and discussion

5.3.1. Tensile strength of thin-wall YBCO

Figure 5.5 shows the room temperature tensile strengths σ measured indirectly using the Brazilian test for the various sample types, which are summarised in Table 5.1. 12 standard YBCO samples were measured. 8 thin-wall samples were measured with open holes while another 8 were measured after their holes were filled using Stycast® 2850 FT (mixed with 23 LV catalyst) to minimise stress concentration caused by the artificial columns. Stycast has a relatively low Young's modulus (< 10 GPa) compared to YBCO bulk material, so the main purpose of the resin impregnation was to minimise stress concentration caused by the artificial holes and to achieve a fair comparison of the strength of the constituent YBCO material.

In theory, stiffer and stronger reinforcement materials could have been chosen to further increase the measured mechanical strength of the filled thin-wall samples, which was the case in the magnetisation experiments described in Section 5.3.3.

The average σ for the standard YBCO was 14.1 MPa. The average σ for the unfilled thin-wall YBCO was 22.9 MPa, which was a 62 % improvement over the standard sample. This showed that the Y-123 material still exhibited significantly better mechanical strength even with the stress concentration of the unfilled holes. The enhancement was confirmed when the thin-wall YBCO samples were filled with Stycast epoxy resin. This resulted in an average σ of 27.3 MPa, demonstrating a 93 % improvement over the standard YBCO.

Additionally, based on the strength data available, the strength scatter also appears to be reduced by introducing the thin-wall geometry. The increase in Weibull modulus from 6.9 to 11.9, going from the standard to the filled thin-wall YBCO samples, suggests the narrowing of the defect size distribution, due most likely to the elimination of the largest pores as a result of the shorter diffusion paths. This, ultimately, has led to higher and more consistent/reliable failure strengths.
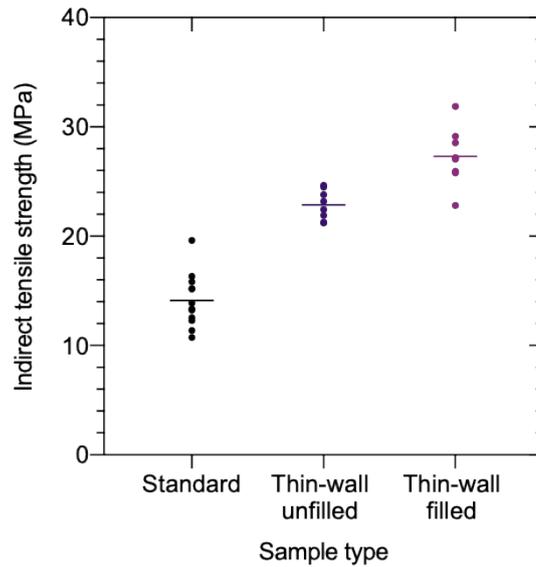
Figure 5.5. Room temperature tensile strength measured indirectly via the Brazilian test for each type of sample.

Table 5.1. Average tensile strength for each sample type. The Weibull modulus and associated characteristic strength have also been calculated for each set of data.

Sample type	Average strength (MPa)	Minimum strength (MPa)	Weibull modulus	Characteristic strength (MPa)
Standard	14.1	10.7	6.9	15.1
Thin-wall unfilled	22.9	21.2	19.1	23.5
Thin-wall filled	27.3	22.8	11.9	28.4

5.3.2. Porosity analysis

Optical micrographs of typical standard and thin-wall YBCO samples are shown in Figure 5.6, where it is clear porosity is significantly reduced in the vicinity of the artificial holes. A very low porosity can be achieved with closely spaced holes at the centre of the sample. Porosity

analysis on the first set of micrographs is shown in Figure 5.7, where the additional standard YBCO sample from Figure 5.6 was also analysed.

While porosity does vary slightly from sample to sample, as evident from the two standard YBCO discs, it appears the porosity of the thin-wall YBCO does not exceed that of the standard YBCO at any position and is actually suppressed considerably in the vicinity of the artificial columns. Therefore, with carefully chosen hole patterns, the porosity at the centre of the sample, which is the region that experiences peak tensile stress during and after magnetisation, can be engineered to be very low.
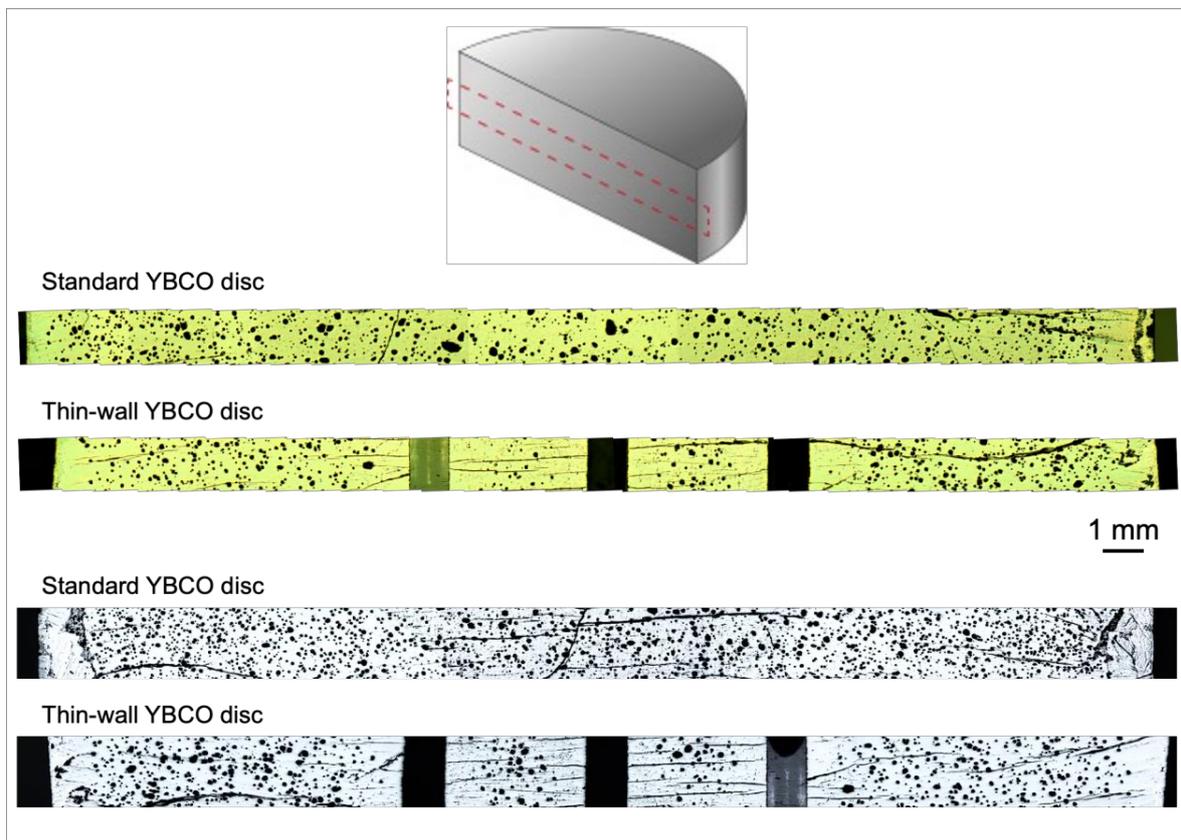
Figure 5.6. Optical micrographs taken across the centre of standard YBCO discs and thin-wall YBCO discs. Pores/voids are clearly visible in the cross sections. The three vertical columns towards the centre of the thin-wall samples are the artificial holes introduced prior to melt processing.
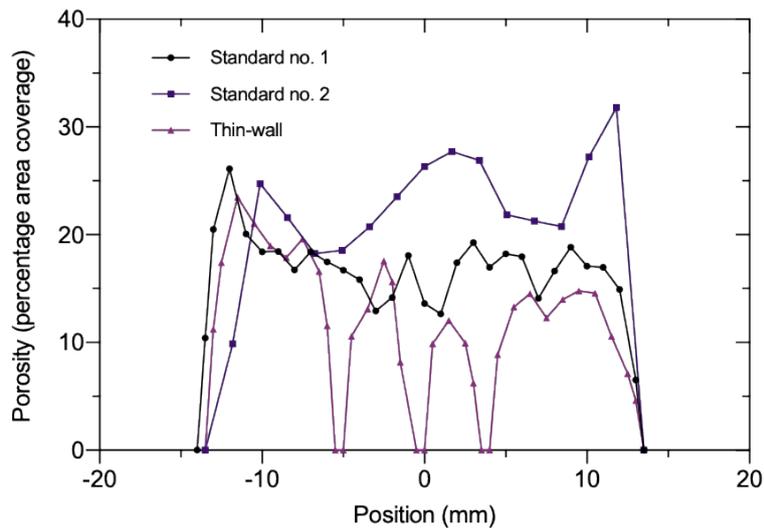
Figure 5.7. The estimated porosity as a function of radial position in the YBCO samples.

5.3.3.   Trapped field performance of thin-wall YBCO

In this section, high-field magnetisation experiments were performed to deliberately fracture the samples in order to verify the mechanical strengths reported in Section 5.3.1, where the Brazilian test showed the thin-wall samples were at least 62 % stronger than the standard samples. The strength enhancement was increased to 93 % when the artificial holes were filled with Stycast.

Samples for the magnetisation experiments were chosen based on their ability to trap similar fields at 77 K and possessing identical sample dimensions (diameter of 27 mm and thickness of 10 mm). One sample of each type was subjected to the field-cooled magnetisation process.

Figure 5.8(a) shows the trapped field performance on the surface of the standard YBCO disc when magnetised with increasing applied field at various temperatures. It is important to note that the data points correspond to trapped fields measured following complete, independent magnetisation cycles, i.e. the sample was de-magnetised completely by warming to 100 K between each data point. Once the sample survived a cycle, either the applied field was increased, or the target temperature was reduced, between the cycles.
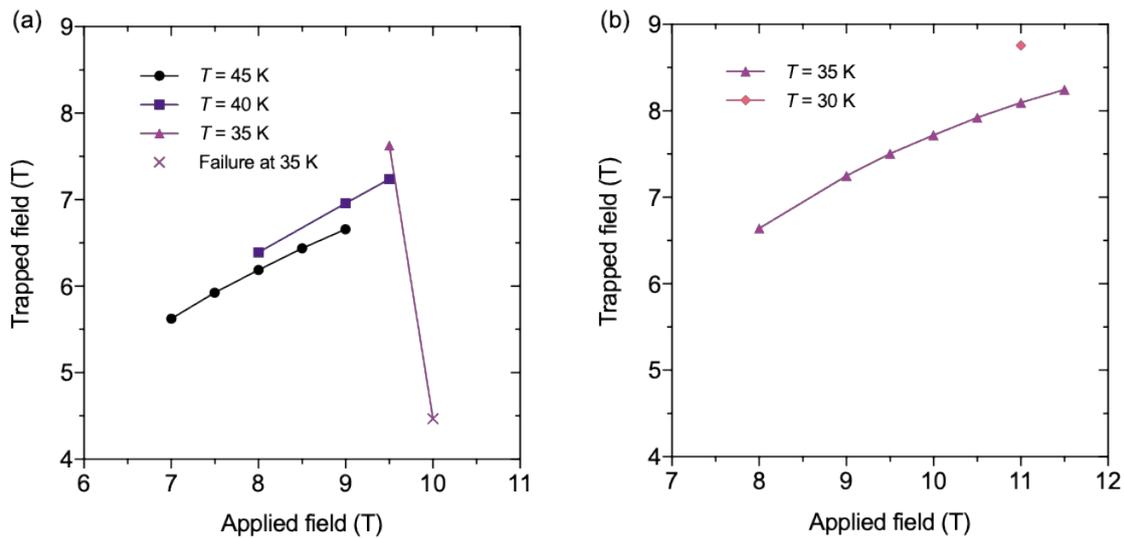
Figure 5.8. (a) Field trapped by the 27 mm diameter standard YBCO sample as a function of applied field and temperature. The sample fractured when it was magnetised with 10 T at 35 K (b) Field trapped by the 27 mm diameter thin-wall YBCO sample as a function of applied field and temperature. No failure was observed in this sample.

Field cooling was first carried out at 45 K with an applied field of 7 T. It can be seen the YBCO disc was able to trap up to 6.66 T at 45 K with an applied field of 9 T. The increase in trapped field with increasing applied field at 45 K suggests the sample was not fully magnetised during field cooling, i.e. it was not fully penetrated by magnetic flux.

The target temperature was reduced to 40 K in order to increase the J_c, the trapped field attainable and, most importantly, the electromagnetic stresses within the sample. At 40 K, the YBCO disc was able to trap up to 7.24 T with an applied field of 9.5 T and, again, survived the range of magnetisation cycles.

The target temperature was further reduced to 35 K. At 35 K, the standard sample survived the initial magnetisation with an applied field of 9.5 T, eventually trapping 7.63 T. However, when the applied field was increased to 10 T, the sample suffered either a crack or a flux jump, which appeared as an abrupt drop in the field measured followed by a significant rise in the sample temperature. Further examination showed the sample indeed cracked, as shown in Figure 5.9. The peak trapped field has dropped considerably compared to the value measured prior to the series of magnetisation cycles described, and significant asymmetry was observed.
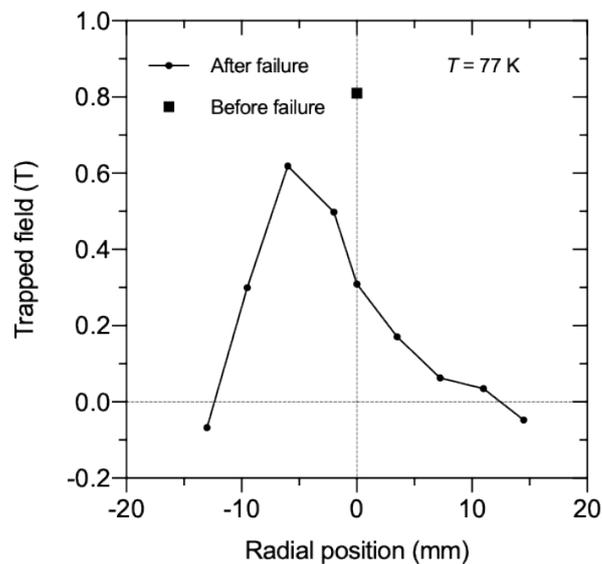
Figure 5.9. Trapped field values measured on the standard YBCO sample after field cooling at 77 K, before and after failure during high-field magnetisation at 35 K.

For consistency, the thin-wall YBCO disc was also subjected to field cooled magnetisation at 35 K. The sample used is shown in Figure 5.10. The artificial holes were filled with solid core copper wires and solder in order to minimise stress concentration and to assist cooling. This demonstrates the versatility of thin-wall samples and means potential improvements in the trapped field capability may be a result of enhancements made to both the mechanical and thermal properties of the sample.

As shown in Figure 5.8(b), the thin-wall sample was field-cooled with 8 T at 35 K initially, after which the applied field was increased incrementally. A peak trapped field of 7.51 T in the thin-wall YBCO sample, achieved with an applied field of 9.5 T, was similar to that observed in the standard YBCO, which trapped 7.63 T with the same applied field and at the same temperature. This suggests the magnetisation experiments were a fair comparison and the electromagnetic stresses being generated within the two samples were similar in magnitude.

Figure 5.8(b) shows the thin-wall YBCO sample was able to withstand up to 11.5 T in applied field at 35 K without failing, while the standard YBCO failed at 10 T.
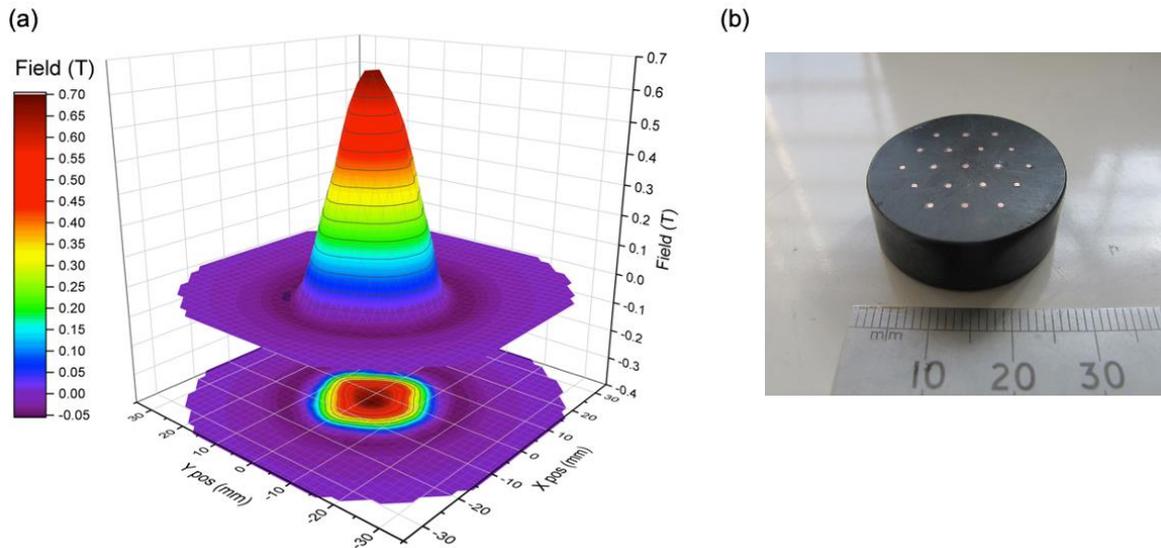
Figure 5.10. (a) Trapped field profile, measured at 77 K, of the thin-wall YBCO sample used in the field cooling experiments. It can be seen that the presence of a large number of artificial holes, 19 holes each around 0.8 – 1.0 mm in diameter (2.6 % of the cross-sectional area), did not affect the magnitude of the peak field. The peak field was consistent with standard YBCO samples and the field profile was sharp and conical. (b) The thin-wall sample used in the magnetisation experiments. The artificial holes were filled with copper wires and solder to minimise stress concentration and improve cooling during magnetisation.

To push the thin-wall sample further and to determine the maximum trapped field achievable, field cooling was carried out with an 11 T applied field at 30 K. Reducing the temperature should increase J_c, which, theoretically, should increase the volume of superconductor under peak tensile stress [67]. The thin-wall YBCO sample was also able to survive the increased J_c and trapped a peak surface field of 8.8 T at 30 K immediately after the removal of the external field, as shown in Figure 5.10.

The trapped field results are significant for the following reasons. Firstly, it has been demonstrated the thin-wall YBCO sample could indeed survive more extreme magnetising conditions and larger electromagnetic stresses, which is consistent with observations of the mechanical tests. The presence of the artificial holes enables beneficial post melt processing treatments to further enhance the mechanical and thermal properties of these trapped field magnets which help to resist brittle fracture and/or flux jumps. For instance, improved cooling

and increased heat capacity through embedded copper wires could have contributed to the survival of the thin-wall sample in this study.

Secondly, the thin-wall YBCO sample showed it could form a viable trapped field magnet in the sub-10 T field range as manufactured, since the sample was able to trap successfully 8.8 T at 30 K on its surface without any external ring reinforcement. On the other hand, the standard YBCO disc could only trap 7.6 T successfully and failed when magnetised with 10 T at 35 K. This could make thin-wall YBCO an attractive option in applications where ring reinforcement may be undesirable, i.e. where sample size is a major constraint. Additionally, the possibility of engineering the thermal properties of this bulk magnet system could be appealing to PFM research.
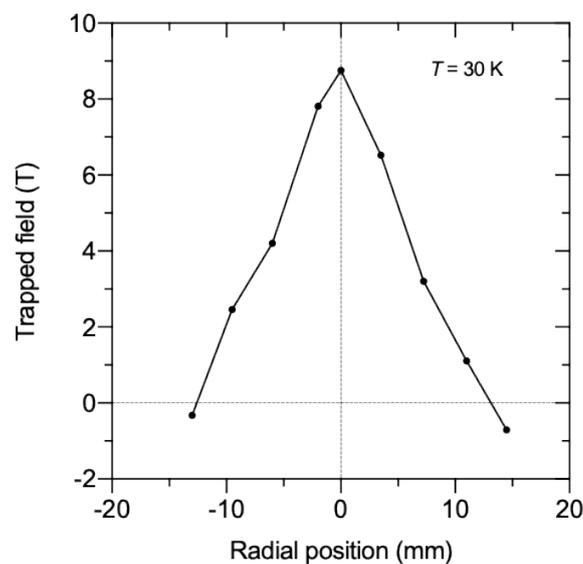
Figure 5.11. Trapped field on the surface of the 27 mm diameter thin-wall YBCO sample when magnetised with 11 T at 30 K. The sample was not reinforced externally.

5.3.4.   Estimate of tensile strength based on maximum trapped field

Using the Bean model [31] and analytical and numerical solutions for the electromagnetic stresses [67], [158], we can estimate the peak tensile hoop stress experienced at the centre of the YBCO bulk superconductor based on the magnetisation results from Section 5.3.3. We

believe each sample was not fully magnetised due to the observed continuous increase in trapped field with increasing applied field used, indicating that the inherent Lorentz force also increased continuously throughout the series of magnetisation cycles.

Tsuchimoto *et al.* analysed numerically two-dimensional stress distributions in bulk superconductors using the finite difference method [158] and following the Bean model. For the aspect ratio used in the present study, where height/radius = 10/13.5 = 0.74, Tsuchimoto *et al.* estimated the maximum hoop stress through the centre of a bulk superconductor with such aspect ratio to be $\sigma \approx 0.3 \times (B_1{}^2/2\mu_0)$, compared to $\sigma = 0.71 \times (B_1{}^2/2\mu_0)$ as is the case of an infinitely long, thin superconductor. B_1 is the maximum trapped field at the centre of the latter. Subsequently, by combining the geometric factor from the study by Tsuchimoto *et al.* [158], the analytical solutions for partial magnetisation by Ren *et al.* [67] and the maximum applied field up to which each sample survived in the present study, the minimum tensile strength of each sample was estimated from $\sigma \approx 0.3 \times (B^2/2\mu_0)$, where σ is the mechanical strength and B is the applied field that the sample could endure.

The results are summarised in Table 5.2, which also shows the tensile strengths obtained for the standard and filled thin-wall samples through the Brazilian test. For the standard YBCO, we can see close agreement between the values determined using the mechanical and magnetisation techniques. This confirms the accuracy of the Brazilian test in providing a strength value representative of the operating limits of the superconductor.

For the thin-wall YBCO sample, on the other hand, the tensile strength was increased by at least 47 % compared to standard YBCO according to the magnetisation results, while the Brazilian test suggested a 93 % improvement. The discrepancy is most likely due to the fact the thin-wall sample did not fail at 11.5 T and could have survived an even higher magnetising field if the magnetisation facility had permitted.

It is also important to note the strengths calculated in Table 5.2 actually represent the stress states at the end of magnetisation and not during magnetisation. The electromagnetic stresses experienced during magnetisation would have been higher [67]. This is also why bulk superconductors tend to fail during magnetisation rather than after the external field has been removed completely. Therefore, the strengths determined in Table 5.2 represent slight underestimates. This, again, is consistent with the mechanical test results on the standard YBCO sample.

Table 5.2. Comparison of the tensile strengths of standard YBCO and thin-wall YBCO samples determined using mechanical and magnetisation techniques. *The thin-wall sample did not fail during magnetisation, and therefore the values shown are not absolute.

Sample type	Tensile strength (MPa) from the Brazilian test	External field survived (T)	Tensile strength (MPa) from magnetisation
Standard	14.1	9.5	10.8
Thin wall	27.3	11.5*	> 15.8*

5.4.   Conclusions

In this chapter, indirect tensile tests were carried out on whole standard and thin-wall YBCO bulk superconductors, which showed the thin-wall samples were at least 62 % stronger than the standard discs due to reduced porosity in the vicinity of the artificial holes. By filling the holes with Stycast, the strength enhancement was increased to 93 %. The enhancement could potentially be increased further, in theory, with a carefully designed hole pattern/spacing and effective mechanical and/or thermal reinforcement materials. An important next step in this investigation would be to determine the optimum number of holes for maximising strength without compromising on trapped field.

The standard and thin-wall samples were subsequently subjected to high-field magnetisation to confirm the improved reliability of thin-wall YBCO. The standard hole-free sample failed when magnetised with 10 T at 35 K, whereas the thin-wall sample survived all magnetisation cycles, including a magnetisation field of 11.5 T at 35 K. In the process, the thin-wall YBCO achieved successfully a trapped field of 8.8 T at 30 K without any external ring reinforcement. These magnetisation results are in close agreement with estimates of the failure fields based on the Brazilian test, implying that the Brazilian test is a useful technique for accurately determining the limitations of (RE)BCO single-grain bulk superconductors.

Chapter 6

Composite bulk superconductor stacks for reliable trapped fields exceeding 16 T

Trapped fields of over 20 T are achievable in state-of-the-art single-grain RE-Ba-Cu-O [or (RE)BCO] bulk superconductors. The major obstacles to realising such performance are firstly, the large tensile stresses that develop during magnetisation as a result of the Lorentz force, and secondly, thermal instabilities that develop as a result of flux movement during removal of the external magnetising field.

In this chapter, the fabrication of disc-shaped GdBCO/Ag bulk superconductor composites reinforced with stainless steel laminations and shrink-fit stainless-steel rings is described. These procedures were aimed at reducing the tensile stress experienced by the bulk stack and at resisting flux avalanches during magnetisation. The sample stacks were magnetised and measured in the variable temperature cryostat of an 18 T superconducting magnet. In the first composite stack fabricated, magnetic fields ~ 17 T were successfully trapped in sequential sets of measurements. A field of 16.8 T was achieved at 26 K in the first magnetisation cycle and 17.6 T was achieved at 22.5 K in the following cycle. Two further composite stacks that were produced by the Bulk Superconductivity Group also demonstrated trapped fields of around 16 T in their initial cycles, signifying a high degree of consistency.

The post-melt-processing treatments described in this study, which are relatively straightforward and inexpensive to implement, have been able to improve significantly the mechanical reliability and thermal stability of typical (RE)BCO bulk superconductors, providing a potentially promising route to achieving 20 T trapped fields in these materials consistently.

6.1. Introduction

6.1.1. High trapped fields in (RE)BCO bulk superconductor magnets

The use of RE-Ba-Cu-O [or (RE)BCO] bulk superconductors for application as strong trapped-field magnets has been investigated by numerous research groups around the world over the past three decades [9], [159]–[162]. As discussed in Chapter 2, the peak trapped field at the centre of a superconducting sample is given by $B_{trapped} = A\mu_0 J_c R$, where A is a geometrical constant, μ_0 is the permeability of free space, J_c is the critical current density and R is the size of the single grain in which persistent supercurrents circulate.

Significant advances have been made over the years with regards to increasing the critical current density and domain size of melt-processed (RE)BCO, including the use of a seed crystal/multiple seed crystals [163], [164], optimisation of the processing conditions [165] or a RE compositional gradient in the precursor pellets to grow single grains [166][167], [168] as large as 100 mm – 150 mm in diameter; and improved flux pinning and J_c through irradiation [169]–[171] or doping [172]. This means that (RE)BCO bulk superconductors are no longer limited by their superconducting properties at high field and low temperature, but rather by their mechanical and thermal properties [67], [173].

Very high trapped fields have been reported for (RE)BCO bulk superconductors. To achieve these results, samples have typically been reinforced mechanically, and sometimes made more conductive thermally, to ensure their survival during and after magnetisation. In 1997, Fuchs *et al.* demonstrated successfully a trapped field of 8.5 T at 51.5 K in-between a pair of non-irradiated, unreinforced YBCO discs that were 24 mm in diameter [14]. However, a flux jump was observed during subsequent activation of the samples at 51 K as a result of cracking, providing direct evidence that the mechanical and thermal properties are the limiting factors in the trapping of large magnetic fields.

In 2000, Fuchs *et al.* reported a trapped field of 14.35 T at 22.5 K in-between a pair of Ag-containing YBCO discs enclosed in austenite Cr–Ni steel tubes of 2 mm in thickness [174]. The Ag particles helped to improve the intrinsic strength of the bulk superconductors while the steel tubes were used to compress the YBCO discs upon cooling as a result of the higher coefficient of thermal expansion of steel in comparison to (RE)BCO materials. The compressive stress generated within the YBCO/Ag samples compensated the tensile electromagnetic stresses and is a technique now frequently used to reinforce bulk

superconductors. Stycast, a thermally conductive epoxy encapsulant, was used to fill the space between the discs and steel tubes through vacuum-impregnation to ensure good mechanical and thermal contact. In addition, Fuchs *et al.* reported a trapped field of 11.4 T at 17 K was possible for a single 26 mm diameter Ag-doped YBCO disc enclosed in steel, demonstrating the magnitude of the potentially usable field that can be attained at the open faces of (RE)BCO trapped field magnets. During their investigation of the temperature dependence of the trapped field, Fuchs *et al.* found that zinc-doped YBCO not reinforced with a steel tube cracked at 57 K while only trapping a maximum field of 4.4 T at its surface. In contrast, they found YBCO enclosed in a steel tube could achieve 9 T at 43 K without cracking.

In 2001, Gruss *et al.* demonstrated trapped fields of up to 16 T at 24 K using YBCO/Ag discs that were doped with zinc for enhanced pinning and a more pronounced peak effect [173]. These magnets were also reinforced with steel tubes.

More recently, trapped fields of over 17 T have been achieved in the (RE)BCO composition. Tomita and Murakami demonstrated in 2003 a trapped field of 17.24 T at 29 K in a stack of two 26.5 mm diameter YBCO bulk superconductors reinforced by resin and alloy impregnation along with carbon fibre wrapping [7]. In 2014, Durrell *et al.* exceeded this performance by trapping a field of 17.6 T at 26 K in a stack of two 24 mm diameter GdBCO/Ag bulk superconductors reinforced with shrink-fit stainless-steel rings [8].

In 2020, Vakaliuk *et al.* reported the trapped field capability of commercial YBCO samples in double-sample stack, single sample and ring-shaped sample configurations [175]. A peak trapped field of 16.85 T was achieved at 30 K at the centre of the two-sample stack. The ring sample achieved a field of 9.78 T at 25 K with an applied field of 10 T, which is the highest trapped field reported for a bulk superconductor of ring geometry. Vakaliuk *et al.* also explored the reproducibility of the trapped fields of samples following magnetisation in multiple independent field-cooling cycles.

There has also been an increasing amount of interest in using layers of high temperature superconducting tape stacked together to form hybrid bulk superconductors, as persistent currents are induced in the superconducting layers during magnetisation. In 2018, Patel *et al.* reported a trapped field of 17.66 T at 8 K in a 34.4 mm diameter stack of tapes [176], which was able to sustain a trapped field of 17.6 T up to 14 K.

6.1.2. Motivation for the proposed study

A trapped field of over 20 T seems attainable in (RE)BCO bulk superconductors with the current state-of-the-art material processing techniques that enable the fabrication of large, well-connected superconducting single grains with excellent $J_c(B, T)$. This prospect has been suggested through extrapolating the field profiles observed in various experimental studies [7] and through numerical modelling using realistic superconducting properties [177]. However, a number of performance-limiting factors have to be addressed for such high fields to be realised in practice.

Firstly, the low tensile strength of these characteristically brittle materials, which is governed by the large number of inherent small-scale defects within the microstructure, places an upper limit on the electromagnetic stress a superconductor can withstand during magnetisation. Konstantopoulou *et al.* determined the tensile strength of YBCO and GdBCO/Ag single grains to be 31 MPa and 34 MPa [92], respectively. Since the Lorentz force $F_L = J_c \times B$ scales strongly with J_c, the mechanical strength of the material, in turn, limits the field a superconductor can trap. Experimental work has revealed the appearance of large cracks in single-grain samples as a result of high-field magnetisation [67], which was accompanied by a sudden and undesirable decrease in the peak trapped field and formation of double peaks in the field profile.

Secondly, bulk (RE)BCO generally exhibits low thermal conductivity [7], [178], around 20 W/mK along the *ab*-plane and around 4 W/mK along the *c*-axis, so thermal instabilities can arise when a large amount of heat $Q = E \cdot J$ is generated due to flux movement during magnetisation, leading to catastrophic flux jumps. Bulk superconductors are highly susceptible to flux jumps below 30 K [173]. Cracks and flux jumps are likely to be interlinked in the failure of (RE)BCO bulk superconductors as both are usually observed in a failed sample. To address these issues and achieve trapped fields of up to 18 T, previous studies have aimed to reinforce bulk samples mechanically and enhance the thermal conductivity through metallic inclusions.

There are still other concerns pertaining to practical applications of these trapped field magnets. Firstly, the statistical nature of the failure mechanism means trapped fields of over 17 T could not be attained reliably, even for a batch of samples nominally fabricated identically. This was discussed by Durrell *et al.*, where three sample stacks of similar composition and structure to the 17.6 T record stack were also magnetised under similar conditions at the same experimental

facility [8]. The first stack suffered cracking and only trapped 10 T, the second successfully trapped 15.4 T, while the third also failed during magnetisation. This indicated that the samples exhibit a wide range of performance that is difficult to predict. It is easy to understand the widespread performance of (RE)BCO bulk superconductors by considering the tensile strengths measured on the standard YBCO single grains in Chapter 5. The tensile strengths ranged from 10.7 MPa to 19.6 MPa, as shown in Figure 5.5, which would have caused the achievable trapped fields to range from 9.5 T to 12.8 T, demonstrating a high degree of variation amongst unreinforced samples.

Secondly, the magnetisation process can also cause existing micro-cracks in the single grains to grow steadily in a quasi-brittle way, damaging the samples at high field such that they cannot trap as high of a field repeatedly following successive magnetisation. This was also reported by Durrell *et al.*, following the failure of the 17.6 T two-sample stack due to crack formation during the second magnetisation procedure.

The work described in this chapter sets out to improve the mechanical reliability and thermal stability of as-grown (RE)BCO trapped field magnets, such that higher maximum trapped fields can be achieved in established sample compositions and with better consistency [179].

The concept proposed in this study was inspired by work carried out by Morita *et al.* in 2017 [180], [181], where they established that a laminated structure, when applied to ring-shaped bulk magnets, decreased significantly the mechanical strains experienced by the superconductor during magnetisation and prevented crack formation. In the present study, a similar composite assembly has been proposed, as shown in Figure 6.1, comprising of a strengthened laminated structure formed by sandwiching stainless steel sheets/discs in between layers of bulk superconductor, which were assembled using Stycast epoxy resin. The assembly was then enclosed in shrink-fit stainless-steel ring.

It is likely the composite proposed in this study also benefits from enhanced thermal conductivity and heat capacity from a thermal stability viewpoint. This should ultimately help to alleviate the occurrence of flux jumps as the heat generated locally could be dissipated more rapidly by the stainless steel in the structure and the fixed amount of thermal energy generated by flux movement would result in a comparatively smaller increase in the temperature of the composite structure.
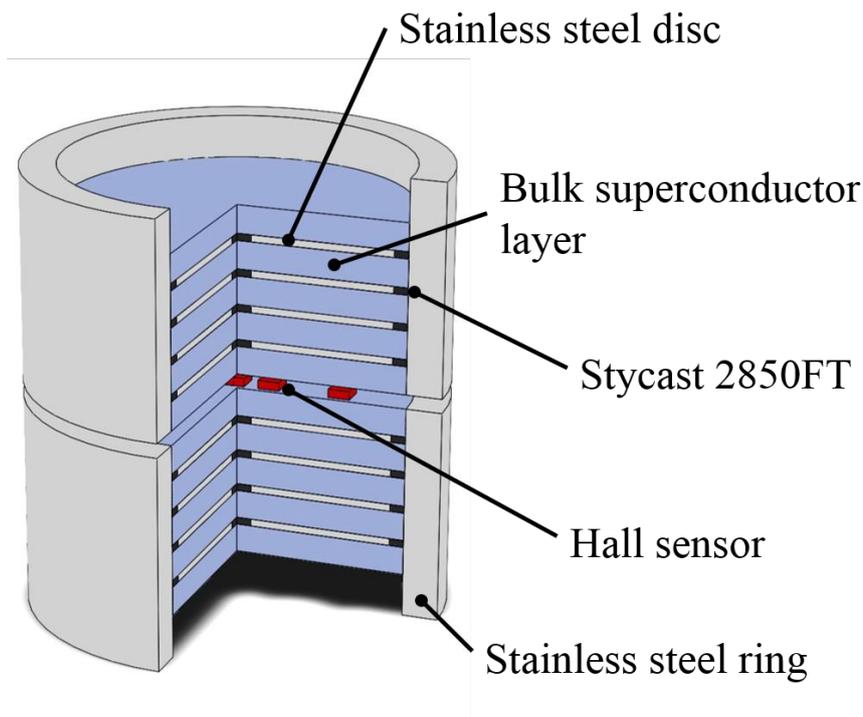
Figure 6.1. Partial section view of the composite bulk superconductor structure proposed and implemented in this study, showing the layers of superconductor and stainless steel. The magnetic field profile is measured using a linear array of Hall sensors placed at the centre of the stack.

6.2. Numerical simulations

To enable the design and assessment of mechanical reinforcement arrangements, two-dimensional (2D) axisymmetric finite element models, implemented in COMSOL Multiphysics, were used to study the field-trapping potential and mechanical stress distribution in various bulk superconductor structures during field-cooled magnetisation. The numerical modelling follows the same framework described in Chapter 4 and in [125]. In summary, the 'Magnetic Field Formulation', 'Heat Transfer in Solids' and 'Structural Mechanics' interfaces were coupled together to allow for a comprehensive study of, firstly, the thermal stresses σ_θ^{COOL} arising from differential thermal contraction of the different materials in the composite structure and, secondly, the electromagnetic stresses σ_θ^{FCM} arising from interaction between the current and the magnetic field. The computational study will focus on the hoop stress σ_θ which is generally larger than the radial stress σ_r in cylindrical bulk superconductors.

The $J_c(B, T)$ characteristics used in the numerical simulations were taken from the study published by Ainslie *et al.* [125], which were established from a representative GdBCO/Ag SQUID specimen for fields of up to 5 T over a temperature range of 30 – 92 K. The curves were subsequently extended to 20 T using the equation proposed by Jirsa *et al.* [130], as described in Chapter 4. The $J_c(B, T)$ data, which were input into the model using interpolation with temperature and field as the two variables, are shown in Figure 6.2.

A list of the relevant material properties used in the models, including references to the relevant literature, can be found in Table 6.1.

6.2.1. Field-trapping potential of (RE)BCO bulk stacks

The trapped field that can be achieved theoretically at the centre of a pair of (RE)BCO bulk superconductors, which is the configuration used in several existing experimental studies, was determined by taking into account only the $J_c(B, T)$ performance of the superconductor and ignoring any mechanical limitations.

Figure 6.3 shows the temperature-dependence of the theoretical trapped field at the centre of the two-sample stack constructed from bulk samples 24 mm in diameter and 12 mm in thickness. With an applied field of 18 T (value was chosen to be consistent with published experimental studies) and at temperatures below 35 K, the trapped field is no longer limited by the current-carrying capability of the superconductor, but rather by the magnitude of the applied field. This is in strong agreement with the field profiles measured by Durrell *et al.* and Tomita and Murakami [7], [8], at 26 K and 29 K, respectively. Both studies reported a flat field distribution towards the centre of the bulk stack that would suggest the bulk superconductors were not fully saturated and that higher trapped fields were possible at those temperatures.

Figure 6.3 implies trapped fields of over 20 T and 30 T are achievable in the two-sample stack at 30 K and 20 K, respectively. The modelling results also suggest that the volume fraction of superconducting material in a composite structure could potentially be reduced and the stack would still be able to trap a sufficiently high field at low temperature due to the high $J_c(B, T)$ of state-of-the-art (RE)BCO material.

Table 6.1. List of assumed material properties in the 2D FEM model of the composite structure.

Parameter	Description	Value	Reference(s)
n	n value (E–J power law)	20	[129]
E_0	Characteristic voltage (E–J power law)	1×10^{-4} V m^{-1}	[129]
$J_c(B, T)$	Critical current density	Interpolation – shown in Figure 6.2	[19, 20]
E_{bulk}	Young's modulus (bulk superconductor)	1×10^{11} Pa	[124], [133], [182]
$E_{stainless}$	Young's modulus (stainless steel)	1.93×10^{11} Pa	[124], [182]
E_{epoxy}	Young's modulus (epoxy resin)	9×10^{9} Pa	[183]
ν_{bulk}	Poisson's ratio (bulk superconductor)	0.25	[134]
$\nu_{stainless}$	Poisson's ratio (stainless steel)	0.28	[124], [182]
ν_{epoxy}	Poisson's ratio (epoxy resin)	0.33	[184]
a_{bulk}	Coefficient of thermal expansion (bulk superconductor)	5.2×10^{-6} K^{-1}	[124], [133], [182]
$a_{stainless}$	Coefficient of thermal expansion (stainless steel)	1.27×10^{-5} K^{-1}	[124], [182]
a_{epoxy}	Coefficient of thermal expansion (epoxy resin)	3.9×10^{-5} K^{-1}	[183]
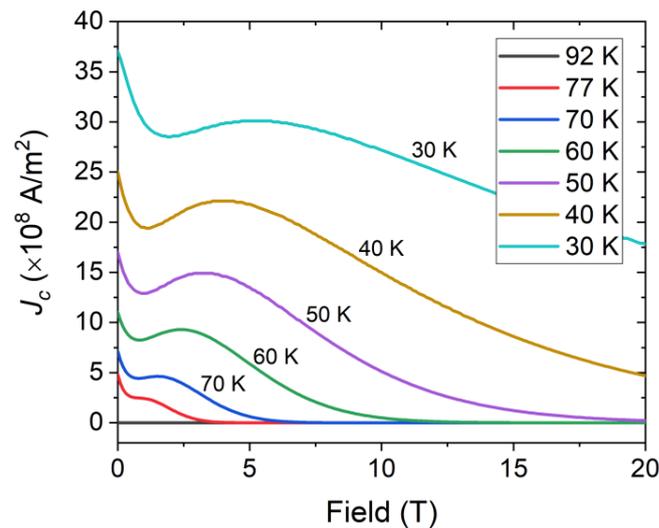
Figure 6.2. $J_c(B, T)$ data used in the 2D FEM models. These were measured from a representative SQUID specimen, cut from a single-grain GdBCO/Ag bulk superconductor.
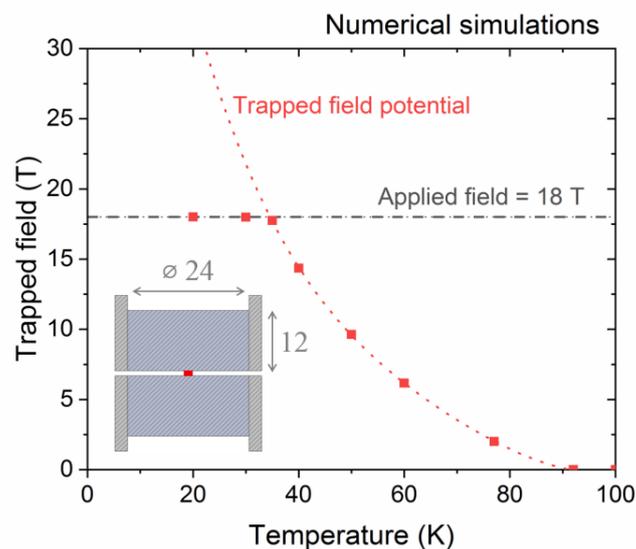
Figure 6.3. Numerical simulation results for the trapped magnetic field achievable at the centre of a conventional two-sample stack at various temperatures with an applied field of 18 T (solid red squares). The field potentially achievable with an arbitrarily high applied field and in the absence of mechanical limitations is shown by the red dotted line. The inset shows the sample geometry used in the numerical simulations. The magnitude of the applied field and the sample dimensions were chosen to reflect those reported in published experimental studies.

6.2.2. Stresses in the composite structure

Figures 6.1 and 6.4 show the composite bulk structure proposed and used in this study. The structure is similar to the laminated structure proposed by Morita *et al.* [180], [181]; although the fabrication procedures differ in that their approach utilised silver sputter deposition on the superconductor layers, further heat treatment and joining of the layers via solder. Figure 6.4 shows a cross-sectional view of the geometries used in the numerical modelling of the bulk superconductor stacks. A stack without the stainless-steel laminations, referred to here as the 'standard' stack, was also modelled for comparison. Positions $z = 0.5$ mm and $z = 6.5$ mm have been marked in the diagrams, corresponding to the surface and mid-plane of the upper bulk sample in each case.
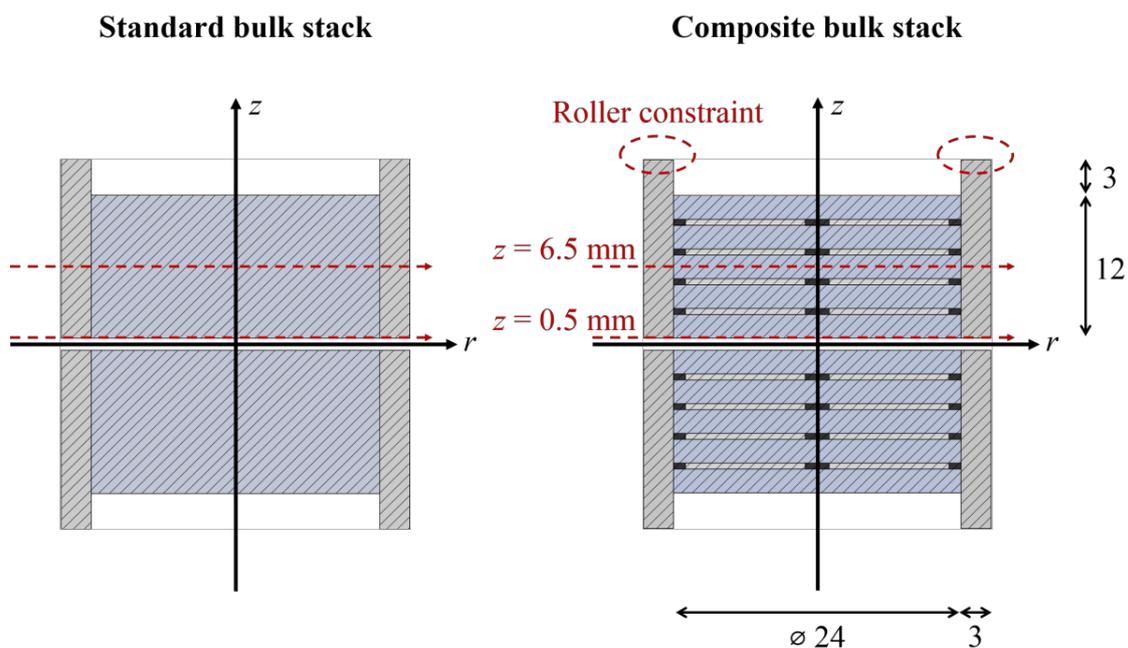
Figure 6.4. Schematic of the cross-sectional views of a conventional, 'standard' sample stack and the 'composite' sample stack investigated in the numerical simulations. The lines marked $z = 0.5$ mm and $z = 6.5$ mm correspond, respectively, to the top surface and mid-plane of the bulk superconductor in the upper half of each structure.

There is continuity of displacements across every interface in the modelled stacks, which is the default boundary condition built into the 'Structural Mechanics' module in COMSOL. This condition implies perfect mechanical connection between adjacent materials at every interface and that the stresses will be transferred accordingly. A 'roller' constraint was applied to the top of the stainless-steel rings, as shown in Figure 6.4, to simulate attaching the sample stacks to the end of a measurement probe. Lastly, only the upper halves of the stacks, i.e. $z > 0$ mm, were modelled given the symmetry of the arrangement.

Figure 6.5(a) shows the thermal hoop stress σ_θ^{COOL} across the standard stack at 30 K just before the field was ramped down. This was taken prior to the magnetisation process, in which case, the electromagnetic stresses σ_θ^{FCM} were zero. The initial position of the structure is outlined in black, and the deformation has been exaggerated by $\times$ 25 to illustrate the way the structure deforms upon cooling and to demonstrate the effect of differential thermal contraction.

The stainless-steel ring contracts more significantly than the bulk superconductor along the z-direction when cooled due to the difference in their coefficients of thermal expansion, causing the upper and lower surfaces of the bulk superconductor to be somewhat bowed and in tension. While the steel ring is highly effective in generating compressive stress at the centre of the bulk superconductor and averting it from brittle mechanical failure there, the ring results in significant tensile stress on the open surfaces of the stack.

On the other hand, Figure 6.5(b) shows σ_θ^{COOL} in the composite stack at the same point in time and plotted using the same colour scale, for which it can be seen that the inclusion of the stainless-steel sheets/discs results in a more compressive stress state overall prior to ramping down the external applied field. This is due to the stainless-steel sheets contracting more quickly than the bulk superconductor layers along the a–b direction (or r-direction in Figure 6.5), causing the superconductor layers to be compressed by the neighbouring steel/resin layers.

According to the models, the composite arrangement experienced σ_θ^{COOL} that is almost 100 MPa more compressive at the centre and around 60 MPa more compressive towards the edge of the bulk superconductor along the $z = 0.5$ mm plane.
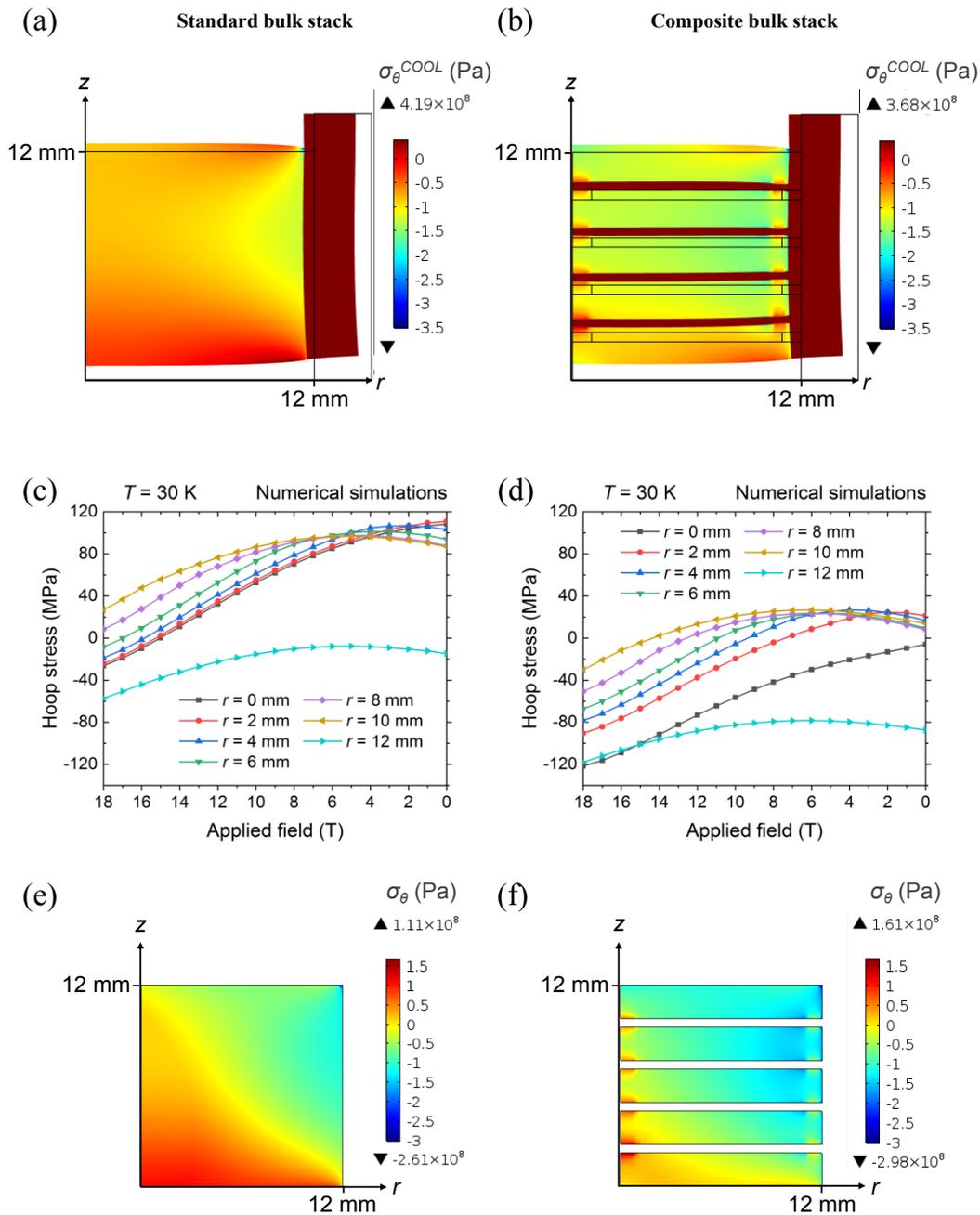
Figure 6.5. (a) Thermal hoop stress σ_θ^{COOL} across the standard stack as a result of cooling from 300 K to 30 K. The deformation has been exaggerated by × 25. (b) Thermal hoop stress across the composite stack as a result of cooling to 30 K. (c) Total hoop stress $\sigma_\theta^{COOL} + \sigma_\theta^{FCM}$ experienced by the standard stack along $z = 0.5$ mm during ramp down of the applied field from 18 T to 0 T at 30 K. (d) Total hoop stress experienced by the composite stack along $z = 0.5$ mm during ramp down of the applied field. (e) Hoop stress $\sigma_\theta^{COOL} + \sigma_\theta^{FCM}$ throughout the cross-section of the standard stack at the end of the magnetisation process. (f) Hoop stress throughout the cross-section of the composite stack at the end of the magnetisation process.

Figure 6.5(c) and Figure 6.5(d) show the evolution of the hoop stresses $\sigma_\theta^{COOL} + \sigma_\theta^{FCM}$ along the $z = 0.5$ mm plane in both stacks as the field was ramped down from 18 T at 30 K. The stresses shown at 18 T, i.e. at the beginning of the magnetisation process, correspond solely to the thermal hoop stresses σ_θ^{COOL} that are shown in Figure 6.5(a) and Figure 6.5(b). Changes in the hoop stress as the field was ramped down correspond to the electromagnetic contribution σ_θ^{FCM}.

The total hoop stress $\sigma_\theta^{COOL} + \sigma_\theta^{FCM}$ reached 111 MPa along $z = 0.5$ mm in the standard stack during magnetisation, whereas the maximum hoop stress in the composite stack was only 27 MPa. It is clear from the models that the standard stack will probably not survive the magnetisation process based on the flexural strength of ~ 105 MPa and splitting tensile strength of ~ 34 MPa measured by Konstantopoulou *et al.* for GdBCO/Ag single grains at 77 K [92]. Furthermore, due to the increased stiffness of the composite structure, the electromagnetic hoop stress contribution σ_θ^{FCM} was suppressed by around 20 MPa compared to the standard stack.

Figure 6.5(e) and Figure 6.5(f) show the stress distribution $\sigma_\theta^{COOL} + \sigma_\theta^{FCM}$ in the superconducting material at the end of the field-cooled magnetisation process. It can be seen from a comparison of the figures that the volume of superconductor under high tensile stress has been reduced significantly with the incorporation of the stainless-steel sheets, with most of the high tensile stresses confined to the stainless-steel layers. The maximum and minimum stresses in the superconductors are also shown in the legend for reference.

The mechanical improvements shown by the numerical modelling can also be understood simplistically with the Voigt model of a two-phase composite under axial loading [185], where a secondary phase reinforcement is aligned with the axis of the applied load. Since the strains in the stainless-steel sheets and bulk superconductor layers must be equal and the stainless-steel sheets are significantly stiffer than the bulk layers, the reinforcement sheets are subject to considerably higher stresses than the superconducting matrix and there is a redistribution of load. Additionally, the composite structure has an increased stiffness overall, compared to the superconductor alone, with a maximum value given by the weighted mean of the stiffnesses of the two phases, which depends on the volume fraction of stainless steel.

The integration of a laminated structure had only a minor impact on the trapped field. The simulations revealed that the peak field at the centre of the composite stack was not affected by the inclusion of the stainless-steel layers, as both the standard and composite stacks trapped

18 T at 30 K. However, the trapped field profile for the composite stack was slightly sharper in comparison to the standard stack, i.e. the field decayed more quickly with radial position and thus formed a narrower conical profile.

Additional positive effects that were difficult to demonstrate with the simulations include the ability of the composite to resist catastrophic fracture across the entire structure, since the stainless-steel sheets (with high fracture toughness and high tensile strength) prevent cracks from propagating from one superconductor layer to another. Secondly, the possibility of filling the exposed pores and defects of each superconductor layer once they have been cut from the parent bulk superconductor can increase significantly the tensile strength of the superconductor itself [85], [186], [187]. Finally, reduced probability of flux jumps, and improved thermal stability, could have resulted from a reduced volume fraction of superconductor, which reduces the amount of heat produced in the structure.

6.3.   Experimental details

6.3.1.   Sample preparation and reinforcement

Single-grain, silver-doped Gd-Ba-Cu-O bulk superconductors (GdBCO/Ag), approximately 25 mm in diameter and 12 mm in thickness, were fabricated by Dr Yunhua Shi using top seeded melt growth [188]. To ensure they were single grains, each sample was first magnetised with an applied field of 1.5 T at 77 K to obtain a trapped field profile. Both samples exhibited a conical trapped field distribution, with peak fields of 0.93 T and 0.94 T.

The GdBCO/Ag bulk superconductors were cut using a diamond saw into five slices of approximately equal thickness to form the laminated composite shown in Figure 6.1. These slices were about 2 mm thick after cutting. Four discs of stainless steel (grade 304), 22 mm in diameter and 0.51 mm in thickness, were then sandwiched in between the GdBCO/Ag slices and glued together using Stycast 2850 FT (mixed with 23 LV catalyst), as shown in Figure 6.6(a). A thickness of 0.51 mm (equivalent to 24 AWG) was chosen for the steel discs since the cutting process removed around 0.5 mm of superconductor per cut. Once glued together, the composites were machined down to a diameter of 24.1 mm. A stainless-steel ring (also grade 304), with an inner diameter of 24.0 mm and outer diameter of 29.0 mm, was then heated

to 300 °C prior to shrink-fitting over each composite arrangement. An interference fit helped to increase the compressive stress in the bulk superconductor.

A linear array of five Hall sensors (Lakeshore HGT–2101) was placed in between the stack at radial positions of - 7.5 mm, - 2.5 mm, 0 mm, 2.5 mm and 7.5 mm from the centre of the stack, as shown in Figure 6.6(b). The two composite bulk samples were then combined into a pair/stack using Stycast epoxy resin with their top surfaces (i.e. where the seed crystals were placed during melt processing) both pointing towards the centre of the stack, as shown in Figure 6.6(c).
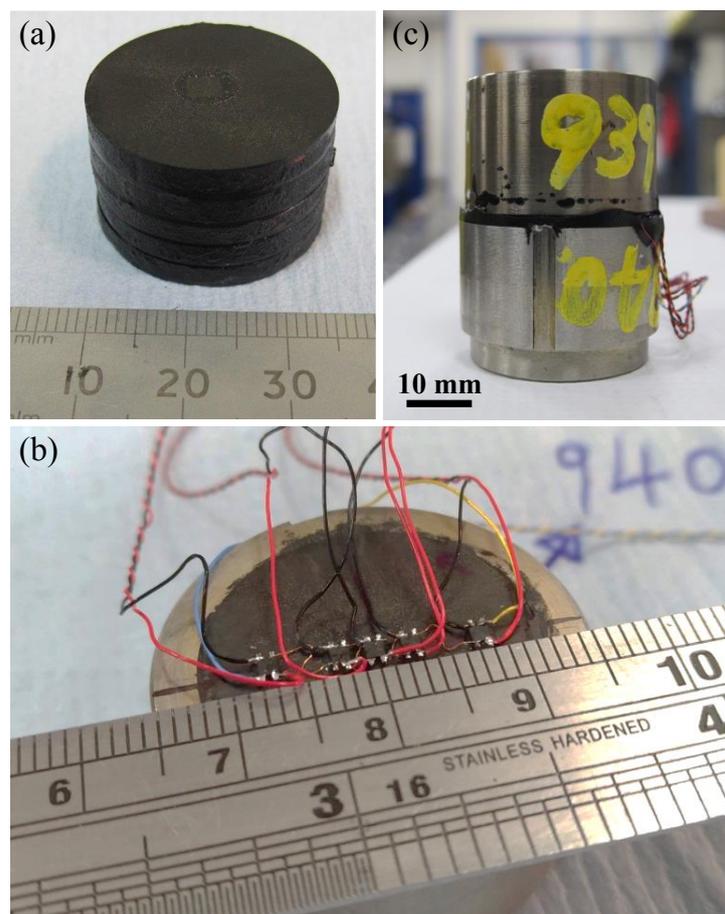
Figure 6.6. (a) Representative bulk superconductor composite, showing the layers of stainless-steel and GdBCO/Ag bulk superconductor held together using Stycast, before being machined and shrink-fitted into stainless steel rings. (b) Positions of the five Hall sensors mounted between the two samples. (c) Photograph of the two-sample stack, held together using Stycast.

For comparison, a "standard" stack was also fabricated under identical conditions, but without the steel lamination. For the standard stack, the shrink-fit stainless-steel rings were made 0.5 mm thicker in wall thickness to explore whether increasing the compressive stress on the bulk samples was sufficient to prevent sample failure. The samples used in the standard stack also exhibited peak trapped fields between 0.9 T and 1.0 T at 77 K.

6.3.2.　Trapped field measurements

The output voltage of each Hall sensor was measured as a function of the external applied field in order to determine the field measured at discrete points along the centre of the stack. The Hall sensors were driven by a 22 Hz, 10 µA peak sine wave generated by a Keithley 6221 current source, and the Hall voltage was measured using a lock-in amplifier for each sensor. A calibrated Cernox sensor on the end of the stack was used to measure the temperature of the stack, while the sample temperature was controlled and stabilised using a wire-wound heater wrapped around the stack.

The standard and composite stacks were magnetised in the bore of the 18 T SCM2 system at the National High Magnetic Field Laboratory (NHMFL), Florida State University. The measurements were carried out by Dr John Durrell and Dr Jan Srpčič.

The field-cooled magnetisation procedure was as follows: an external field of 18 T was applied whilst the stack temperature was held at 100 K, i.e. above the critical temperature. Once the field was stable at 18 T, the stack was cooled to the desired measurement temperature between 20 K and 30 K and allowed to stabilise. Finally, the external field was removed slowly at a rate of 0.015 – 0.02 T/min, and the resultant trapped field and subsequent flux creep were measured at the set temperature.

6.4.　Results and discussion

6.4.1.　Standard stack

The standard stack was magnetised and measured using the same experimental arrangement for consistency. Figure 6.7 shows the field measured between the samples as the applied field

was ramped down from 18 T at 26 K with a ramp rate of 0.016 T/min. The trapped field initially remained high, suggesting a high and stable $J_c(B)$, and with the field at the central hall sensor decreasing by a minimal amount. The fields measured by sensors 2, 3 and 4 were 17.7 T, 18.0 T and 17.7 T, respectively, when the external field was reduced to 9 T.

A sudden drop in field was then observed across the stack, indicating that a crack has formed, or a flux jump has occurred. This was immediately followed by a sharp rise in the temperature of the stack from 26 K to 38.8 K. Immediately after the sudden decrease, the field measured at $r = -7.5$ mm was actually higher than that at $r = 0$ mm, indicating a significant re-distribution of the pinned magnetic flux.

This behaviour is commonly observed in (RE)BCO bulk superconductors magnetised at low temperature. Tomita and Murakami reported an abrupt decrease in field in a two-sample YBCO stack, which they were able to prevent subsequently in a separate but similar stack impregnated with Bi-Pb-Sn-Cd alloy to improve thermal stability [7].
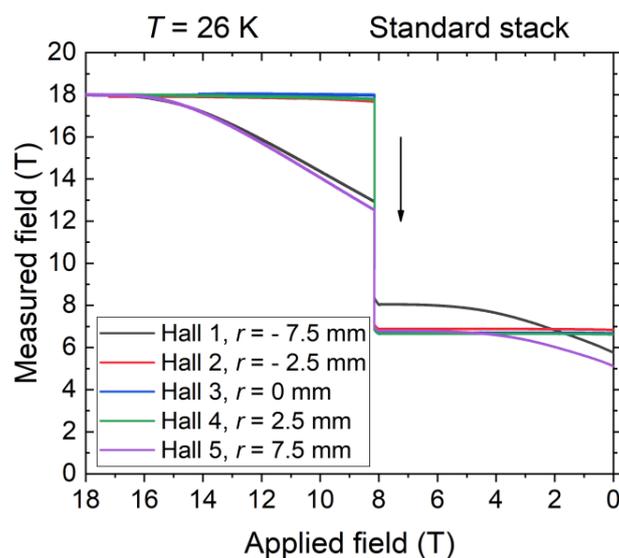
Figure 6.7. Magnitude of the field measured at the centre of the two-sample standard stack at 26 K as the external field was ramped down from 18 T.

6.4.2. Trapped fields > 16 T in the composite stack

The composite stack was magnetised initially by field cooling in 18 T at 26 K with a constant ramp down rate of 0.02 T/min, which resulted in a trapped field of 16.8 T immediately after the complete removal of the applied field. The field measured at five positions across the centre of the stack during the magnetisation process is shown in Figure 6.8(a). The sample was then warmed slowly at a rate of approximately 1 K/min to determine the temperature dependence of the trapped field distribution, as shown in Figure 6.8(b). From the warm-up curves, it can be seen that a field of 11.4 T and 8.2 T was maintained at 40 K and 50 K respectively, which are temperatures that could be achieved easily with portable commercial cryocoolers.

Minor changes in the gradient of the field measured at $r = 0$ mm towards the end of the magnetisation process, evident in Figure 6.8(a), hint at the effect of the additional mechanical reinforcement and thermal stability provided by the composite structure. It is possible that this behaviour corresponds to the beginning of crack formation or flux instabilities that could have led to an avalanche within the bulk superconductor layers, but they appear to be suppressed by the composite structure with enhanced stability. For instance, if a crack has formed in one of the superconductor layers, its propagation may have been prevented by the neighbouring stainless-steel layers, obviating catastrophic structural damage. Similarly, if regions of a superconductor layer began to warm up due to flux movement, the local heat could have been dissipated quickly by the local stainless-steel sheets.

The stack was then de-magnetised and re-magnetised using a similar process to confirm repeatability, since it did not show any evidence of a catastrophic failure during the initial cycle. The second cycle involved field cooling the stack in a field of 18 T at a lower temperature of 22.5 K following a constant ramp-down rate of 0.015 T/min. This produced a trapped field of just over 17.6 T immediately after the complete removal of the applied field. The fields measured during the magnetisation are shown in Figure 6.9(a). The 17.6 T trapped field, which is comparable to the highest field ever trapped by a bulk superconductor at any temperature, was obtained by averaging the field measured over 100 seconds after the external field reached zero to minimise error due to noise.

Minor asymmetry towards the edge of the stack can be seen in Figure 6.9(b), where the fields measured by the Hall sensors positioned at $r = \pm 7.5$ mm differed by 2.5 T. This may be due to asymmetry in the $J_c(B)$ properties of one or both of the composite bulk superconductors, to a

small error in the positioning of the Hall sensors, or to a small misalignment of the two composite samples.
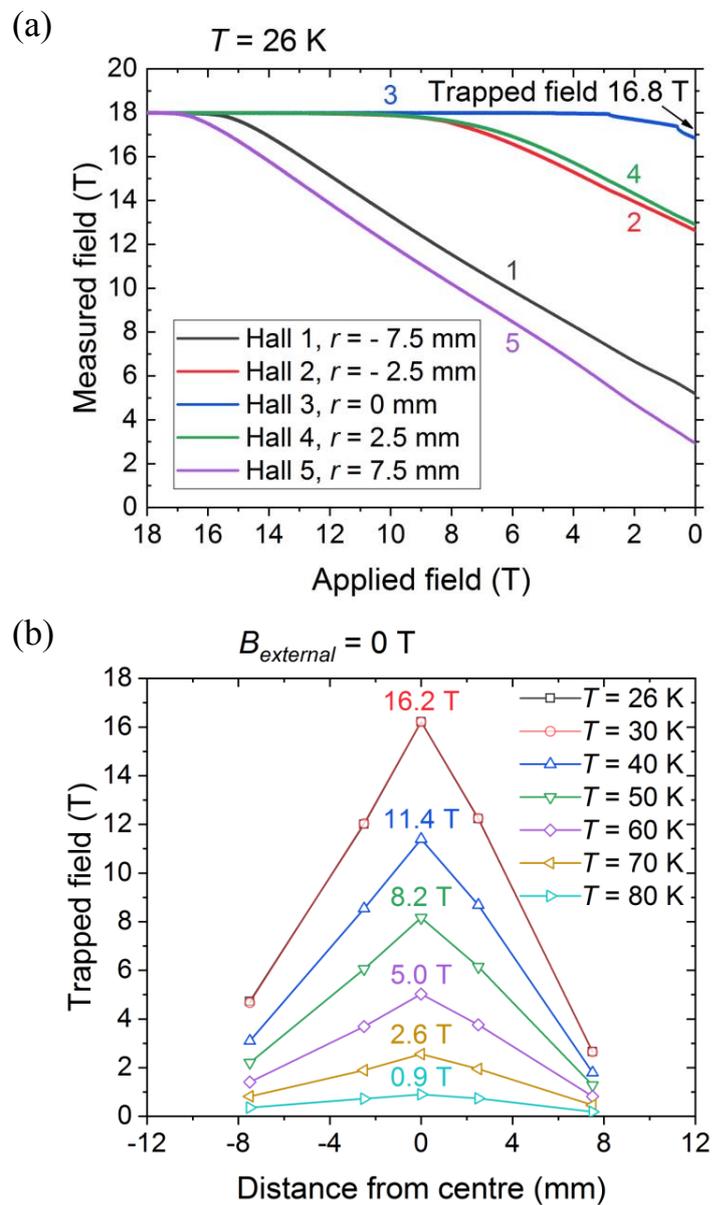
Figure 6.8. (a) Magnitude of the field measured at the centre of the two-sample GdBCO/Ag composite stack at 26 K as the external field was ramped down from 18 T. The residual trapped field is shown at the end of the ramp. (b) Trapped field profiles measured at various temperatures as the sample stack was warmed slowly at a rate of approximately 1 K/min after the removal of the applied field. The field measured by the central Hall sensor is shown at 10 K temperature increments.

(a)

(b)
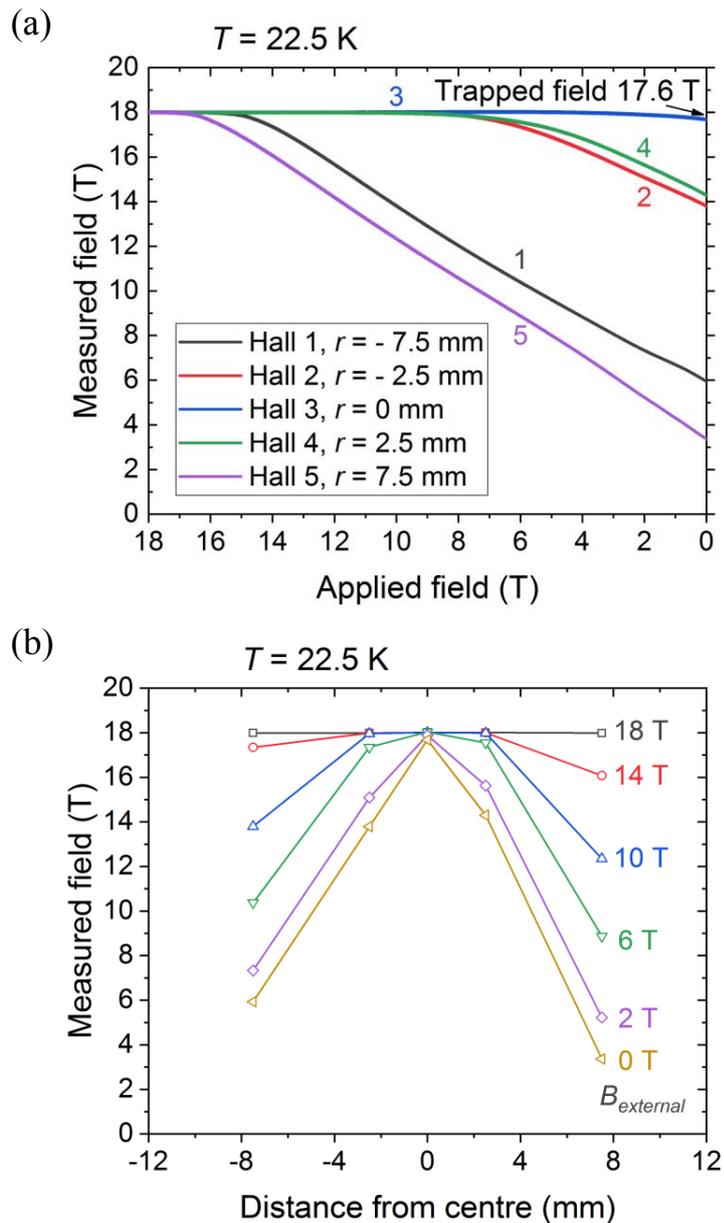
Figure 6.9. (a) Magnitude of the field measured at the centre of the two-sample GdBCO/Ag composite stack at 22.5 K as the external field was ramped down from 18 T. The residual trapped field is shown at the end of the ramp. (b) Field profiles measured at various points during the ramp-down of the applied field as the stack temperature was maintained at 22.5 K.
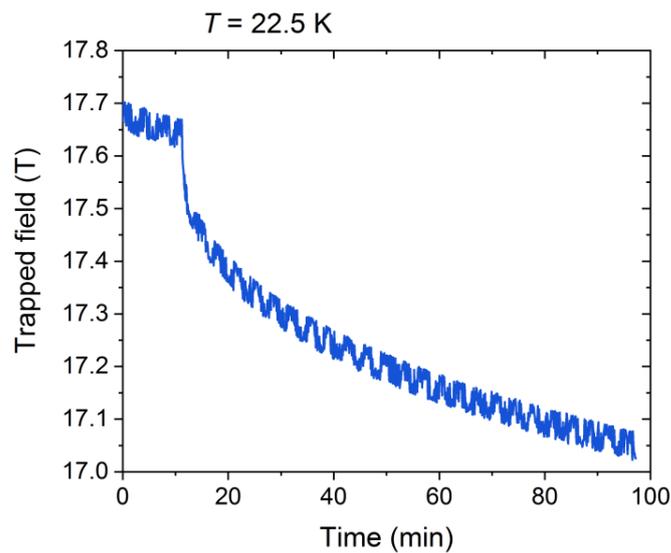
Figure 6.10. Decay of the trapped field in the GdBCO/Ag composite stack as a result of flux creep immediately after the removal of the external field and after trapping 17.6 T. The stack temperature was maintained at 22.5 K throughout the measurement.

Subsequently, to determine the decay in trapped field with time as a result of flux creep, the trapped field was recorded for 100 minutes with the sample temperature held at 22.5 K, as shown in Figure 6.10. The flux creep measured in this composite stack appears to be more severe than the 17.6 T stack of standard GdBCO/Ag stack reported by Durrell *et al.* [8]. This weaker flux pinning may be due to the gap between each superconductor layer, which is absent in the standard stacks. This could potentially be a drawback of this composite approach and needs to be investigated further.

The effectiveness of the proposed composite structure, as predicted by detailed numerical simulations, has been verified by the high trapped field achieved experimentally, which is comparable to the highest trapped fields reported to date. In addition, these results were significant because reliable and reproducible magnetisation with an applied field of 18 T at temperatures below 30 K without the samples failing mechanically or thermally has been demonstrated here to be possible. Despite being the first stack to be manufactured and measured, it was able to survive two independent high-field magnetisation cycles, initially achieving 16.8 T at 26 K and then 17.6 T at 22.5 K. This is noteworthy because there is high variability amongst conventional stacks of (RE)BCO single-grain bulk superconductors, due

most likely to variation in the defect distribution from sample to sample, as Durrell *et al.* discussed in their study [8]. To the best of our knowledge, previous studies have not been able to re-magnetise successfully a multi-sample stack under such high field conditions.

On the whole, the composite arrangement can be perceived as a hybrid between a standard bulk superconductor disc and a stack of tapes. Stacked tapes have superior mechanical and thermal stability as a result of their large metallic volume fraction (> 90 %), although they require a low operating temperature due to their relatively low engineering current density J_e. On the other hand, bulk superconductors have high J_c of the order of 10^9 A/m^2 below 50 K, which means higher operating temperatures can be used, but they often fail due to their poor mechanical and thermal properties. The composite structure reported here can be viewed as a practical compromise between the two types of trapped field magnet. This is also evident from the temperature required to achieve trapped fields of around 17.6 T, which was achieved at 26 K in the standard bulk stack [8], whereas the stacked tapes had to be cooled to 8 K [176]. The composite structure reported here needed to be cooled to 22.5 K.

A flux jump was observed in the composite stack after the magnetisation cycle that achieved 17.6 T as the samples were warmed up too rapidly due to experimental time constraints. It is likely that this could have resulted in cracking of the GdBCO/Ag samples. A distortion of the trapped field profile was later confirmed when the stack was field cooled at 77 K again back in Cambridge and the sample re-measured.

6.5.   Additional experimental results

The results presented and discussed in Section 6.4 were from the first stack fabricated following the composite approach. The stack was measured at NHMFL in June 2019.

Two more composite stacks were fabricated by Dr Yunhua Shi following the procedures outlined in Section 6.3 and were measured at NHMFL by Dr John Durrell and Mr Tony Dennis in March 2020. In the March 2020 measurements, a 31 T magnet system was used to magnetise the samples in an attempt to exceed the current record of 17.6 T. The March 2020 measurements are discussed briefly below.

The first stack, fabricated from GdBCO/Ag bulk superconductors approximately 24 mm in diameter, was field cooled using a 20 T applied field at 25 K. The stack successfully trapped 15.4 T at 25 K in its first field cycle. Due to time constraints, a ramp rate of 0.05 T/min was used when reducing the external field, which was significantly faster than that employed in the June 2019 measurements. The survival of the stack at such a high ramp rate, which directly affects the rate at which heat is generated by the superconducting layers, strongly supports the concept of additional thermal stability provided by the composite structure. The stack, however, did not survive a subsequent field cooling cycle from 21 T at 20 K.

The second stack, fabricated from GdBCO/Ag samples approximately 27.5 mm in diameter, was also field cooled using a 20 T applied field at 25 K with a ramp rate of 0.05 T/min. Similarly, this stack survived its initial cycle, successfully trapping 16.4 T at 25 K, as shown in Figure 6.11. However, the stack also failed during a second field cycle at a lower temperature and higher applied field, where it showed multiple failures during the ramp down of the external field.
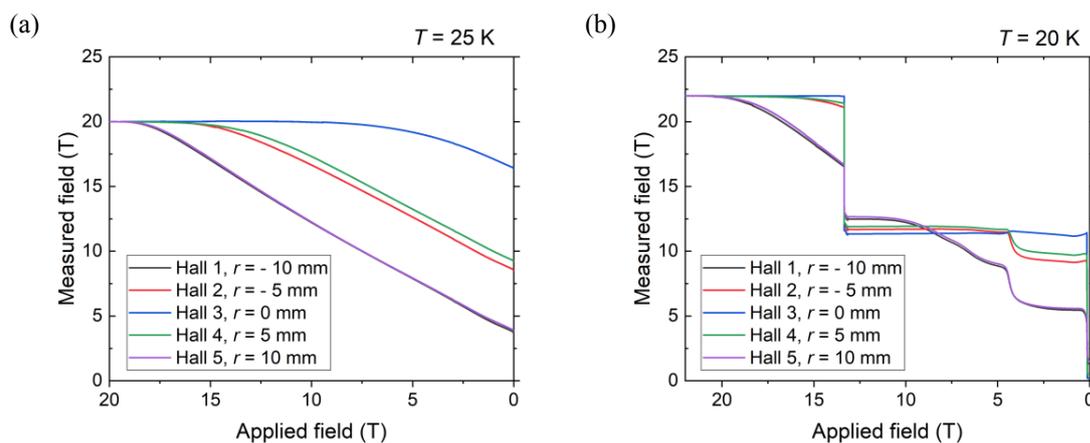

Figure 6.11. (a) Magnitude of the field measured at the centre of the two-sample GdBCO/Ag composite stack at 25 K as the external field was ramped down from 20 T. A trapped field of 16.4 T was achieved at the end of the ramp. (b) Magnitude of the field measured at the centre of the stack at 20 K as the external field was ramped down from 22 T in a subsequent cycle.

The trapped field results obtained so far have been encouraging, as trapped fields of at least 15 T were demonstrated in the three stacks measured so far. This study also suggests that with further optimisation, for example, in terms of the ratio of superconductor to stainless steel in the laminate and in terms of the magnetisation parameters, the composite reinforcement technique may be a promising route to ensure (RE)BCO trapped field magnets are sufficiently stable, mechanically and thermally, to support trapped fields of over 18 T in the near future.

6.6.   Conclusions

In this chapter, the modelling, fabrication and sequential high-field magnetisation of a stack of GdBCO/Ag bulk superconductors strengthened with stainless steel laminates and shrink-fit stainless-steel rings have been described. The inexpensive and straightforward sample preparation processes proposed in this study were aimed directly at improving the mechanical reliability and thermal stability of the (RE)BCO sample stacks, which are issues that hinder the consistent generation of trapped fields exceeding 16 T, even by samples fabricated nominally identically.

Through field cooling, the composite stack successfully trapped 16.8 T at 26 K initially, followed by 17.6 T at 22.5 K in a second independent cycle. This first stack was able to achieve a trapped field comparable to the highest trapped fields reported to date for bulk superconducting magnets of any mechanical and chemical composition and at any temperature. In addition, this was also the first time such a high field has been reproduced in a single stack.

Measurements on two other composite stacks fabricated by the Bulk Superconductivity Group provide further supporting evidence of the advantages of the proposed structure, as both stacks survived their initial magnetisation procedures and successfully trapped magnetic fields of around 16 T.

Post-melt-processing treatments that can be carried out after the growth of large (RE)BCO single grains, such as those described in this study, are highly desirable due to the sensitive nature of the melt growth process and difficulty in adding inclusions to the superconducting phase matrix, i.e. to improve mechanical strength, fracture toughness or thermal conductivity, without affecting the superconducting properties significantly.

It is also fair to speculate that the composite approach described could be even more effective and valuable in larger (RE)BCO single grains, which are expected to exhibit worse mechanical properties despite possessing better field-trapping capability.

Chapter 7

Conclusions and future research

7.1. Conclusions

Having demonstrated the ability to trap magnetic fields in excess of 17 T, single-grain (RE)BCO bulk superconductors have shown great potential for a wide range of innovative and technologically important engineering applications, ranging from magnetically targeted drug delivery systems to compact, high power density electric motors/generators. At such high fields, however, the electromagnetic stresses that develop within the superconductors as a result of the Lorentz force can cause mechanical failure of these brittle materials, as analytical solutions have predicted inherent tensile hoop stresses of up to 28 MPa and 113 MPa at trapped fields of 10 T and 20 T, respectively. Mechanical failure usually leads to an abrupt, irreversible drop in the performance of these trapped field magnets. Therefore, the mechanical properties of bulk (RE)BCO need to be studied comprehensively and techniques for improving these properties need to be established for the continued technical development of these materials.

In this study, the mechanical behaviour of single-grain (RE)BCO bulk superconductors has been characterised using in-situ and ex-situ techniques. The three-point bend and the Brazilian tests were applied to batches of nominally identical YBCO single grains at room temperature. Bend test beams were cut from 25 mm diameter single-grain YBCO, which allowed the inherent spatial distribution of flexural strength to be determined. The results showed fracture strength is lowest at the centre of the bulk samples, but also increases gradually with distance from the seed crystal. These observations are consistent with the intrinsic variation in single grain microstructure since, firstly, high porosity is typically observed at the centre of the samples, which decreases the strength significantly as pores represent stress concentration sites that initiate cracks and promote failure. Secondly, RE-211 particle density normally increases in both the *ab-* and *c*-directions as a function of distance from the seed, which increases the strength at a given position due to improved fracture toughness. The Brazilian test was

subsequently used to determine the bulk-to-bulk scatter in tensile strength in 16 mm diameter single-grain YBCO discs. Analysis of the indirect tensile strengths revealed a Weibull modulus of 10.1, which indicates a narrow scatter from sample to sample despite the pronounced spatial distribution within each single grain. Reproducible, and therefore predictable, failure should be considered beneficial to the widespread use of these materials. Additionally, the indirect tensile strengths of YBCO ranged from 19.5 MPa to 26.0 MPa, which were in closer agreement with the 25 MPa estimate of sample strength derived directly from magnetisation measurements. In comparison, the three-point bend test data varied more widely, from 40.2 MPa to 76.2 MPa.

In addition to tests carried out on un-magnetised (RE)BCO bulk specimens in a tensile testing machine, the mechanical behaviour of a bulk superconductor during magnetisation was also observed directly. In-situ measurement of the pinning-induced strain was achieved using cryogenic strain gauges attached to the surface of a 40 mm diameter GdBCO/Ag bulk superconductor, which was part of a two-sample stack. A comprehensive picture of the strain and stress evolution was determined by measuring the hoop and radial strains at multiple positions along the sample radius as the stack was field cooled in 6 T to 9.6 T at 64 K. The two-sample stack was then modelled using the finite element method, first by assuming a homogeneous material and taking into account the experimentally determined $J_c(B)$ instead of using a constant J_c. The experimental strains were similar in magnitude to the simulation results, but the strain evolution exhibited significantly different profiles as the external field was ramped down. Further investigation showed that in order to model large (RE)BCO single grains more accurately, the realistic inhomogeneity in the superconducting and mechanical properties, which arise from the top seeded melt growth process, need to be considered. In the present study, the spatial variation of the critical current density and Young's modulus within the GdBCO/Ag single grain, which were determined empirically from representative samples, were incorporated. Consequently, closer agreement was achieved in terms of the trapped field and electromagnetic strains. Another key finding from the study was that the maximum strains and stresses experienced during field cooling actually do not increase further with increasing applied field when the applied field is sufficiently high to magnetise the sample fully. This was not predicted by analytical solutions and means a maximum hoop stress exists for a given sample and operating temperature, making it easier to design mechanical reinforcements for a system once the operating conditions and target performance are known.

Pre- and post-melt processing techniques were considered for reinforcing single-grain (RE)BCO bulk superconductors. 26 mm diameter YBCO samples grown with artificial holes were characterised using the Brazilian test to illustrate the enhancement that can be made to the intrinsic strength of YBCO single grains by simply patterning an array of holes into the precursor pellets prior to melt processing. This technique reduces the effective wall thickness, allowing oxygen produced during melt growth to escape from the interior of the partially decomposed sample. The fully-grown thin-wall samples had an average tensile strength of 27.3 MPa (when the columnar holes were filled with Stycast epoxy resin) compared to 14.1 MPa for the standard hole-free YBCO single grains grown under similar conditions. According to analytical solutions, the increase in tensile strength by 93 % should improve the trapped field capability by 39 %. The enhancement in strength was then validated using high-field magnetisation experiments targeted at deliberately fracturing the samples under the Lorentz force. The standard YBCO sample failed when magnetised with 10 T at 35 K, suffering permanent damage. As a result, the standard YBCO could only trap a maximum surface field of 7.6 T without failure. On the other hand, the thin-wall YBCO sample survived all magnetisation cycles, including an applied field of 11.5 T at 35 K (the maximum field that can be applied with the facilities available), demonstrating the ability to withstand significantly higher electromagnetic stresses. The thin-wall sample achieved, in the process, a surface trapped field of 8.8 T at 30 K without any external ring reinforcement. Another advantage of the thin-wall geometry is that the artificial holes can be filled using materials with high thermal conductivity and heat capacity, which can help to mitigate flux jumps and generally enable the overall properties of the bulk sample to be engineered.

Finally, a straight-forward post melt processing treatment was proposed in order to improve the mechanical reliability and thermal stability of as-grown and as-annealed (RE)BCO single-grain bulk superconductors. The design was selected with the help of numerical simulations and then implemented experimentally. This composite approach involved laminating the as-manufactured samples with stainless steel sheets approximately 0.5 mm in thickness and enclosing the laminated structure in shrink-fit stainless-steel rings approximately 2.5 mm in wall thickness in order to generate compressive pre-stress. The first composite stack, fabricated from 24 mm diameter GdBCO/Ag discs, successfully trapped 16.8 T at 26 K in the first magnetisation cycle followed by 17.6 T at 22.5 K in the second cycle. These results are significant as this was the first report of a (RE)BCO bulk stack that survived repeated magnetisation with an external field as high as 18 T. Furthermore, 17.6 T matched the highest

trapped field reported to date, which had only been achieved once previously, despite several attempts by research groups worldwide to replicate or exceed this value. Two more composite stacks were manufactured and measured subsequently, and both achieved trapped fields of around 16 T in their initial magnetisation cycles, exhibiting a high degree of repeatability and reliability with this reinforcement approach.

To summarise, this study has identified and applied experimental procedures to determine the mechanical properties and the pinning-induced deformation behaviour of two commonly encountered single-grain bulk superconductor systems, namely YBCO and GdBCO/Ag. The procedures can be expanded and applied easily to other (RE)BCO systems, such as SmBCO or YBCO grown by other melt processes, including top seeded infiltration and growth (TSIG). Additionally, this work has established two validated techniques for mechanically and thermally reinforcing existing (RE)BCO systems to improve their ability to survive high magnetisation fields, and therefore improve their trapped field performance and suitability for a variety of potential engineering applications.

7.2.   Future research

The mechanical characterisation and reinforcement investigations carried out in this study have generated some interesting results which, in combination with the present challenges regarding the commercial and industrial uses of single-grain (RE)BCO bulk superconductors, can form the foundation of a number of subsequent topics encompassing computational and experimental research.

Firstly, strength and Young's modulus data from the mechanical tests could be fed back into the sample growth process to produce samples with a higher overall strength and more homogeneous strength distribution. This can be approached by, for example, decreasing the maximum porosity, increasing the uniformity and concentration of RE-211 particles and employing dopants in the single grain microstructure. Furthermore, while local strength has been shown to correlate with the local porosity and RE-211 content in this study, more parameters may be involved in determining the spatial distribution of mechanical properties within single grains. An example of this may be the residual stresses that manifest from the solidification and subsequent cooling of single grains from the growth window at approximately 1000 °C to room temperature. Residual stresses develop during this part of the

fabrication process as a result of the various phases possessing different thermal expansion coefficients, and therefore contracting by different amounts when cooled. This would then place certain regions within the microstructure under greater tension and promote failure at these positions. Finite element analysis could be used to investigate the interaction between different phases within the microstructure. Additionally, alternative testing techniques could be explored for determining mechanical properties and for reproducing the results in Chapters 3 and 4, and to obtain further information on the material. An example could be applying the Oliver-Pharr method to nanoindentation testing to determine the hardness and elastic modulus of the material from the load–displacement curves measured. Since a large number of indentations can be performed on a bulk sample, this method allows the spatial distribution of hardness and modulus to be mapped extensively.

Secondly, strain could be measured during pulsed field magnetisation (PFM) given that PFM is a more practical charging technique than field cooled magnetisation with regards to practical applications involving high magnetic fields. Preliminary attempts at measuring strain during PFM showed that conventional strain gauges likely would not be suitable due to the large, induced voltages in the metallic foil and insufficient time resolution of the current measurement apparatus, as samples are subject to pulsed fields of up to 5 T with a rise time less than 0.1 s and a decay time less than 1 s. However, alternative techniques discussed in this dissertation, such as fibre Bragg gratings and digital image correlation, could be viable alternatives. An advantage of digital image correlation is that the whole surface of the bulk superconductor could be characterised, providing a comprehensive picture of the evolution of stress and strain across the entire superconductor disc and revealing differences in behaviour between growth sectors and growth sector boundaries.

Thirdly, bulk superconductors fabricated with artificial holes could be investigated in greater detail, again with a particular focus on practical applications. The present study has shown that thin-wall YBCO is stronger mechanically and traps a larger magnetic field than standard YBCO when field-cooled. It would be useful to compare the trapped field performance of thin-wall samples with those of standard samples when pulsed field magnetised. Unique hole patterns could be employed, and high thermal conductivity materials could be used to fill the artificial holes, in order to assist with heat dissipation from the superconducting material during PFM and to engineer the thermal time constant of the system. This, in turn, could lead to the generation of higher and more consistent trapped fields in the context of PFM.

Fourthly, investigations should be carried out to determine whether the mechanical properties or the thermal properties dominate sample failure during magnetisation at low temperature. Since brittle fracture and flux avalanche/jump are both normally observed during the failure of a (RE)BCO single grain, it is difficult to deduce which type of failure actually triggers the cascade. An understanding of the order of failures would be highly useful to future reinforcement work. Systematic studies involving the use of different ramp rates for a fixed magnetising field could provide valuable insight.

Finally, the composite bulk superconductor design proposed in Chapter 6 could be further optimised in terms of the thickness of the stainless-steel sheets, the lamination material and the bonding material used, to maximise the mechanical reinforcement provided. The experimental parameters used in the high-field magnetisation process, such as the field ramp rate, could also be further optimised, i.e. by implementing a different ramp rate for each field range based on the heat generated, to minimise the occurrence of thermomagnetic instabilities and to minimise thermal stresses. The composite GdBCO/Ag bulk stack approach has yielded highly encouraging results so far and further research may help single-grain (RE)BCO bulk superconductors achieve trapped fields of over 20 T reliably in the near future, which will have profound implications for the application of these technologically important materials.

References

[1] J. G. Bednorz and K. A. Müller, "Possible High Tc Superconductivity in the Ba−La−Cu−O System," *Zeitschrift für Phys. B Condens. Matter*, vol. 64, no. 2, pp. 189–193, 1986.

[2] J. R. Gavaler, M. A. Janocko, and C. K. Jones, "Preparation and properties of high-Tc Nb-Ge films," *J. Appl. Phys.*, vol. 45, no. 7, pp. 3009–3013, 1974.

[3] M.-K. Wu *et al.*, "Superconductivity at 93 K in a New Mixed-Phase Y-Ba-Cu-O Compound System at Ambient Pressure," *Phys. Rev. Lett.*, vol. 58, no. 9, p. 908, 1987.

[4] H. Maeda, Y. Tanaka, M. Fukutomi, and T. Asano, "A New High-Tc Oxide Superconductor without a Rare Earth Element," *Jpn. J. Appl. Phys.*, vol. 27, no. 2A, p. L209, 1988.

[5] I. K. Gopalakrishnan, P. Sastry, K. Gangadharan, G. M. Phatak, J. V Yakhmi, and R. M. Iyer, "Synthesis and properties of a 125 K superconductor in the Tl-Ca-Ba-Cu-O system," *Appl. Phys. Lett.*, vol. 53, no. 5, pp. 414–416, 1988.

[6] L. Gao *et al.*, "Superconductivity up to 164 K in HgBa2Cam−1CumO2m+2+δ (m= 1, 2, and 3) under quasihydrostatic pressures," *Phys. Rev. B*, vol. 50, no. 6, p. 4260, 1994.

[7] M. Tomita and M. Murakami, "High-temperature superconductor bulk magnets that can trap magnetic fields of over 17 tesla at 29 K," *Nature*, vol. 421, no. 6922, p. 517, 2003.

[8] J. H. Durrell *et al.*, "A trapped field of 17.6 T in melt-processed, bulk Gd-Ba-Cu-O reinforced with shrink-fit steel," *Supercond. Sci. Technol.*, vol. 27, no. 8, p. 82001, 2014.

[9] J. H. Durrell *et al.*, "Bulk superconductors: a roadmap to applications," *Supercond. Sci. Technol.*, vol. 31, no. 10, p. 103501, 2018.

[10] P. J. McGinn, W. Chen, and M. A. Black, "Texture processing of bulk YBa2Cu3O6+x by zone melting," *Phys. C Supercond.*, vol. 161, no. 2, pp. 198–204, 1989.

[11]   F. Yu, K. W. White, and R. Meng, "Mechanical characterization of top-seeded melt-textured YBa2Cu3O7−δ single crystal," *Phys. C Supercond.*, vol. 276, no. 3–4, pp. 295–308, 1997.

[12]   E. S. Reddy and T. Rajasekharan, "Effect of content on the macro-defect structure of melt processed superconductor," *Supercond. Sci. Technol.*, vol. 11, no. 2, p. 183, 1998.

[13]   C.-J. Kim and G.-W. Hong, "Defect formation, distribution and size reduction of Y2BaCuO5 in melt-processed YBCO superconductors," *Supercond. Sci. Technol.*, vol. 12, no. 3, p. R27, 1999.

[14]   G. Fuchs *et al.*, "High trapped fields in bulk YBa2Cu3O7−δ samples at temperatures around 50 K," *Appl. Phys. Lett.*, vol. 70, no. 1, pp. 117–119, 1997.

[15]   H. Kamerlingh Onnes, "The resistance of pure mercury at helium temperatures," *Commun. Phys. Lab. Univ. Leiden, b*, vol. 120, 1911.

[16]   H. Kamerlingh Onnes, "The sudden disappearance of the ordinary resistance of tin, and the super-conductive state of lead," *Commun. Phys. Lab. Univ. Leiden, d*, vol. 133, 1913.

[17]   W. Meissner and R. Ochsenfeld, "Ein neuer effekt bei eintritt der supraleitfähigkeit," *Naturwissenschaften*, vol. 21, no. 44, pp. 787–788, 1933.

[18]   A. Bussmann-Holder and H. Keller, "High-temperature superconductors: underlying physics and applications," *Zeitschrift für Naturforsch. B*, vol. 75, no. 1–2, pp. 3–14, 2020.

[19]   MIT, "Lecture 17: Type II Superconductors," *Massachusetts Institute of Technology 6.763 2003 Lecture 17*, 2003. [Online]. Available: http://web.mit.edu/6.763/www/FT03/Lectures/Lecture17.pdf. [Accessed: 23-Apr-2020].

[20]   F. London and H. London, "The electromagnetic equations of the supraconductor," *Proc. R. Soc. London. Ser. A-Mathematical Phys. Sci.*, vol. 149, no. 866, pp. 71–88, 1935.

[21]   A. B. Pippard and W. L. Bragg, "An experimental and theoretical study of the relation between magnetic field and current in a superconductor," *Proc. R. Soc. London. Ser. A.*

Math. Phys. Sci., vol. 216, no. 1127, pp. 547–568, 1953.

[22]   V. L. Ginzburg and L. D. Landau, ".," *Zh. Eksp. Teor. Fiz*, vol. 20, no. 1064, p. 1950, 1950.

[23]   R. A. Dunlap, *Electrons in Solids: Contemporary Topics*. Morgan & Claypool Publishers, 2019.

[24]   C. Kittel, *Introduction to Solid State Physics*, vol. 8. Wiley New York, 1976.

[25]   P. Seidel, M. Grajcar, A. Plecenik, and R. Hlubina, "Superconducting parameters of YBCO and BSCCO from 'tunneling'spectroscopy," *Phys. B Condens. Matter*, vol. 218, no. 1–4, pp. 224–227, 1996.

[26]   A. A. Abrikosov, "On the magnetic properties of superconductors of the second group," *Sov. Phys. JETP*, vol. 5, pp. 1174–1182, 1957.

[27]   A. C. Rose-Innes, A. C. I. Rose, E. H. Rhoderick, and R. E. H, *Introduction to Superconductivity*. Pergamon Press, 1978.

[28]   Hanaguri, "SPM Sample Images - STM Topographic Image of Vortex Lattice of a Superconductor NbSe2," *Magnetic Materials Laboratory, RIKEN*. [Online]. Available: http://www.unisoku.com/products/SPMSampleImage.html. [Accessed: 24-Apr-2020].

[29]   M. Murakami, *Melt processed high-temperature superconductors*, vol. 9. World Scientific, 1992.

[30]   M. Murakami, "Processing of bulk YBaCuO," *Supercond. Sci. Technol.*, vol. 5, no. 4, p. 185, 1992.

[31]   C. P. Bean, "Magnetization of hard superconductors," *Phys. Rev. Lett.*, vol. 8, no. 6, p. 250, 1962.

[32]   Y. B. Kim, C. F. Hempstead, and A. R. Strnad, "Critical persistent currents in hard superconductors," *Phys. Rev. Lett.*, vol. 9, no. 7, p. 306, 1962.

[33]   P. W. Anderson, "Theory of flux creep in hard superconductors," *Phys. Rev. Lett.*, vol. 9, no. 7, p. 309, 1962.

[34] D. Chen and R. B. Goldfarb, "Kim model for magnetization of type-II superconductors," *J. Appl. Phys.*, vol. 66, no. 6, pp. 2489–2500, 1989.

[35] R. J. Cava *et al.*, "Bulk superconductivity at 91 K in single-phase oxygen-deficient perovskite Ba2YCu3O9−δ," *Phys. Rev. Lett.*, vol. 58, no. 16, p. 1676, 1987.

[36] J. Nagamatsu, N. Nakagawa, T. Muranaka, Y. Zenitani, and J. Akimitsu, "Superconductivity at 39 K in magnesium diboride," *Nature*, vol. 410, no. 6824, pp. 63–64, 2001.

[37] Y. Kamihara *et al.*, "Iron-based layered superconductor: LaOFeP," *J. Am. Chem. Soc.*, vol. 128, no. 31, pp. 10012–10013, 2006.

[38] A. Extance, "The race is on to make the first room temperature superconductor," *CHEMISTRYWORLD*, 2019. [Online]. Available: https://www.chemistryworld.com/news/the-race-is-on-to-make-the-first-room-temperature-superconductor/4010591.article. [Accessed: 26-Apr-2020].

[39] A. M. Campbell and D. A. Cardwell, "Bulk high temperature superconductors for magnet applications," *Cryogenics (Guildf).*, vol. 37, no. 10, pp. 567–575, 1997.

[40] J. W. Ekin *et al.*, "Evidence for weak link and anisotropy limitations on the transport critical current in bulk polycrystalline Y1Ba2Cu3Ox," *J. Appl. Phys.*, vol. 62, no. 12, pp. 4821–4828, 1987.

[41] D. C. Larbalestier *et al.*, "Weak links and the poor transport critical currents of the 123 compounds," *Phys. C Supercond.*, vol. 153, pp. 1580–1585, 1988.

[42] D. Dimos, P. Chaudhari, J. Mannhart, and F. K. LeGoues, "Orientation Dependence of Grain-Boundary Critical Currents in YBa2Cu3O7−δ Bicrystals," *Phys. Rev. Lett.*, vol. 61, no. 2, p. 219, 1988.

[43] Y. Shiohara and A. Endo, "Crystal growth of bulk high-Tc superconducting oxide materials," *Mater. Sci. Eng. R Reports*, vol. 19, no. 1–2, pp. 1–86, 1997.

[44] H. Hosono, A. Yamamoto, H. Hiramatsu, and Y. Ma, "Recent advances in iron-based superconductors toward applications," *Mater. today*, vol. 21, no. 3, pp. 278–302, 2018.

[45] G. Fuchs *et al.*, "High trapped fields in bulk MgB2 prepared by hot-pressing of ball-milled precursor powder," *Supercond. Sci. Technol.*, vol. 26, no. 12, p. 122002, 2013.

[46] J. D. Weiss, A. Yamamoto, A. A. Polyanskii, R. B. Richardson, D. C. Larbalestier, and E. E. Hellstrom, "Demonstration of an iron-pnictide bulk superconducting magnet capable of trapping over 1 T," *Supercond. Sci. Technol.*, vol. 28, no. 11, p. 112001, 2015.

[47] L. Civale *et al.*, "Angular-dependent vortex pinning mechanisms in YBa2Cu3O7 coated conductors and thin films," *Appl. Phys. Lett.*, vol. 84, no. 12, pp. 2121–2123, 2004.

[48] A. Xu *et al.*, "Angular dependence of Jc for YBCO coated conductors at low temperature and very high magnetic fields," *Supercond. Sci. Technol.*, vol. 23, no. 1, p. 14003, 2009.

[49] D. A. Cardwell and N. H. Babu, "Processing and properties of single grain (RE)–Ba–Cu–O bulk superconductors," *Phys. C Supercond. its Appl.*, vol. 445, pp. 1–7, 2006.

[50] M. Ainslie and H. Fujishiro, *Numerical Modelling of Bulk Superconductor Magnetisation*. IOP Publishing, 2019.

[51] J. V. J. Congreve, Y. H. Shi, A. R. Dennis, J. H. Durrell, and D. A. Cardwell, "Microstructure and Composition of Primary and Recycled Single Grains of YBCO, Gd BCO-Ag, and Sm BCO-Ag Bulk Superconductors," *J. Am. Ceram. Soc.*, vol. 99, no. 9, pp. 3111–3119, 2016.

[52] Y. Shi, N. H. Babu, and D. A. Cardwell, "Development of a generic seed crystal for the fabrication of large grain (RE)–Ba–Cu–O bulk superconductors," *Supercond. Sci. Technol.*, vol. 18, no. 4, p. L13, 2005.

[53] H. Fujishiro, T. Tateiwa, A. Fujiwara, T. Oka, and H. Hayashi, "Higher trapped field over 5 T on HTSC bulk by modified pulse field magnetizing," *Phys. C Supercond. its Appl.*, vol. 445, pp. 334–338, 2006.

[54] J. R. Hull and M. Murakami, "Applications of bulk high-temperature superconductors," *Proc. IEEE*, vol. 92, no. 10, pp. 1705–1718, 2004.

[55] M. Murakami, N. Sakai, T. Higuchi, and S. I. Yoo, "Melt-processed light rare earth element-Ba-Cu-O," *Supercond. Sci. Technol.*, vol. 9, no. 12, p. 1015, 1996.

[56] Z. Deng *et al.*, "A high-temperature superconducting Maglev-evacuated tube transport (HTS Maglev-ETT) test system," *IEEE Trans. Appl. Supercond.*, vol. 27, no. 6, pp. 1–8, 2017.

[57] L. Schultz *et al.*, "Superconductively levitated transport system-the SupraTrans project," *IEEE Trans. Appl. Supercond.*, vol. 15, no. 2, pp. 2301–2305, 2005.

[58] M. Strasik *et al.*, "An overview of Boeing flywheel energy storage systems with high-temperature superconducting bearings," *Supercond. Sci. Technol.*, vol. 23, no. 3, p. 34021, 2010.

[59] H. Matsuzaki *et al.*, "An axial gap-type HTS bulk synchronous motor excited by pulsed-field magnetization with vortex-type armature copper windings," *IEEE Trans. Appl. Supercond.*, vol. 15, no. 2, pp. 2222–2225, 2005.

[60] M. Miki *et al.*, "Development of a synchronous motor with Gd–Ba–Cu–O bulk superconductors as pole-field magnets for propulsion system," *Supercond. Sci. Technol.*, vol. 19, no. 7, p. S494, 2006.

[61] T. Oka *et al.*, "Study on magnetic separation system using high Tc superconducting bulk magnets for water purification technique," in *Journal of Physics: Conference Series*, 2009, vol. 156, no. 1, p. 12031.

[62] T. Nakamura *et al.*, "Development of a superconducting bulk magnet for NMR and MRI," *J. Magn. Reson.*, vol. 259, pp. 68–75, 2015.

[63] J. O'Callaghan, "It may look like a toy track but this is the future of train travel, says China. SUPER-MAGLEV could one day go up to 1,800MPH," *Urban transport*, 2014. [Online]. Available: https://www.dailymail.co.uk/sciencetech/article-2622516/Forget-high-speed-rail-future-train-travel-SUPER-MAGLEV-says-China-one-day-1-800MPH.html. [Accessed: 27-Apr-2020].

[64] T. Oka, "Processing and applications of bulk HTSC," *Phys. C Supercond. its Appl.*, vol. 463, pp. 7–13, 2007.

[65] Z. Y. Zhang, S. Matsumoto, R. Teranishi, and T. Kiyoshi, "Magnetic field, temperature and mechanical crack performance of a GdBCO magnetic lens," *Supercond. Sci.*

Technol., vol. 25, no. 11, p. 115012, 2012.

[66] K. Takahashi, H. Fujishiro, and M. D. Ainslie, "A new concept of a hybrid trapped field magnet lens," *Supercond. Sci. Technol.*, vol. 31, no. 4, p. 44005, 2018.

[67] Y. Ren, R. Weinstein, J. Liu, R. P. Sawh, and C. Foster, "Damage caused by magnetic pressure at high trapped field in quasi-permanent magnets composed of melt-textured Y-Ba-Cu-O superconductor," *Phys. C Supercond.*, vol. 251, no. 1–2, pp. 15–26, 1995.

[68] T. H. Johansen, "Flux-pinning-induced stress and magnetostriction in bulk superconductors," *Supercond. Sci. Technol.*, vol. 13, no. 10, p. R121, 2000.

[69] M. E. Launey and R. O. Ritchie, "On the fracture toughness of advanced materials," *Adv. Mater.*, vol. 21, no. 20, pp. 2103–2110, 2009.

[70] C. E. Inglis, "Stresses in a plate due to the presence of cracks and sharp corners," *Trans Inst Nav. Arch.*, vol. 55, pp. 219–241, 1913.

[71] A. A. Griffith, "VI. The phenomena of rupture and flow in solids," *Philos. Trans. R. Soc. london. Ser. A, Contain. Pap. a Math. or Phys. character*, vol. 221, no. 582–593, pp. 163–198, 1921.

[72] G. R. Irwin, "Analysis of stresses and strains near the end of a crack transversing a plate," *Trans. ASME, Ser. E, J. Appl. Mech.*, vol. 24, pp. 361–364, 1957.

[73] D. W. Richerson, *Modern ceramic engineering: properties, processing, and use in design*. CRC press, 2005.

[74] Y. Shi, M. Gough, A. R. Dennis, J. H. Durrell, and D. A. Cardwell, "Distribution of the superconducting critical current density within a Gd–Ba–Cu–O single grain," *Supercond. Sci. Technol.*, vol. 33, no. 4, p. 44009, 2020.

[75] G. Krabbes, G. Fuchs, W.-R. Canders, H. May, and R. Palka, *High temperature superconductor bulk materials: fundamentals, processing, properties control, application aspects*. John Wiley & Sons, 2006.

[76] N. M. Alford, J. D. Birchall, W. J. Clegg, M. A. Harmer, K. Kendall, and D. H. Jones, "Physical and mechanical properties of YBa2Cu3O7-δ superconductors," *J. Mater. Sci.*,

vol. 23, no. 3, pp. 761–768, 1988.

[77] F. P. Knudsen, "Dependence of mechanical strength of brittle polycrystalline specimens on porosity and grain size," *J. Am. Ceram. Soc.*, vol. 42, no. 8, pp. 376–387, 1959.

[78] N. Qunhui, L. Anping, L. Yong, and K. Qingping, "Deformation and fracture of Y-Ba-Cu-O superconductor," *Chinese Phys. Lett.*, vol. 6, no. 7, p. 321, 1989.

[79] A. P. Li, Q. H. Ni, and Q. P. Kong, "Mechanical properties of Ag-doped YBa2Cu3O7−y superconductors," *Phys. status solidi*, vol. 127, no. 1, pp. 187–193, 1991.

[80] N. Sakai, S. J. Seo, K. Inoue, T. Miyamoto, and M. Murakami, "Mechanical properties of RE–Ba–Cu–O bulk superconductors," *Phys. C Supercond.*, vol. 335, no. 1–4, pp. 107–111, 2000.

[81] A. Goyal, W. C. Oliver, P. D. Funkenbusch, D. M. Kroeger, and S. J. Burns, "Mechanical properties of highly aligned YBa2Cu3O7−δ. Effect of Y2BaCuOx particles," *Phys. C Supercond.*, vol. 183, no. 4–6, pp. 221–233, 1991.

[82] A. Goyal, P. D. Funkenbusch, D. M. Kroeger, and S. J. Burns, "Anisotropic hardness and fracture toughness of highly aligned YBa2Cu3O7−δ," *J. Appl. Phys.*, vol. 71, no. 5, pp. 2363–2367, 1992.

[83] H. Fujimoto, M. Murakami, and N. Koshizuka, "Effect of Y2BaCuO5 on fracture toughness of YBCO prepared by a MPMG process," *Phys. C Supercond.*, vol. 203, no. 1–2, pp. 103–110, 1992.

[84] A. Leenders, M. Mich, and H. C. Freyhard, "Influence of thermal cycling on the mechanical properties of VGF melt-textured YBCO," *Phys. C Supercond.*, vol. 279, no. 3–4, pp. 173–180, 1997.

[85] M. Tomita, M. Murakami, and K. Katagiri, "Reliability of mechanical properties for bulk superconductors with resin impregnation," *Phys. C Supercond.*, vol. 378, pp. 783–787, 2002.

[86] H. Fujimoto, "Flexural strength of melt-processed Y–Ba–Cu–O bulk superconductors with Ag addition measured at 77 K," *Supercond. Sci. Technol.*, vol. 16, no. 9, p. 1115, 2003.

[87]   T. Okudera *et al.*, "Fracture toughness evaluation of YBCO bulk superconductor," *Phys. C Supercond.*, vol. 392, pp. 628–633, 2003.

[88]   K. Katagiri *et al.*, "Tensile and bending mechanical properties of bulk superconductors at room temperature," *Phys. C Supercond.*, vol. 412, pp. 633–637, 2004.

[89]   A. Murakami *et al.*, "Low temperature mechanical properties of Y123 bulk superconductor fabricated by the modified QMG process," *Phys. C Supercond.*, vol. 412, pp. 673–677, 2004.

[90]   S. Nariki, N. Sakai, M. Murakami, and I. Hirabayashi, "Effects of Dy2BaCuO5 contents on microstructure and mechanical strength of Ag-added Dy–Ba–Cu–O bulk superconductors," *Phys. C Supercond.*, vol. 412, pp. 651–656, 2004.

[91]   H. Fujimoto and A. Murakami, "Mechanical properties of Gd123 superconducting bulks at 77 K," *Supercond. Sci. Technol.*, vol. 25, no. 5, p. 54017, 2012.

[92]   K. Konstantopoulou, Y. H. Shi, A. R. Dennis, J. H. Durrell, J. Y. Pastor, and D. A. Cardwell, "Mechanical characterization of GdBCO/Ag and YBCO single grains fabricated by top-seeded melt growth at 77 and 300 K," *Supercond. Sci. Technol.*, vol. 27, no. 11, p. 115011, 2014.

[93]   A. Murakami, K. Katagiri, H. Miyata, K. Kasaba, and Y. Shoji, "Distribution of mechanical properties in a single-grain Sm123 bulk superconductor at liquid nitrogen temperature," *IEEE Trans. Appl. Supercond.*, vol. 16, no. 2, pp. 1003–1006, 2006.

[94]   A. Murakami, H. Teshima, M. Morita, and A. Iwamoto, "Distribution of mechanical properties in large single-grained RE–Ba–Cu–O bulk 150 mm in diameter fabricated using RE compositional gradient technique," *Phys. C Supercond. its Appl.*, vol. 496, pp. 44–48, 2014.

[95]   A. Murakami and A. Iwamoto, "Mechanical properties of EuBaCuO superconducting bulk material at liquid nitrogen temperature," in *J. Phys.: Conf. Ser.*, 2017, vol. 871.

[96]   A. Murakami *et al.*, "Mechanical properties of Gd123 bulk superconductors at room temperature," *Cryogenics (Guildf).*, vol. 43, no. 6, pp. 345–350, 2003.

[97]   A. Murakami, H. Fujimoto, and A. Iwamoto, "Fracture strength properties of Gd-Ba-

Cu-O large single-grain bulk with CeO2 addition," *Phys. Procedia*, vol. 27, pp. 160–163, 2012.

[98] Y. L. Chen, H. M. Chan, M. P. Harmer, V. R. Todt, S. Sengupta, and D. Shi, "A new method for net-shape forming of large, single-domain YBa2Cu3O6+x," *Phys. C Supercond.*, vol. 234, no. 3–4, pp. 232–236, 1994.

[99] K. Iida, N. H. Babu, Y. Shi, and D. A. Cardwell, "Seeded infiltration and growth of large, single domain Y–Ba–Cu–O bulk superconductors with very high critical current densities," *Supercond. Sci. Technol.*, vol. 18, no. 11, p. 1421, 2005.

[100] D. K. Namburi, Y. Shi, K. G. Palmer, A. R. Dennis, J. H. Durrell, and D. A. Cardwell, "An improved top seeded infiltration growth method for the fabrication of Y–Ba–Cu–O bulk superconductors," *J. Eur. Ceram. Soc.*, vol. 36, no. 3, pp. 615–624, 2016.

[101] F. Carneiro, "A new method to determine the tensile strength of concrete," in *Proceedings of the 5th meeting of the Brazilian Association for Technical Rules*, 1943, vol. 3, no. 16, pp. 126–129.

[102] G. Hondros, "The evaluation of Poisson's ratio and the modulus of materials of low tensile resistance by the Brazilian (indirect tensile) test with particular reference to concrete," *Aust. J. Appl. Sci.*, vol. 10, no. 3, pp. 243–268, 1959.

[103] C. Fairhurst, "On the validity of the 'Brazilian' test for brittle materials," in *International Journal of Rock Mechanics and Mining Sciences & Geomechanics Abstracts*, 1964, vol. 1, no. 4, pp. 535–546.

[104] D. Li and L. N. Y. Wong, "The Brazilian disc test for rock mechanics applications: review and new insights," *Rock Mech. rock Eng.*, vol. 46, no. 2, pp. 269–287, 2013.

[105] L. Reinking, "Examples of Image Analysis Using ImageJ," 2007. [Online]. Available: https://imagej.nih.gov/ij/docs/pdfs/examples.pdf. [Accessed: 22-Jun-2020].

[106] W. Lo and D. A. Cardwell, "Investigation of the controlled growth of large undoped and Pt-containing YBCO pseudo-crystals," *Mater. Sci. Eng. B*, vol. 53, no. 1–2, pp. 45–53, 1998.

[107] R. Cloots, T. Koutzarova, J. P. Mathieu, and M. Ausloos, "From RE-211 to RE-123.

How to control the final microstructure of superconducting single-domains," *Supercond. Sci. Technol.*, vol. 18, no. 3, p. R9, 2004.

[108] A. Endo, H. S. Chauhan, T. Egi, and Y. Shiohara, "Macrosegregation of Y2Ba1Cu1O5 particles in Y1Ba2Cu3O7−δ crystals grown by an undercooling method," *J. Mater. Res.*, vol. 11, no. 4, pp. 795–803, 1996.

[109] P. Diko, "Growth-related microstructure of melt-grown REBa2Cu3Oy bulk superconductors," *Supercond. Sci. Technol.*, vol. 13, no. 8, p. 1202, 2000.

[110] J. Seidel, N. Claussen, and J. Rödel, "Reliability of alumina ceramics: effect of grain size," *J. Eur. Ceram. Soc.*, vol. 15, no. 5, pp. 395–404, 1995.

[111] K. O. Hill, Y. Fujii, D. C. Johnson, and B. S. Kawasaki, "Photosensitivity in optical fiber waveguides: Application to reflection filter fabrication," *Appl. Phys. Lett.*, vol. 32, no. 10, pp. 647–649, 1978.

[112] K. O. Hill and G. Meltz, "Fiber Bragg grating technology fundamentals and overview," *J. Light. Technol.*, vol. 15, no. 8, pp. 1263–1276, 1997.

[113] P. E. Anuta, "Spatial registration of multispectral and multitemporal digital imagery using fast Fourier transform techniques," *IEEE Trans. Geosci. Electron.*, vol. 8, no. 4, pp. 353–368, 1970.

[114] T. J. Keating, P. R. Wolf, and F. L. Scarpace, "An improved method of digital image correlation," *Photogramm. Eng. Remote Sensing*, vol. 41, no. 8, pp. 993–1002, 1975.

[115] W. H. Peters and W. F. Ranson, "Digital imaging techniques in experimental stress analysis," *Opt. Eng.*, vol. 21, no. 3, p. 213427, 1982.

[116] T. C. Chu, W. F. Ranson, and M. A. Sutton, "Applications of digital-image-correlation techniques to experimental mechanics," *Exp. Mech.*, vol. 25, no. 3, pp. 232–244, 1985.

[117] I. Latka, T. Habisreuther, and M. Zeisberger, "Fiber Bragg grating based spatially resolved characterization of flux-pinning-induced strain of disk-shaped bulk YBCO samples," *Cryogenics (Guildf).*, vol. 49, no. 7, pp. 340–345, 2009.

[118] M. Zeisberger, I. Latka, W. Ecke, T. Habisreuther, D. Litzkendorf, and W. Gawalek,

"Measurement of the thermal expansion of melt-textured YBCO using optical fibre grating sensors," *Supercond. Sci. Technol.*, vol. 18, no. 2, p. S202, 2005.

[119] T. Miyamoto, K. Nagashima, N. Sakai, and M. Murakami, "Mechanical properties of bulk superconductors," *Supercond. Sci. Technol.*, vol. 13, no. 6, p. 816, 2000.

[120] T. Miyamoto, K. Nagashima, N. Sakai, and M. Murakami, "Direct measurements of mechanical properties for large-grain bulk superconductors," *Phys. C Supercond.*, vol. 340, no. 1, pp. 41–50, 2000.

[121] K. Takahashi *et al.*, "Thermal and magnetic strain measurements on a REBaCuO ring bulk reinforced by a metal ring during field-cooled magnetization," *Supercond. Sci. Technol.*, vol. 32, no. 1, p. 15007, 2018.

[122] S. Namba, H. Fujishiro, T. Naito, M. D. Ainslie, and K. Y. Huang, "Electromagnetic strain measurements and two-directional mechanical stress estimation for a REBaCuO ring bulk reinforced by a metal ring during field-cooled magnetization," *Supercond. Sci. Technol.*, vol. 32, no. 12, p. 125011, 2019.

[123] M. Tsuchimoto, K. Murata, M. Iori, and Y. Itoh, "Numerical evaluation of maximum stress of a bulk superconductor in partial magnetization," *IEEE Trans. Appl. Supercond.*, vol. 14, no. 2, pp. 1122–1125, 2004.

[124] H. Fujishiro *et al.*, "Simulation studies of mechanical stresses in REBaCuO superconducting ring bulks with infinite and finite height reinforced by metal ring during field-cooled magnetization," *Supercond. Sci. Technol.*, vol. 30, no. 8, p. 85008, 2017.

[125] M. D. Ainslie *et al.*, "Numerical modelling of mechanical stresses in bulk superconductor magnets with and without mechanical reinforcement," *Supercond. Sci. Technol.*, vol. 32, no. 3, p. 34002, 2019.

[126] H. Wu, H. Yong, and Y. Zhou, "Stress analysis in high-temperature superconductors under pulsed field magnetization," *Supercond. Sci. Technol.*, vol. 31, no. 4, p. 45008, 2018.

[127] S. Nariki, N. Sakai, and M. Murakami, "Fabrication of large melt-textured Gd-Ba-Cu-O superconductor with Ag addition," *Phys. C Supercond.*, vol. 341, pp. 2409–2412,

2000.

[128] N. H. Babu, K. Iida, and D. A. Cardwell, "Flux pinning in melt-processed nanocomposite single-grain superconductors," *Supercond. Sci. Technol.*, vol. 20, no. 9, p. S141, 2007.

[129] M. D. Ainslie and H. Fujishiro, "Modelling of bulk superconductor magnetization," *Supercond. Sci. Technol.*, vol. 28, no. 5, p. 53002, 2015.

[130] M. Jirsa, L. Pust, D. Dlouhý, and M. R. Koblischka, "Fishtail shape in the magnetic hysteresis loop for superconductors: Interplay between different pinning mechanisms," *Phys. Rev. B*, vol. 55, no. 5, p. 3276, 1997.

[131] M. D. Ainslie *et al.*, "Enhanced trapped field performance of bulk high-temperature superconductors using split coil, pulsed field magnetization with an iron yoke," *Supercond. Sci. Technol.*, vol. 29, no. 7, p. 74003, 2016.

[132] M. D. Ainslie, D. Zhou, H. Fujishiro, K. Takahashi, Y. H. Shi, and J. H. Durrell, "Flux jump-assisted pulsed field magnetisation of high-Jc bulk high-temperature superconductors," *Supercond. Sci. Technol.*, vol. 29, no. 12, p. 124004, 2016.

[133] H. Mochizuki, H. Fujishiro, T. Naito, Y. Itoh, Y. Yanagi, and T. Nakamura, "Trapped field characteristics and fracture behavior of REBaCuO bulk ring during pulsed field magnetization," *IEEE Trans. Appl. Supercond.*, vol. 26, no. 4, pp. 1–5, 2015.

[134] P. Diko, G. Fuchs, and G. Krabbes, "Influence of silver addition on cracking in melt-grown YBCO," *Phys. C Supercond.*, vol. 363, no. 1, pp. 60–66, 2001.

[135] H. Fujishiro and T. Naito, "Simulation of temperature and magnetic field distribution in superconducting bulk during pulsed field magnetization," *Supercond. Sci. Technol.*, vol. 23, no. 10, p. 105021, 2010.

[136] M. R. Koblischka and M. Murakami, "Pinning mechanisms in bulk high-Tc superconductors," *Supercond. Sci. Technol.*, vol. 13, no. 6, p. 738, 2000.

[137] S. Nariki, N. Sakai, and M. Murakami, "Processing of high-performance Gd–Ba–Cu–O bulk superconductor with Ag addition," *Supercond. Sci. Technol.*, vol. 15, no. 5, p. 648, 2002.

[138] X. Chaud *et al.*, "Fabrication and characterization of thin-wall YBCO single-domain samples," *Supercond. Sci. Technol.*, vol. 19, no. 7, p. S590, 2006.

[139] X. Chaud *et al.*, "Improved magnetic trapped field in thin-wall YBCO single-domain samples by high-pressure oxygen annealing," *Mater. Sci. Eng. B*, vol. 151, no. 1, pp. 53–59, 2008.

[140] D. Zhou, S. Hara, B. Li, K. Xu, J. Noudem, and M. Izumi, "Significant improvement of trapped flux in bulk Gd–Ba–Cu–O grains fabricated by a modified top-seeded melt growth process," *Supercond. Sci. Technol.*, vol. 26, no. 1, p. 15003, 2012.

[141] G.-Z. Li, D.-J. Li, X.-Y. Deng, J.-H. Deng, and W.-M. Yang, "Infiltration growth and crystallization characterization of single-grain Y–Ba–Cu–O bulk superconductors," *Cryst. Growth Des.*, vol. 13, no. 3, pp. 1246–1251, 2013.

[142] Y. Shi, D. K. Namburi, M. Wang, J. Durrell, A. Dennis, and D. Cardwell, "A Reliable Method for Recycling (RE)-Ba-Cu-O (RE: Sm, Gd, Y) Bulk Superconductors," *J. Am. Ceram. Soc.*, vol. 98, no. 9, pp. 2760–2766, 2015.

[143] A. Murakami, H. Miyata, R. Hashimoto, K. Katagiri, and A. Iwamoto, "Evaluations of mechanical properties in Dy123 single-grain bulk superconductors with low porosity," *IEEE Trans. Appl. Supercond.*, vol. 19, no. 3, pp. 2995–2998, 2009.

[144] N. Sakai, D. Ishihara, K. Inoue, and M. Murakami, "Formation of pores in melt-processed RE–Ba–Cu–O and the techniques to reduce pore density," *Supercond. Sci. Technol.*, vol. 15, no. 5, p. 698, 2002.

[145] H.-W. Park, K.-B. Kim, K.-W. Lee, I.-H. Kuk, G.-W. Hong, and C.-J. Kim, "Sm2BaCuO5 refinement via an attrition milling and addition in Sm-Ba-Cu-O systems melt-textured at oxygen partial pressures of 0.001-1 atm," *Supercond. Sci. Technol.*, vol. 9, no. 8, p. 694, 1996.

[146] N. Sakai, A. Mase, H. Ikuta, S. J. Seo, U. Mizutani, and M. Murakami, "Mechanical properties of Sm-Ba-Cu-O/Ag bulk superconductors," *Supercond. Sci. Technol.*, vol. 13, no. 6, p. 770, 2000.

[147] N. Sakai, K. Ogasawara, K. Inoue, D. Ishihara, and M. Murakami, "Fabrication of melt-

processed RE-Ba-Cu-O bulk superconductors with high densities," *IEEE Trans. Appl. Supercond.*, vol. 11, no. 1, pp. 3509–3512, 2001.

[148] J. V. J. Congreve, Y. Shi, K. Y. Huang, A. R. Dennis, J. H. Durrell, and D. A. Cardwell, "Improving mechanical strength of YBCO bulk superconductors by addition of Ag," *IEEE Trans. Appl. Supercond.*, vol. 29, no. 5, pp. 1–5, 2019.

[149] E. S. Reddy, N. H. Babu, Y. Shi, D. A. Cardwell, and G. J. Schmitz, "Processing of single domain Y–Ba–Cu–O with pre-defined 3D interconnected porosity for bulk reinforcement," *Supercond. Sci. Technol.*, vol. 16, no. 11, p. L40, 2003.

[150] E. S. Reddy, M. Herweg, and G. J. Schmitz, "Processing of Y2BaCuO5 foams," *Supercond. Sci. Technol.*, vol. 16, no. 5, p. 608, 2003.

[151] J. G. Noudem, E. S. Reddy, and G. J. Schmitz, "Magnetic and transport properties of YBa2Cu3Oy superconductor foams," *Phys. C Supercond.*, vol. 390, no. 4, pp. 286–290, 2003.

[152] J. G. Noudem, S. Meslin, C. Harnois, D. Chateigner, and X. Chaud, "Melt textured YBa2Cu3Oy bulks with artificially patterned holes: a new way of processing c-axis fault current limiter meanders," *Supercond. Sci. Technol.*, vol. 17, no. 7, p. 931, 2004.

[153] X. Chaud *et al.*, "Isothermal growth of large YBaCuO single domains through an artificial array of holes," *J. Cryst. Growth*, vol. 275, no. 1–2, pp. e855–e860, 2005.

[154] D. Kenfaui, P. Sibeud, E. Louradour, X. Chaud, and J. G. Noudem, "An effective approach for the development of reliable YBCO bulk cryomagnets with high trapped field performances," *Adv. Funct. Mater.*, vol. 24, no. 25, pp. 3996–4004, 2014.

[155] T. Hlásek *et al.*, "Enhanced mechanical properties of single-domain YBCO bulk superconductors processed with artificial holes," *IEEE Trans. Appl. Supercond.*, vol. 29, no. 5, pp. 1–4, 2019.

[156] F. Antončík *et al.*, "Radial and axial stiffness of superconducting bearings based on YBCO single-domain bulks processed with artificial holes," *Supercond. Sci. Technol.*, vol. 33, no. 4, p. 45010, 2020.

[157] T. Hlasek *et al.*, "Enhanced mechanical properties of single-domain YBCO bulks via

artificial holes," in *ASC Poster 2MPo2D-02*, 2018.

[158] M. Tsuchimoto and H. Takashima, "Two-dimensional stress distributions in disk and ring high-Tc superconductors," *Jpn. J. Appl. Phys.*, vol. 39, no. 10R, p. 5816, 2000.

[159] K.-H. Müller *et al.*, "New permanent magnets," *J. Magn. Magn. Mater.*, vol. 226, pp. 1370–1376, 2001.

[160] T. Nakamura, Y. Itoh, M. Yoshikawa, T. Oka, and J. Uzawa, "Development of a superconducting magnet for nuclear magnetic resonance using bulk high-temperature superconducting materials," *Concepts Magn. Reson. Part B Magn. Reson. Eng. An Educ. J.*, vol. 31, no. 2, pp. 65–70, 2007.

[161] T. Yanamoto, M. Izumi, K. Umemoto, T. Oryu, Y. Murase, and M. Kawamura, "Load test of 3-MW HTS motor for ship propulsion," *IEEE Trans. Appl. Supercond.*, vol. 27, no. 8, pp. 1–5, 2017.

[162] U. Floegel-Delor *et al.*, "Mobile HTS bulk devices as enabling ton-force technology for maglev trains," *IEEE Trans. Appl. Supercond.*, vol. 29, no. 5, pp. 1–5, 2019.

[163] D. F. Lee, C. S. Partsinevelos, R. G. Presswood Jr, and K. Salama, "Melt texturing of preferentially aligned YBa2Cu3Ox superconductor by a seeded directional solidification method," *J. Appl. Phys.*, vol. 76, no. 1, pp. 603–605, 1994.

[164] P. Schätzle, G. Krabbes, G. Stöver, G. Fuchs, and D. Schläfer, "Multi-seeded melt crystallization of YBCO bulk material for cryogenic applications," *Supercond. Sci. Technol.*, vol. 12, no. 2, p. 69, 1999.

[165] S. Nariki, S. J. Seo, N. Sakai, and M. Murakami, "Influence of the size of Gd211 starting powder on the critical current density of Gd-Ba-Cu-O bulk superconductor," *Supercond. Sci. Technol.*, vol. 13, no. 6, p. 778, 2000.

[166] N. Okajima, Y. Oura, H. Ohsaki, H. Teshima, and M. Morita, "Trapped Flux and Current Density Distributions of a 140 mm Diameter Large Single-grain Gd-Ba-Cu-O Bulk Superconductor Fabricated with RE Compositional Gradient Method," *Phys. Procedia*, vol. 45, pp. 269–272, 2013.

[167] S. Nariki, N. Sakai, and M. Murakami, "Melt-processed Gd–Ba–Cu–O superconductor

with trapped field of 3 T at 77 K," *Supercond. Sci. Technol.*, vol. 18, no. 2, p. S126, 2004.

[168] S. Nariki, H. Teshima, and M. Morita, "Development of high-performance QMG bulk magnets for high magnetic field engineering applications," *IEEE Trans. Appl. Supercond.*, vol. 26, no. 3, pp. 1–4, 2016.

[169] R. L. Fleischer, H. R. Hart Jr, K. W. Lay, and F. E. Luborsky, "Increased flux pinning upon thermal-neutron irradiation of uranium-doped YBa2Cu3O7," *Phys. Rev. B*, vol. 40, no. 4, p. 2163, 1989.

[170] M. C. Frischherz, M. A. Kirk, J. Farmer, L. R. Greenwood, and H. W. Weber, "Defect cascades produced by neutron irradiation in YBa2Cu3O7−δ," *Phys. C Supercond.*, vol. 232, no. 3–4, pp. 309–327, 1994.

[171] M. Eisterer, S. Tönies, W. Novak, H. W. Weber, R. Weinstein, and R. Sawh, "Improvement of critical current densities by fission tracks in U-doped high temperature superconductors," *Supercond. Sci. Technol.*, vol. 11, no. 10, p. 1001, 1998.

[172] G. Krabbes *et al.*, "Zn doping of YBa2Cu3O7 in melt textured materials: peak effect and high trapped fields," *Phys. C Supercond.*, vol. 330, no. 3–4, pp. 181–190, 2000.

[173] S. Gruss *et al.*, "Superconducting bulk magnets: Very high trapped fields and cracking," *Appl. Phys. Lett.*, vol. 79, no. 19, pp. 3131–3133, 2001.

[174] G. Fuchs *et al.*, "Trapped magnetic fields larger than 14 T in bulk YBa2Cu3O7−x," *Appl. Phys. Lett.*, vol. 76, no. 15, pp. 2107–2109, 2000.

[175] O. Vakaliuk, F. Werfel, J. Jaroszynski, and B. Halbedel, "Trapped field potential of commercial Y-Ba-Cu-O bulk superconductors designed for applications," *Supercond. Sci. Technol.*, vol. 33, no. 9, p. 95005, 2020.

[176] A. Patel *et al.*, "A trapped field of 17.7 T in a stack of high temperature superconducting tape," *Supercond. Sci. Technol.*, vol. 31, no. 9, p. 09LT01, 2018.

[177] H. Fujishiro, T. Naito, and S. Awaji, "Proposal of effective mechanical reinforcement structure for REBaCuO disk bulk pair by full metal encapsulation to achieve higher trapped field over 20 T," *Supercond. Sci. Technol.*, 2019.

[178] H. Fujishiro, S. Nariki, and M. Murakami, "Thermal conductivity and thermoelectric power of DyBaCuO bulk superconductors," *Supercond. Sci. Technol.*, vol. 19, no. 7, p. S447, 2006.

[179] K. Y. Huang *et al.*, "Composite stacks for reliable 17 T trapped fields in bulk superconductor magnets," *Supercond. Sci. Technol.*, vol. 33, no. 2, p. 02LT01, 2019.

[180] K. Morita, H. Teshima, and S. Nariki, "Development of New Reinforcement Method and 10T Magnetization of QMG Magnet," *Nippon Steel Sumitomo Met. Tech. Rep.*, vol. No. 117, 2017.

[181] M. Morita, "History and recent progress of QMG^{TM} and QMG bulk magnets," in *Journal of Physics: Conference Series*, 2018, vol. 1054, no. 1, p. 12046.

[182] K. Takahashi, H. Fujishiro, T. Naito, Y. Yanagi, Y. Itoh, and T. Nakamura, "Fracture behavior analysis of EuBaCuO superconducting ring bulk reinforced by a stainless steel ring during field-cooled magnetization," *Supercond. Sci. Technol.*, vol. 30, no. 11, p. 115006, 2017.

[183] Henkel, "LOCTITE STYCAST 2850FT." Technical Data Sheet, 2016.

[184] Epoxy Technology Inc, "Understanding Mechanical Properties of Epoxies For Modeling, Finite Element Analysis (FEA)," 2012. [Online]. Available: http://www.epotek.com/site/files/Techtips/pdfs/tip19.pdf.

[185] University of Cambridge, "Mechanics of Fibre-Reinforced Composites: Stiffness of long fibre composites," 2008. [Online]. Available: https://www.doitpoms.ac.uk/tlplib/fibre_composites/stiffness.php. [Accessed: 08-Mar-2021].

[186] M. Tomita and M. Murakami, "Improvement of the mechanical properties of bulk superconductors with resin impregnation," *Supercond. Sci. Technol.*, vol. 13, no. 6, p. 722, 2000.

[187] M. Tomita and M. Murakami, "Mechanical properties of bulk superconductors with resin impregnation," *Supercond. Sci. Technol.*, vol. 15, no. 5, p. 808, 2002.

[188] Y. Shi *et al.*, "Batch-processed GdBCO–Ag bulk superconductors fabricated using

generic seeds with high trapped fields," *Phys. C Supercond. its Appl.*, vol. 470, no. 17–18, pp. 685–688, 2010.